Doctoral Dissertation

# Theoretical Study on The Role of Oxygen Vacancy in The Improvement of Metal Oxides' Reactivity for Green Technology Applications

# グリーンテクノロジーに向けた金属酸化物の反応性向上における酸素欠陥の役割に関する理論的研究

*NGUYEN HOANG LINH*

July 2015

Department of Applied Physics
Graduate School of Engineering
Osaka University

# Abstract

Metal oxides have attracted a lot of attention because of their various promising industrial applications, especially considering how these materials are chosen for their unique chemical, electrical and optical properties. These properties are often related to the presence of defects in the structure, in particular, oxygen defects (O-vacancies) where studies on their effects are gaining interest in material science. A new approach in materials design called "defect engineering" has been introduced with the purpose of manipulating the nature and concentration of defects in solids in a desired manner for specific and targeted functions. This study reports O-vacancies as effective defects that would enable us to change the characteristics of metal oxides, e.g., geometric and electronic structures, the corresponding chemical and physical reactivity, for promoting a desired reactivity. By density functional theory (DFT) calculations, a detailed understanding of the effects of O-vacancies in two metal oxides case studies of well-known catalysts for a lot of green-technology applications is provided: anatase $TiO_2(001)$ and lanthanum gallate ($LaGaO_3$)-based materials.

*Anatase $TiO_2(001)$.* Anatase $TiO_2$ is popular as a photocatalyst and non-platinum-based catalyst for fuel cells, with $O_2$ adsorption as an important step for a lot of catalytic reactivities. Our results show that $O_2$ molecule is difficult to adsorb on the stoichiometric anatase $TiO_2(001)$, which is attributed to a strong repulsion from the O ions of the surface. This is in agreement with the experimental observations on anatase $TiO_2(001)$ for $O_2$ adsorption. Creation of O-vacancy is favourable on the 2-fold coordinated O ion on the surface, resulting in excess electrons. These excess electrons redistribute locally around the two neighboring 4-fold coordinated Ti ions, and an associated localized defect state appears in the corresponding electronic structure. Calculations with on-site Coulomb interaction parameters, $U$, show that the localized defect state can be described well with GGA+$U$; however, there is no significant qualitative change on the adsorption of $O_2$ on this surface regardless of the $U$ value considered. The presence of O-vacancy promotes $O_2$ adsorption on an initially inert stoichiometric $TiO_2(001)$ through creation of active site on the surface. The adsorbed $O_2$ can be found either in superoxide state ($O_2^-$) and peroxide state ($O_2^{2-}$), depending on the adsorption configuration. An $O_2^-$ anion was formed when the O-O bond is oriented parallel to the surface, along [010]. And an $O_2^{2-}$ anion forms when

$O_2$ adsorbs perpendicularly to the surface, along [001]. $O_2^-$ state of adsorbed $O_2$ is more stable than $O_2^{2-}$ state. Healing/migration of the surface occurs when one of the O atoms of the perpendicularly adsorbed $O_2$ fills the vacant site recovering the stoichiometric surface and the other atom diffuses. By filling the O-vacancy which is the active site for $O_2$ adsorption, healing/migration effect could reduce the efficiency of the surface chemical reactions and slow down the catalytic reaction rate. However, this effect has less probability to occur than the $O_2$ adsorption configuration with $O_2^-$ state. Anatase $TiO_2(001)$ with O-vacancies, in general, still promotes $O_2$ molecule interaction with the surface.

*Pristine $LaGaO_3$ (LG) based materials.* $LaGaO_3$-based materials are known as promising ionic conductors for electrolyte of SOFC applications. The geometric and electronic structure of pristine/stoichiometric LG is based on the tilting of $[GaO_6]$ octahedrons from the ideal cubic perovskite structure, which cause the difference in the nature of the bonds of O ions and the surrounding cation ions, especially the bonds with La ions. Equatorial O ions have weaker bonds with La ions than apical O ions. O-vacancy is difficult to form in pristine LG as indicated by the calculated large O-vacancy formation energy. The equatorial O-positions of $[GaO_6]$ octahedron are found to be more favorable than the apical O-positions for introducing O-vacancy. The effect of O-vacancy on the structural characteristics is primarily observed around the vicinity of the vacancy site. The introduction of O-vacancy leads to excess electrons in the O-deficient LG ($LG_{-\delta}$), which induces accumulation of charge between two 5-fold coordinated Ga ions, and an associated localized defect state appears in the corresponding electronic structure. The appearance of O-vacancy allows the O ion to migrate in $LG_{-\delta}$ through O hopping to the O-vacancy site. Calculated potential curves for O-migration shows that the preferable migration paths are along the equatorial edges of the $[GaO_6]$ octahedron with high activation energy. The mechanism of O-migration reveals that excess electrons enhance not only the repulsive Coulomb interaction between the mobile O and the surrounding Ga ions, but also the attractive Coulomb interaction between the mobile O and the surrounding La ions. Although the presence of O-vacancy induces O-migration through the initially inert LG-based materials, it also produces excess electrons, which is the reason for the high activation energy for O (O-vacancy) migration in pristine LG based materials.

*Sr and Mg co-doped $(LaSr)(GaMg)O_3$ (LSGM) based materials.* Doping divalent elements into trivalent cation sites is one way to reduce excess electrons from the creation of O-vacancy, and, consequently, decrease the O-vacancy formation

energy and enhance the O-migration. Due to the similarities in ionic radii with the host (La/Ga) ions, Sr and Mg dopants at La and Ga sites, respectively, were chosen. Doping with divalent cations resulted in charge compensation, which reduces the O-vacancy formation energy. It is easier for O-vacancies to be created in co-doped LSGM-based materials than in LG-based materials. Due to the nature of the bond between O ions and the surrounding cation ions, especially Sr and Mg, O-vacancy is easier to form nearest to Sr than nearest to Mg. This explains the experimental observation on the significant role of Sr in increasing O-vacancy concentration. Together with reducing the O-vacancy formation energy, the co-doped LSGM shows the significant decrease in the activation energy of O (O-vacancy) migration. Most of the preferable path for O migration in the co-doped LSGM is still the same as that of the pristine LG-based material, i.e., between two equatorial O positions. The presence of dopants, especially Sr at La sites, introduces other preferable paths, which are from the O positions outside the vicinity of Sr to the O positions nearest to Sr, either on the apical edge or equatorial edge of [$GaO_6$] octahedra.

From these studies, we have shown that the presence of O-vacancies has significant effects on the promotion of desired reactivities in initially inert materials. Understanding about the nature of O vacancies in oxide materials allows us to propose ways on improving it's efficiency for a desired reaction, e.g., through doping, etc. It raises the interest to further research of O-vacancies in metal oxides.

# Contents

**Abstract** iii

**Abbreviation** vii

**List of Figures** xiv

**List of Tables** xvi

**1 Introduction** 1

**2 O-vacancies in Anatase $TiO_2$(001)** 5

2.1 Titanium Dioxide and Catalytic Reactivities . . . . . 5

2.2 The Stoichiometric Anatase $TiO_2$(001) . . . . . 7

2.2.1 Geometric Structure . . . . . 7

2.2.2 Electronic Properties . . . . . 8

2.3 O-deficient/Reduced Anatase $TiO_{2-\delta}$(001) . . . . . 9

2.3.1 O-vacancy Formation . . . . . 9

2.3.2 Geometric Structure . . . . . 10

2.3.3 Electronic Properties . . . . . 10

2.4 The $O_2$ Adsorption . . . . . 13

2.4.1 On the stoichiometric anatase $TiO_2$(001) . . . . . 13

2.4.2 On the O-deficient/Reduced Anatase $TiO_{2-\delta}$(001) . . . . . 15

2.4.3 Healing/ Migration effect . . . . . 18

2.5 Summary . . . . . 19

**3 O-vacancies in Pristine Lanthanum Gallate Based Materials** 21

3.1 LG-based materials . . . . . 21

3.2 The Pristine/ Stoichiometric LG . . . . . 22

3.2.1 Geometric Structure . . . . . 22

3.2.2 Electronic Properties . . . . . 23

3.3 O-deficient/Reduced $LaGaO_{3-\delta}$ ($LG_{-\delta}$) . . . . . 24

3.3.1 O-vacancy Formation . . . . . 24

3.3.2 Geometric Structure . . . . . 25

3.3.3 Electronic Properties . . . . . 26

3.4 Oxygen Migration (O-vacancy migration) . . . . . 26
3.5 Summary . . . . . 30

**4 O-vacancies in Doped $LaGaO_3$ Based Materials 31**
4.1 Doped $LaGaO_3$-Based Materials . . . . . 31
4.2 Sr- and Mg-Doped $LaGaO_3$: (LSGM) . . . . . 32
4.2.1 Geometric Structure . . . . . 32
4.2.2 Electronic Properties . . . . . 33
4.3 O-deficient/reduced $(LaSr)(GaMg)O_{3-\delta}$ . . . . . 35
4.3.1 Geometric Structure . . . . . 36
4.3.2 Electronic Properties . . . . . 37
4.3.3 Oxygen Migration (O-vacancy Migration) . . . . . 38
4.3.3.1 Effect of Sr Ions . . . . . 38
4.3.3.2 Effect of Mg Ions . . . . . 39
4.3.3.3 Outside the Vicinity of Dopants . . . . . 41
4.4 Summary . . . . . 42

**5 Summary, Conclusion and Outlook 43**

**A Density Functional Theory Formalism 47**
A.1 The Schrödinger Equation . . . . . 47
A.2 Hohenberg-Kohn Theorems . . . . . 48
A.3 Kohn-Sham Equation . . . . . 48
A.4 Approximations for Exchange-Correlation Functional . . . . . 50
A.5 Implementation of DFT . . . . . 51

**Bibliography 53**

**Acknowledgement 65**

**List of Publications 66**

**List of Scientific Meeting 67**

# Abbreviation

| | |
|---|---|
| CB | Conduction Band |
| CBM | Conduction Band Minimum |
| DFT | Density Functional Theory |
| DOS | Density of States |
| EPR | Electron Paramagnetic Resonance |
| ESR | Electron Spin Resonance |
| FIM | Field Ion Microscopy |
| GGA | Generalized Gradient Approximation |
| LDA | Local Density Approximation |
| LDOS | Local Density of States |
| LG | $LaGaO_3$ |
| $LG_{-\delta}$ | $LaGaO_3$ ($\delta = 0.0626$) |
| LSGM | $(La_{1-x}Sr_x)(Ga_{1-x}Mg_x)O_3$ (x=0.0625) |
| $LSGM_{-\delta}$ | $(La_{1-x}Sr_x)(Ga_{1-x}Mg_x)O_{3-\delta}$ (x=0.0625 and $\delta = 0.0625$) |
| ORR | Oxygen Reduction Reaction |
| PEMFC | Proton Exchange Membrane Fuel Cell |
| PES | Potential Energy Surface |
| SOFC | Solid Oxide Fuel Cell |
| STM | Scanning Tunneling Microscopy |
| SE-IRAS | Surface-Enhanced Infrared Reflection Adsorption Spectroscopy |
| STS | Scanning Tunneling Spectroscopy |
| VB | Valence Band |
| VBM | Valence Band Maximum |

# List of Figures


1.1 "Defect Engineering" approach to improve the desired reactivity in metal oxides. . . . . 2

2.1 The different polymorphs of titanium dioxide ($TiO_2$): (a) rutile, (b) anatase and (c) brookite. Ti : large/blue spheres. O: small/red spheres. . . . . 5

2.2 Side view (along $[\bar{1}00]$) of the slab model for anatase $TiO_2(001)$-$(2 \times 2)$. . . . . 7

2.3 Calculated local density of states (LDOS) of the stoichiometric $TiO_2(001)$ The DOS contribution of the top surface layer was shown, and so the corresponding $p$ orbitals of the $O_{2c}$, $p$ orbitals of the $O_{3c}$ and $d$ orbitals of the $Ti_{5c}$. The arrows indicate the corresponding valence band maximum (VBM) and conduction band minimum (CBM). Energies given in [eV] with respect to the Fermi level ($E_F$). . . . . 8

2.4 Four O-vacancy positions on anatase $TiO_2(001) - (2 \times 2)$, viz., in the $O_{2c}$ and $O_{3c}$ planes of the topmost layer and the O planes of the next layer (of $TiO_2$ units) (cf., Fig. 2.2). These are also alternatively labeled as $1^{st}$-, $2^{nd}$-, $3^{rd}$-, $4^{th}$-layers. . . . . 9

2.5 The O-deficient/reduced anatase $TiO_2(001)$ after relaxation. On the surface, there are two $Ti_{4c}$ near the $O_{2c}^{\text{vacant}}$ site. $O_{2c}^{\text{1st}}$, $O_{2c}^{\text{2nd}}$, and $O_{2c}^{\text{3rd}}$ represent the $1^{st}$, $2^{nd}$, and $3^{rd}$ nearest $O_{2c}$ from the $O_{2c}^{\text{vacant}}$ site. 10

2.6 Calculated LDOS of the O-deficient/reduced $TiO_2(001)$ for several on-site Coulomb interaction values $U$: (a) 0.0 eV, (b) 2.4 eV, (c) 3.0 eV, (d) 4.0 eV, and (e) 5.0 eV. The DOS contribution from $d$-orbitals of the $Ti_{4c}$, $p$-orbitals of the nearest $O_{2c}$ ( i.e., $O_{2c}^{\text{1st}}$) and $p$-orbitals of the $2^{nd}$ and $3^{rd}$ nearest $O_{2c}$ ( i.e., $O_{2c}^{\text{2nd}}$ and $O_{2c}^{\text{3rd}}$) from the $O_{2c}^{\text{vacant}}$ site. The arrows indicate the corresponding VBM and CBM. Energies given in [eV] with respect to the Fermi level ($E_F$). 12

2.7 (a) Top view of a stoichiometric anatase $Ti0_2(001)$, with the corresponding symmetric sites, viz., atop $Ti_{5c}$; $O_{2c}$; $O_{3c}$; and Ho: the hollow site. Also shown are the stable configurations for an incoming $O_2$: (b) atop $Ti_{5c}$, with the O-O bond along [001]; (c) atop $O_{2c}$, with the O-O bond along [010]; (d) atop $O_{2c}$, with the O-O bond along [001]; (e) atop $O_{3c}$, with the O-O bond along [100]; and (f) atop Ho, with the O-O bond along [010]. . . . . 13

2.8 (a): Optimized structure of the A1 adsorption configuration at the O-vacancy site: $O_2$ adsorbs with the O-O bond parallel to the surface along the [010] direction. (b): Calculated DOS of the top layer of the O-deficient/reduced anatase $TiO_2(001)$ after oxygen adsorption in A1 configuration with standard GGA ($U = 0$ eV) calculations and GGA+$U$ ($U = 4$ eV) calculations. Energies given in [eV] with respect to the Fermi level ($E_F$). . . . . 15

2.9 (a): Optimized structure of the A2 adsorption configurations at the O-vacancy site: $O_2$ adsorbs with the O-O bond perpendicular to the surface along the [001] direction. In the A2 configuration, the bottom O ($O_{ad1}$) of $O_2$ protrudes from the surface, and the top O ($O_{ad2}$) is near the $Ti_{4c}$-plane. (b): Calculated DOS of the top layer of the O-deficient/reduced anatase $TiO_2(001)$ after oxygen adsorption in A2 configuration with standard GGA ($U = 0$ eV) calculations and GGA+$U$ ($U = 4$ eV) calculations. Energies given in [eV] with respect to the Fermi level ($E_F$). . . . . 17

2.10 Potential energy surface for O adatom diffusion on the stoichiometric $TiO_2(001)$. The coordinates $(x, y)$ of the O adatom are given as fractional units of the $(2 \times 2)$ surface. The top-view and the symmetric sites correspond to Figure 2.7. (Inset) The configuration corresponding to the case when the O adatom is at a minima above $(x, y) = (0, 0.125)$. O adatom: smaller/yellow sphere. Contour spacing: 0.15 eV. Surface lattice parameter $a = 3.79(4)$ Å. . 19

3.1 The optimized structure of the stoichiometric LG as viewed from (a) the $c$-axis and (b) the $b$-axis, and (c) a magnified view of the [$GaO_6$] octahedron of the supercell. The $(2 \times 1 \times 2)$ supercell contains 80 atoms: 16 La, 16 Ga, and 48 O. The corresponding coordinate axes ($a, b, c$ and $a', c'$) are also shown. . . . . 22

3.2 Calculated LDOS of the stoichiometric $LaGaO_3$ (LG). (a) DOS for whole $(2 \times 1 \times 2)$ super-cell with the DOS contributions from lanthanum (La), gallium (Ga), apical oxygen ($O_{ap}$), and equatorial oxygen ($O_{eq}$), respectively. (b)-(e) DOS contributions from the $s$, $p$, $d$, and $f$-orbitals of La, Ga, $O_{ap}$, and $O_{eq}$, respectively. Energies are given in [eV] with respect to the Fermi level ($E_F$). The corresponding VBM and CBM are also indicated. . . . . 23

3.3 A magnified view of the most stable pyramidal structure [$GaO_5$] of the reduced $LaGaO_3$ ($LG_{-\delta}$). O vacancy ($O^{vac}$: white, dashed-outlined sphere. (Inset) The most stable position for $O^{vac}$ in the $(2\times1\times2)$ supercell, containing 79 atoms: 16 La (largest/light purple spheres), 16 Ga ($2^{nd}$ largest/green spheres), 47 O (smallest/red spheres). The corresponding coordinate axes ($a, b, c$ and $a', c'$) are also shown. . . . . 25

3.4 Calculated density of states (DOS) of O-deficient/reduced $LaGaO_3$ ($LG_{-\delta}$). (a) [$GaO_5$] pyramids, which consist the surrounding $La^{vc}$ ions (red/dash), the $Ga_{5c}$ ions (blue/solid), the surrounding $O^{vc}$ ions ($O_{sur}$), including $O_{eq}^{\pm a'}$ and $O_{ap}^{\pm b}$, and the $O_{vc}$-opposite O ions ($O_{eq}^{-c'}$) metioned in Fig. 3.3. (b) Other [$GaO_6$] octahedra, which include La, Ga and O ions. Energies given in [eV] with respect to the Fermi level ($E_F$). Figure 4(c) shows partial charge distribution of the defect state near the Fermi level of $LG_{-\delta}$, where the isosurface value is 0.003 $e/\text{Å}^3$. The corresponding VBM and CBM are also indicated. . . . . 26

3.5 (a) O-migration paths from the most stable $O^{vac}$ configuration in an O-deficient/reduced $LaGaO_3$ ($LG_{-\delta}$). Path I corresponds to the shortest path between two non-vertex sharing [$GaO_6$] octahedra. Path II corresponds to the path between $O_{eq}$ sites in a a vertex-sharing [$GaO_6$] octahedra. There are two paths between the $O_{eq}$ sites, viz., paths III and IV, as shown. (b) Calculated energies corresponding to certain points along the paths indicated. Energies given in [eV] with respect to the initial position configuration. . . 27

3.6 The most favourable O-vacancy ($O^{vac}$) migration path (path III in Fig. 3.5). The labels "Initial", "1", "2", "3", "Final" indicate the initial, location, intermediate locations, and final locations of ($O^{vac}$). $O_m$ traces the same path in the opposite direction. . . . . 28

3.7 Calculated energies and partial charge distributions of the defect states correspond to each states along the O-vacancy ($O^{vac}$) migration path (path III in Fig. 3.5and also cf., Fig. 3.6). Isosurfaces are given in intervals of 0.003 $e/Å^3$. . . . . 29

4.1 The optimized structure of the non-defect LSGM. (a) In the (2×1× 2) supercell, a Sr ion and a Mg ion were substituted for the La ion and Ga ion, respectively. The supercell contains 80 atoms: 15 La (light purple spheres), 1 Sr (blue spheres), 15 Ga (green spheres), 1 Mg (orange spheres), 48 O (red spheres). (b) A magnified view of the vicinity of Sr ion with the three nearest O ions (viz. $O_1^{Sr}$, $O_2^{Sr}$ and $O_3^{Sr}$). (c) A magnified view of the vicinity of Mg ion. $O^{Mg}$ and $Ga^{Mg}$ refer to the O ion of [$MgO_6$] octahedron and the first nearest Ga ions. . . . . 32

4.2 Calculated local density of states (LDOS) of the doped LSGM. (a) DOS for whole $(2 \times 1 \times 2)$ super-cell with DOS contributions from lanthanum (La), gallium (Ga), apical oxygen ($O_{ap}$), and equatorial oxygen ($O_{eq}$), respectively. (b) LDOS for the vicinity of Sr ion, which consist the surrounding $La^{Mg}$ ions, Sr ion and the $O^{Sr}$ ions (i.e. $O_1^{Sr}$, $O_2^{Sr}$ and $O_3^{Sr}$). (Inset: The magnified view of LDOS in the energy range [-4.5 eV, 0.5 eV].) (c) DOS for the vicinity of Mg ion, which consist Mg ion, the O ions of [$MgO_6$] ($O^{Mg}$) and the nearest Ga ions ($Ga^{Mg}$). (cf., Fig. 4.1) (Inset: The magnified view of LDOS in the energy range [-4.5 eV, 0.5 eV].) Energies are given in [eV] with respect to the Fermi level ($E_F$). The corresponding valence band maximum (VBM) and conduction band maximum (CBM) are also indicated. . . . . 34

4.3 A magnified view of the most stable pyramidal structure [$GaO_5$] of the O-deficient/reduced $LSGM_{-\delta}$. One of the O ions along $b$-axis is replaced by an O vacancy ($O^{vac}$, white, dashed-outlined sphere), resulting in two 5-fold coordinated Ga ions ($Ga_{5c}$, viz., $Ga_{5c}^{\pm b}$). The $(2 \times 1 \times 2)$ supercell contains 79 atoms: 15 La ($2^{nd}$ largest/light purple spheres), 1 Sr (largest/blue sphere), 15 Ga ($4^{th}$ largest/green spheres), 1 Mg ($3^{rd}$ largest/orange sphere), 47 O (smallest/red spheres). (Inset) The most stable position for $O^{vac}$ in the $(2 \times 1 \times 2)$ supercell. The corresponding coordinate axes ($a, b, c$ and $a', c'$) are also shown. . . . . 36

4.4 Calculated LDOS of LSGM and O-deficient/reduced LSGM$_{-\delta}$. (a) DOS for whole ($2 \times 1 \times 2$) super-cell: (b) LDOS for the vicinity of Sr ion, which consist the surrounding La$^{\mathrm{Mg}}$ ions, Sr ion and the O$^{\mathrm{Sr}}$ ions (incl. O$_1^{\mathrm{Sr}}$, O$_2^{\mathrm{Sr}}$ and O$_3^{\mathrm{Sr}}$). (c) LDOS for the vicinity of Mg ion, which consist the O ions of [MgO$_6$] (O$^{\mathrm{Mg}}$), the nearest Ga ions (Ga$^{\mathrm{Mg}}$) and Mg ions. Energies are given in [eV] with respect to the Fermi level ($E_{\mathrm{F}}$). The corresponding VBM and CBM are also indicated. . . . . 37

4.5 **(a)** O-migration paths from the most stable O$^{\mathrm{vac}}$ configuration near Sr ion (i.e., O$_{1st}^{\mathrm{Sr}}$) in the O-deficient/reduced LSGM$_{-\delta}$. path Sr-I corresponds to the path near Sr ion, which has the transition state of mobile O passing through the triangle △Sr-Ga-La. path Sr-II corresponds to the path from the outside O site to the site nearest Sr ion (Mobile O passes the triangle △La-Ga-La in the transition state). **(b)** Calculated energies corresponding to certain points along the paths indicated in Fig. (a). The migration activation energy ($E_{\mathrm{a}}$) corresponds to the energy of the transition state. Energies were given in [eV] with respect to the initial position configuration. . . . . 38

4.6 (a): O-migration paths from the most stable O$^{\mathrm{vac}}$ configuration near Mg ion in the O-deficient/reduced LSGM$_{-\delta}$. path II-g and path II-m correspond to the path between the apical O site and equatorial O sites within the nearest [GaO$_6$] and [MgO$_6$] octahedra, respectively. path III-g and III-m correspond to the path between two equatorial O sites within the nearest [GaO$_6$] and [MgO$_6$] octahedra, respectively. (b): Calculated energies corresponding to certain points along the paths indicated in Fig.(a). The migration activation energy ($E_{\mathrm{a}}$) corresponds to the energy of the transition state. Energies were given in [eV] with respect to the initial position configuration. . . . . 40

4.7 (a): O-migration paths from the most stable $O^{vac}$ configuration outside the vicinity of dopants in the O-deficient/reduced $LSGM_{-\delta}$. Path II-o corresponds to the path between the apical O site and equatorial O sites, and path III-o correspond to the path between two equatorial O sites within a $[GaO_6]$ octahedron. (b): Calculated energies corresponding to certain points along the paths indicated in Fig.(a). The migration activation energy ($E_a$) corresponds to the energy of the transition state. Energies were given in [eV] with respect to the initial position configuration. . . . . 41

# List of Tables


2.1 Oxygen vacancy formation energy ($E_{\mathrm{O}}^{\mathrm{vacancy}}$, Eq. 2.1) in anatase $TiO_2(001) - (2 \times 2)$ (cf., Figs. 2.2and 2.4). . . . . 10

2.2 Displacement ($\Delta z$) along [001] from the stoichiometric surface, bond length ($r$), the subtended angle $\measuredangle(\mathrm{Ti}_{4c} - \mathrm{O}_{2c}^{\mathrm{1st}} - \mathrm{Ti}_{4c})$ and the charge gain/loss ($\pm\Delta Q$) due to the formation of $\mathrm{O}_{2c}^{\mathrm{vacant}}$ for the surface Ti (i.e., $\mathrm{Ti}_{4c}$ and $\mathrm{Ti}_{5c}$) and the surface O (i.e., $\mathrm{O}_{2c}^{\mathrm{1st}}$, $\mathrm{O}_{2c}^{\mathrm{2nd}}$, $\mathrm{O}_{2c}^{\mathrm{3rd}}$ and $\mathrm{O}_{3c}$), with various on-site Coulomb parameters $U$ (cf., Fig. 2.5). Negative values of $\Delta z$ correspond to displacement of the surface ions toward the bulk. . . . . 11

2.3 Computed adsorption energy ($E_{\mathrm{ads}}$, Eq. 2.2) of $O_2$ on the stoichiometric $TiO_2(001)$, bond length of the adsorbed $O_2$ ($r_{\mathrm{O-O}}$), and amount of charge transfer ($\Delta Q$) from anatase $TiO_2(001)$ to the $O_2$ adsorbed at each of the five stable adsorption configurations/sites, viz., $\mathrm{Ti}_{5c}$, $\mathrm{O}_{2c}[010]$, $\mathrm{O}_{2c}[001]$, $\mathrm{O}_{3c}$, and Ho (cf., Fig. 2.7.). A positive value of $E_{\mathrm{ads}}$ correspond to the endothermic adsorption of $O_2$. . . 14

2.4 Computed adsorption energy ($E_{\mathrm{ads}}$, Eq. 2.2) of $O_2$ on the O-deficient/reduced $TiO_2(001)$, bond length of the adsorbed $O_2$ ($r_{\mathrm{O-O}}$), the stretching frequency ($\nu_{\mathrm{O-O}}$), and charge gain/loss ($\pm\Delta Q$) by the neighboring Ti and O atoms on O-reduced surface due to the adsorption of $O_2$, for various on-site Coulomb parameters $U$ (cf., Fig. 2.8and Fig. 2.9). . . . . 16

3.1 Calculated O-vacancy formation energy ($E_{\mathrm{O}}^{vacancy}$, Eq. 3.1) in $LaGaO_3$ (LG) for the apical $\mathrm{O}_{\mathrm{ap}}^{\pm b}$ ions along the $b$-axis and the equatorial $\mathrm{O}_{eq}^{\pm c'}$ and $\mathrm{O}_{eq}^{\pm a'}$ ions along the $c$- and $a$-axes, respectively (cf., Fig. 3.1). . . . . 24

3.2 Bader charge analysis for each images along the O-migration path. Positions of $\mathrm{Ga}_{5c}$, $\mathrm{Ga}_{56}$, $\mathrm{Ga}_{65}$, $\mathrm{La}_1^{\mathrm{m}}$ and $\mathrm{La}_2^{\mathrm{m}}$ were shown in Fig. 3.6. $\mathrm{O}_{\mathrm{m}}$ represents for the mobile O ions, which is in the inverse direction with the $O^{vac}$. $\mathrm{O}_{\mathrm{sur}}$ ions are the other O ions surrounding the shared $[GaO_5]$ pyramid. Positive (negative) values refers to electron loss (gain) through bonding with other ions. . . . . 28

4.1 Bader charge analysis of the non-defected LSGM. Effective charge of each atoms is the deduction of the corresponding Bader charge from the original valence electrons of the atoms (10 for La, 13 for Ga, 10 for Sr, 8 for Mg and 6 for O). Positive/negative values refers to loss/gain electrons. $O^{Sr}$ and $O^{Mg}$ refers for O ions in the vicinity of the Sr and Mg, respectively. "Other O" refers to the other O ions outside of the vicinity of Sr and Mg ions. (cf., Fig. 4.1) . . . 34

4.2 Calculated O-vacancy formation energy ($E_{\mathrm{O}}^{vacancy}$, Eq. 4.1) in LSGM for the corresponding $1^{\mathrm{st}}$, $2^{nd}$ and $3^{rd}$ nearest to the Mg and Sr dopants (cf., Fig. 4.1). . . . . 35

4.3 Bader charge analysis of the the O-deficient/reduced $\mathrm{LSGM}_{-\delta}$. Effective charge of each atoms is the deduction of the corresponding Bader charge from the original valence electrons of the atoms (10 for La, 13 for Ga, 10 for Sr, 8 for Mg and 6 for O). Positive/negative values refers to loss/gain electrons. $\mathrm{Ga}_{5c}^{\pm b}$ was showed in Fig. 4.3. $\mathrm{Ga}_{6c}$ and $\mathrm{O}_{\mathrm{vac}}^{\mathrm{sur}}$ refer to the 6-fold coordinated Ga ions in supercell and the surrounding O ion of $[\mathrm{GaO}_5]$ pyramid (incl. $\mathrm{O}_{\mathrm{vac}}^{\pm a'/c'}$, respectively. . . . . 37

4.4 Bond lengths of between mobile O and the surrounding atoms: the shared 5-fold coordinated Ga (i.e., $\mathrm{Ga}_{5c}^{\mathrm{s}}$), O ion of $[\mathrm{GaO}_5]$ pyramid nearest to mobile O, $\mathrm{Sr/La}_1^{\mathrm{m}}$ for the corresponding path *Sr-I*/*Sr-II*, respectively, and $\mathrm{La}_2^{\mathrm{m}}$ (cf., Fig. 4.5a). . . . . 39

# Chapter 1

# Introduction

Global warming and the exhaustion of fossil resources are now becoming more and more serious problems."Green technology" is seen to be an obvious answer to these problems. The field of green technology encompasses a continuously evolving group of methods and materials, from techniques for generating energy to non-toxic cleaning products. The present expectation is that this field will bring innovation and practical changes in the industry and our daily life. This rapidly growing field includes large subject areas, i.e., energy, green building materials, environmentally preferred purchasing, green chemistry, green nanotechnology, with the wide-range of applications. It cannot be denied that the development of this field depends on the invention and development of new materials or the improvement of the original materials to increase efficiency of green technology applications and make them more practical and popular, not only in the industrial field, but also in daily life. Among various promising materials, metal oxides are the largest family of materials exhibiting various interesting chemical and physical characteristics, from the optical properties to superconductivity [1]. It is the reason for the appearance of metal oxides in many green technology applications [2–4], e.g., cathode catalysis of proton exchange membrane fuel cell (PEMFC), solid electrolyte for solid oxide fuel cell (SOFC), photocatalysis, etc.

**"Defect engineering"** Material properties, especially that of metal oxides, are often altered by the presence of faults or defects in the structure [5, 6]. For instance, the strength of a metal is largely connected to the presence of dislocations; the color of a gem is related to the amount of transition metal atom impurities; the spectacular advances in the microelectronic industry are determined by doping semiconductors by the insertion of impurity atoms; the superconducting behaviour of some cuprates is closely connected to the level of oxygen vacancies. Alteration of material properties in the presence of defects in metal oxide has attracted an increasing interest in materials science, surface chemistry, and solid state physics. A new approach in material design called *"defect engineering"* has been introduced with the purpose of manipulating the nature and concentration

of defects in solid in a desired manner for specific and targeted functions.

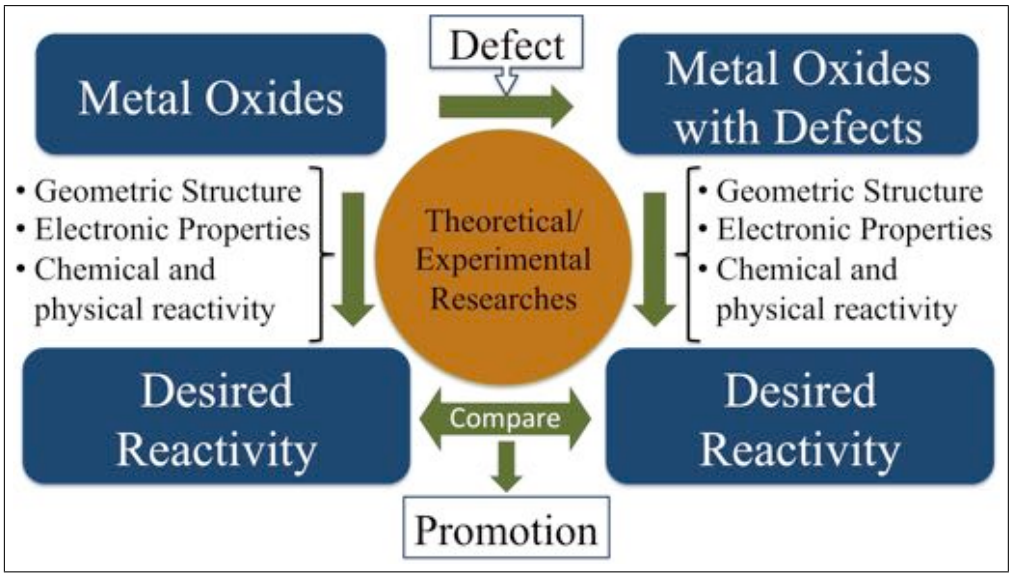


**Figure 1.1:** "Defect Engineering" approach to improve the desired reactivity in metal oxides.

In "defect engineering", the following scheme, as seen in Fig. 1.1, is proposed to achieve the goal of improvement of the desired reactivity of materials

- The characteristics of metal oxides, i.e. geometric structure, electronic properties and the corresponding chemical physical reactivity, will be determined by theoretical/experimental studies to clarify how the desired reactivity works in the considered metal oxides
- According to the understanding of the properties of metal oxide and the reactivity, suitable defects was proposed in the original metal oxides. The presence of defects supposes to enhance the properties of these materials supporting the desired reactivity, or reduce the properties hindering the reactivity.
- The properties of the defected metal oxides will be investigated to determine the effect of defects and the performance of the desired reactivity.
- Improvement of the desired reactivity in the defected metal oxides will be verified by comparing with the corresponding reactivity in the original metal oxides

In my study, oxygen vacancy (O-vacancy) was considered as a special point defect to improve the reactivity of metal oxides. The determination of the existence and properties of O-vacancies and their role in the chemistry of compound

materials have been studied for a long time. However, the limitation in research technology hinder the trace of their reactivity in a direct way. In recent years, the development of technology allows us to track the reactivity of O-vacancies on the metal oxides in direct way, e.g., using of atomically resolved scanning tunneling microscope (STM) images follows a dynamic process of the migration of oxygen vacancies at the surface of a well-ordered $TiO_2$ surface [7]. It was the start of researches related to fully investigate the properties and reactivity of O-vacancies in solid materials, especially in metal oxides. A detailed understanding on the role of O-vacancies would enable us to understand how metal oxides function and, perhaps, even allow us to design oxide materials exhibiting specific, targeted functions. It is good to keep in mind that there is no "almighty" way to perfectly improve any desired reactivity. The advantages and disadvantages of the introduction of O-vacancies defect will be discussed in this dissertation through the density functional theory (DFT)-based calculations, which give us the possibility of molecular-level researches.

In this study, the proposed method applied to two well-known metal oxides: titanium dioxide surface and lanthanum gallate based materials. Titanium dioxide is a well-known catalyst, not only for photocatalytic reactivity, but also as a promising non-platinum based catalyst for oxygen reduction reactions (ORRs). And, lanthanum gallate based materials is famous as promising ionic conductors, which can be applied as electrolyte for SOFCs.

For anatase $TiO_2(001)$ surface, the desired activity of this material is for catalytic reactivity. In this study, we focused on the adsorption of oxygen molecule ($O_2$), which plays an important role in several catalytic activities, e.g., electron scavengers used to suppress electron-hole recombination in photo-oxidation processes, or non-platinum catalysis. Despite the important role of $O_2$, details of the effect of O-vacancy on anatase $TiO_2(001)$ and the $O_2$ adsorption on this surface need to be studied.

For pristine and doped LG-based materials, the focus is on ionic conductivity, which is the basis for applying these materials as electrolyte for SOFC applications. The performance of ionic conductivity in electrolyte materials strongly depends on how oxygen migration (O-migration) work in the materials. However, the mechanism of O-migration in this materials is not well understood. It can be expected that the introduction of O-vacancies induces O-migration through an initially inert LG. An understanding of the role of O-vacancies in the pristine LG-based materials was investigated and discussed in this study. From this, doping at the cation sites was proposed as the solution to control the performance

and reduce the negative effect of O-vacancies in pristine LG-based materials, and improve the O-migration.

# Chapter 2

# O-vacancies in Anatase $TiO_2(001)$

## 2.1 Titanium Dioxide and Catalytic Reactivities

Titanium dioxide ($TiO_2$) has attracted a lot of attention because of its various promising industrial applications, e.g., photocatalytic water splitting and hydrogen production [8, 9], organic dye-sensitized solar cells [10], solar energy conversion [11], to name a few. In almost all these applications, $O_2$ adsorption on $TiO_2$ plays an important role. They act not only as the main oxidizing reagents but also as electron scavengers in photo-oxidation processes [12]. In addition, experiments report that doping nitrogen increases O-vacancy formation and enhances the oxygen reduction reactions (ORRs) on $TiO_2$ surfaces [13–16]. This makes $TiO_2$ even more attractive as an alternative material to replace the expensive platinum used, e.g., as electrocatalysts in fuel cells.

There are three polymorphs of $TiO_2$ used widely in the industry: rutile, anatase and brookite (cf., Fig. *Figure 2.1*).

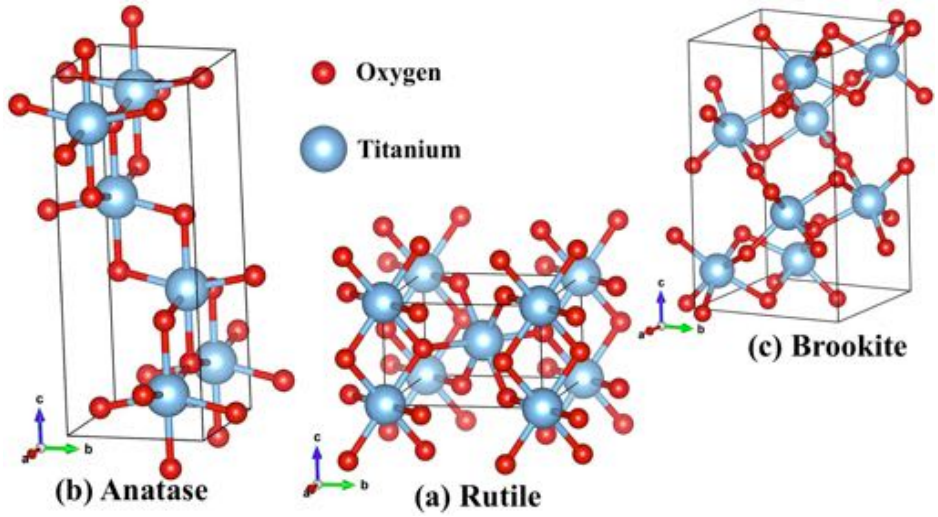


**Figure 2.1:** The different polymorphs of titanium dioxide ($TiO_2$): (a) rutile, (b) anatase and (c) brookite. Ti : large/blue spheres. O: small/red spheres.

Among them, rutile and its facets are the most stable structure, which can be found most in titanium dioxide compounds. This reason makes rutile structure and its surfaces been extensively studied in the last decade, both experimentally (using STM/STS: scanning tunnelling microscopy/spectroscopy and FIM: field ion microscopy, among others) and theoretically [3,17,18]. However, anatase and it surfaces have found to exhibit efficient catalytic reactivity [19,20]. Despite the studies of anatase so far (e.g., in terms of processes such as molecular adsorption, dissociation, and diffusion), full understanding of the potentials of anatase $TiO_2$(001) surface have not been well understood.

Anatase surfaces are mostly exposed (101) facets together with a small amount of (001) facets (less than ca. 6%, according to the Wulff construction [21]). However, the minority (001) surface exhibits high-reactivity [22–24]. In particular, anatase $TiO_2$(001) was found to be active for oxygen adsorption, with a corresponding oxygen adsorption energy lower than anatase $TiO_2$(101) [25]. Both high reactivity to oxygen adsorption and the small oxygen adsorption energy play important roles in catalytic activity in fuel cells. Depending on the experimental conditions [3,26–35], anatase $TiO_2$(001) exposes in both of the unreconstructed [29–31] and $(1 \times 4)$ reconstructed [32–34] surfaces. Studies have shown that the unreconstructed (001)-$(1 \times 1)$ is rather unstable [3,27,35]. There is a large tensile stress present on the unreconstructed (001)-$(1 \times 1)$, which can be attributed to the symmetry breaking, resulting in the inequivalent Ti-O bond lengths on the surface. $(1 \times 4)$ reconstruction of anatase $TiO_2$(001), realized by replacing the rows of surface bridging oxygens with rows of $TiO_3$ species, relieves this large surface tensile stress [3,27,35]. However, $(1 \times 4)$ reconstructed surface is less active than the unreconstructed one [21,36].

Experimental studies [37–39], using Auger electron spectroscopy, low-energy-electron-diffraction, electron-energy-loss spectroscopy, confirmed the presence of $Ti^{3+}$ ions in both rutile and anatase phases, upon removing O atoms from stoichiometric $TiO_2$. The presence of $Ti^{3+}$ ions can also be associated with the appearance of a new state in the band gap, ca. $0.7 - 0.9$ eV below the Fermi level ($E_F$) [40,41]. Electron spin resonance (ESR) observations (done on $TiO_2$ P-25 powder, having a mixed phase of anatase and rutile, in the ratio of 4:1) suggest that the trapped electrons are excited to the conduction band (CB) upon illumination of light, with energy lower than the band gap, and are re-trapped as $Ti^{3+}$ cations in the dark [42]. On the O-deficient/reduced rutile $TiO_2$(110) surface, with $Ti^{3+}$ ions present, studies have identified a non-vacancy-related $O_2$ dissociation channel, resulting in O adatom pairs [43]. This is in addition to the

$O_2$ dissociation channel that occurs at the O-vacancy site, which results in filled vacancies and isolated O adatoms [41].

Molecular oxygen ($O_2$) plays a key role in many $TiO_2$-based applications; e.g., $O_2$ adsorbed on $TiO_2$ surfaces is known to act as an electron scavenger, which is used to suppress electron − hole recombination in the photocatalytic reaction, and the first step of catalytic reactions, especially ORRs. Theoretical studies of $O_2$ adsorption on anatase surfaces have mostly focused on the (101) surface. The interaction between $O_2$ and other anatase surfaces, especially the active (001) surface still need further clarification. Besides, the studies of $O_2$ adsorption shows the disagreement between theoretical and experimental studies. The $O_2^{2-}$ anions were theoretically predicted to be more stable than the $O_2^-$ anions on the stable anatase $TiO_2$(101) [44–46]. This prediction seem to contradict with the observation of the $O_2^-$ stabilization from the electron paramagnetic resonance (EPR) experiment [47, 48].

All these reasons make anatase $TiO_2$(001) and the $O_2$ adsorption becomes interesting, not only for theoretical research, but also for a wide-range of applications, e.g., photocatalysis application, fuel cell, etc.

## 2.2 The Stoichiometric Anatase $TiO_2$(001)

### 2.2.1 Geometric Structure

The model of anatase $TiO_2$(001) started from an optimized bulk anatase $TiO_2$ structure. The corresponding calculated bulk lattice parameters are $a = b = 3.79(4)$ Å and $c = 9.51(5)$ Å, in good agreement with previous theoretical studies [21, 49].

A four layer slab of $TiO_2$ units was constructed with the $(2 \times 2)$ surface, consisting of 48 atoms: 16 Ti ions and 32 O ions, separated by 20 Å of vacuum space along [001], in a supercell geometry (cf. Fig. 2.2). The bottom two layers (of $TiO_2$ units) represent the bulk anatase $TiO_2$, and consist of 6-fold coordinated Ti ions ($Ti_{6c}$) and 3-fold coordinated O ions ($O_{3c}$). The top two layers (of $TiO_2$ units) represent the anatase

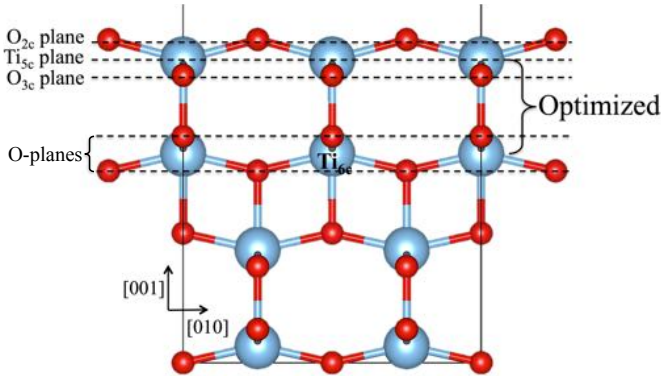


**Figure 2.2:** Side view (along $[\bar{1}00]$) of the slab model for anatase $TiO_2$(001)-$(2 \times 2)$.

$TiO_2(001)$. The unsaturated 5-fold coordinated Ti ions ($Ti_{5c}$) are located on the same plane, the Ti-plane, which is used as the reference plane for the adsorption process. The planes containing the 2-fold coordinated O (denoted as $O_{2c}$) and the 3-fold coordinated O (denoted as $O_{3c}$) are located above and below the Ti-plane, respectively. Thus, the topmost layer consists of three atomic layers, viz., the $O_{2c}$-, the $Ti_{5c}$- (or Ti-), and $O_{3c}$-planes, in order starting from the vacuum side. The top two layers (of $TiO_2$ units) are fully optimized, while the bottom two layers (of $TiO_2$ units) are fixed.

On the optimized anatase $TiO_2(001)$, the $O_{2c}$ are displaced outwards (0.016 Å), while the $O_{3c}$ and $Ti_{5c}$ relax inwards (0.038 Å and 0.068 Å, respectively). It results the bond lengths between the surface atoms: $r_{Ti_{5c}-O_{2c}} = 1.96$ Å and $r_{Ti_{5c}-O_{3c}} = 1.94$ Å. Each $O_{2c}$ binds equally to two $Ti_{5c}$, forming the subtended angle $\measuredangle(\mathrm{Ti}-\mathrm{O}-\mathrm{Ti}) = 149.9°$ (155.4° for the bulk). The anatase $TiO_2(001)$ is under tensile stress, as previously observed for bulk anatase and other anatase surfaces, attributed to the repulsion from the O atoms [21, 49]. Taking into account the structural symmetry of the system induced the preservation of structural symmetry breaking.

### 2.2.2 Electronic Properties

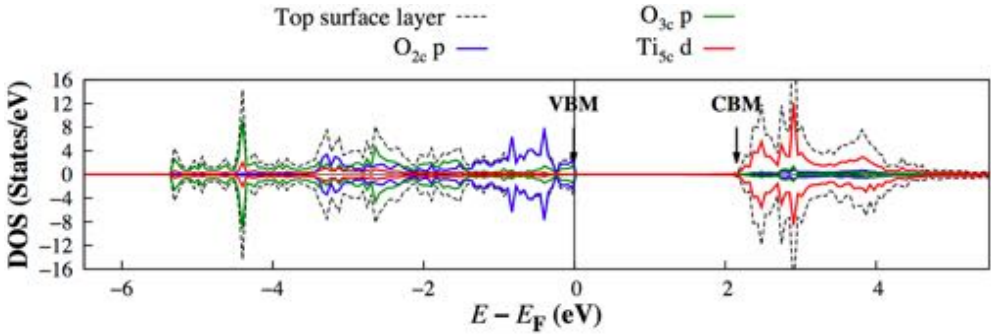


**Figure 2.3:** Calculated local density of states (LDOS) of the stoichiometric $TiO_2(001)$ The DOS contribution of the top surface layer was shown, and so the corresponding $p$ orbitals of the $O_{2c}$, $p$ orbitals of the $O_{3c}$ and $d$ orbitals of the $Ti_{5c}$. The arrows indicate the corresponding valence band maximum (VBM) and conduction band minimum (CBM). Energies given in [eV] with respect to the Fermi level ($E_F$).

The corresponding local density of states (LDOS) shows the gap of 2.1 eV between valence band (VB) maximum (VBM) and conduction band (CB) minimum (CBM). Anatase $TiO_2(001)$ shows the typical band gap of anatase within the framework of DFT studies [36, 50–52], which is well- known for the underestimation of LDA for the band gaps of semiconductors and insulators [53, 54].

The LDOS shows the main contribution from the surface $O_{2c}$ ions in the energy range from -1.5 eV to Fermi level ($E_F$) (cf., Fig. 2.3). Meanwhile, the surface $O_{3c}$ ions show the main contribution at lower energy range ([−5.4 eV, −1.5 eV], cf., Fig. 2.3). Since the unsaturated two-fold coordinated $O_{2c}$ ions are expected to be more reactive, they show the higher energetic states.

## 2.3 O-deficient/Reduced Anatase $TiO_{2-\delta}(001)$

### 2.3.1 O-vacancy Formation

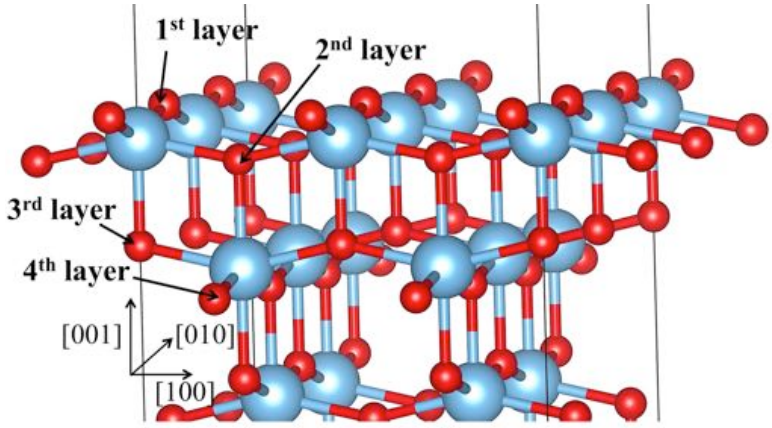


**Figure 2.4:** Four O-vacancy positions on anatase $TiO_2(001) - (2 \times 2)$, viz., in the $O_{2c}$ and $O_{3c}$ planes of the topmost layer and the O planes of the next layer (of $TiO_2$ units) (cf., Fig. 2.2). These are also alternatively labeled as $1^{st}$-, $2^{nd}$-, $3^{rd}$-, $4^{th}$-layers.

The feasibility of realizing such O-vacancies is evaluated with the corresponding calculated O-vacancy formation energy ($E_O^{\text{vacancy}}$), in terms of the difference in the corresponding energies for a stoichiometric anatase $TiO_2(001) - (2 \times 2)$ ($E^{\text{stoichiometric}}$) with that of a O-deficient/reduced surface ($E^{\text{reduced}}$) and a free O in the gas phase ($\frac{1}{2}E_{O_2}^{\text{gas}}$, cf., Eq. 2.1 [55, 56]), i.e.,

$$\begin{aligned} E_O^{vacancy} &= E^{reduced} - E^{stoichiometric} + \frac{1}{2}E_{O_2}^{gas} \\ &= E_{TiO_{2-\delta}} - E_{TiO_2} + \frac{1}{2}E_{O_2}^{gas} \end{aligned} \tag{2.1}$$

The computed $E_O^{\text{vacancy}}$ are shown in Table 2.1. The $O_{2c}$ plane shows the lowest O-vacancy formation energy for the creation of O-vacancy, $E_O^{\text{vacancy}} = 4.00$ eV, in agreement with previous studies [57]. The deeper we go into the bulk, starting from the $O_{2c}$-plane, to the $O_{3c}$ plane, and then the O planes (alternatively, the $1^{st}$-, $2^{nd}$-, $3^{rd}$-, $4^{th}$- layers, respectively, in Fig. 2.4), the larger the formation energy needed.

**Table 2.1:** Oxygen vacancy formation energy ($E_{\mathrm{O}}^{\mathrm{vacancy}}$, Eq. 2.1) in anatase $TiO_2(001) - (2 \times 2)$ (cf., Figs. 2.2 and 2.4).

| | $O_{2c}$-plane | $O_{3c}$-plane | O-plane | |
|---|---|---|---|---|
| Vacancy site | $1^{st}$ layer | $2^{nd}$ layer | $3^{rd}$ layer | $4^{th}$ layer |
| $E_{\mathrm{O}}^{\mathrm{vacancy}}$ [eV] | 4.00 | 4.77 | 4.76 | 4.96 |

### 2.3.2 Geometric Structure

On the O-deficient/reduced anatase $TiO_2(001)$, a missing O at $O_{2c}$ ($O_{2c}^{\mathrm{vacant}}$) breaks the symmetry, and generates two 4-fold coordinated Ti ions ($Ti_{4c}$ in Fig. 2.5). Thus, there are two $Ti_{4c}$ and two $Ti_{5c}$ ions per unit cell of O-deficient/reduced anatase $TiO_2(001)$. As shown in Table 2.2 (first column, $U = 0.0$ eV), the $Ti_{4c}$ ions move 0.13 Å into the bulk. The nearest $O_{2c}$ atom from the $O_{2c}^{\mathrm{vacant}}$ site ($O_{2c}^{\mathrm{1st}}$) moves outward 0.56 Å from surface, decreasing the subtended angle $\measuredangle(Ti_{4c} - O_{2c}^{\mathrm{1st}} - Ti_{4c}) = 98.75°$ and shortening the $Ti_{4c}$–$O_{2c}^{\mathrm{1st}}$ bond length to 1.83 Å (from 1.96 Å in the stoichiometric anatase $TiO_2(001)$). Meanwhile, the other $O_{2c}$, viz., the $2^{nd}$ nearest ($O_{2c}$) and the $3^{rd}$ nearest $O_{2c}$ ($O_{2c}^{\mathrm{3rd}}$) move slightly (0.02 Å and 0.09 Å, respectively) into the bulk. The $O_{3c}$ ions move slightly outwards (0.04 Å) from their initial positions. The presence of $O_{2c}^{\mathrm{vacant}}$ also breaks the equal proportionality/symmetry of the bonds between $O_{3c}$ and its two nearest Ti ions (Fig. 2.5). The two $O_{3c}$–Ti bonds, which were 1.94 Å in a stoichiometric (001) surface, become $Ti_{4c}$–$O_{3c}$ and $Ti_{5c}$–$O_{3c}$, with bond lengths 1.91 Å and 2.01 Å, respectively.

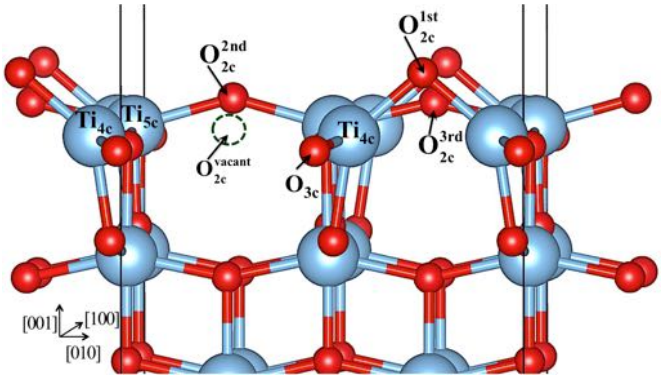


**Figure 2.5:** The O-deficient/reduced anatase $TiO_2(001)$ after relaxation. On the surface, there are two $Ti_{4c}$ near the $O_{2c}^{\mathrm{vacant}}$ site. $O_{2c}^{\mathrm{1st}}$, $O_{2c}^{\mathrm{2nd}}$, and $O_{2c}^{\mathrm{3rd}}$ represent the $1^{st}$, $2^{nd}$, and $3^{rd}$ nearest $O_{2c}$ from the $O_{2c}^{\mathrm{vacant}}$ site.

### 2.3.3 Electronic Properties

In bulk anatase, O-vacancy results in delocalized excess electrons [24, 51]. On the O-deficient/reduced anatase $TiO_2(001) - (2 \times 2)$, two excess electrons are created per O-vacancy ($O_{2c}^{\mathrm{vacant}}$). As shown in Table 2.2 (first column, on-site

**Table 2.2:** Displacement ($\Delta z$) along [001] from the stoichiometric surface, bond length ($r$), the subtended angle $\measuredangle(\mathrm{Ti}_{4c} - \mathrm{O}_{2c}^{1\mathrm{st}} - \mathrm{Ti}_{4c})$ and the charge gain/loss ($\pm\Delta Q$) due to the formation of $\mathrm{O}_{2c}^{\mathrm{vacant}}$ for the surface Ti (i.e., $\mathrm{Ti}_{4c}$ and $\mathrm{Ti}_{5c}$) and the surface O (i.e., $\mathrm{O}_{2c}^{1\mathrm{st}}$, $\mathrm{O}_{2c}^{2\mathrm{nd}}$, $\mathrm{O}_{2c}^{3\mathrm{rd}}$ and $\mathrm{O}_{3c}$), with various on-site Coulomb parameters $U$ (cf., Fig. 2.5). Negative values of $\Delta z$ correspond to displacement of the surface ions toward the bulk.

| $U$[eV] | 0.0 | 2.5 | 3.0 | 4.0 | 5.0 |
|---|---|---|---|---|---|
| $\Delta z_{\mathrm{Ti}_{4c}}$ [Å] | -0.13 | 0.00 | 0.04 | 0.07 | 0.10 |
| $\Delta z_{\mathrm{Ti}_{5c}}$ [Å] | -0.04 | 0.05 | 0.07 | 0.09 | 0.12 |
| $\Delta z_{\mathrm{O}_{2c}^{1\mathrm{st}}}$ [Å] | 0.56 | 0.55 | 0.59 | 0.64 | 0.69 |
| $\Delta z_{\mathrm{O}_{2c}^{2\mathrm{nd}}}$ [Å] | -0.02 | 0.12 | 0.14 | 0.18 | 0.22 |
| $\Delta z_{\mathrm{O}_{2c}^{3\mathrm{rd}}}$ [Å] | -0.09 | 0.02 | 0.04 | 0.07 | 0.10 |
| $\Delta z_{\mathrm{O}_{3c}}$ [Å] | 0.04 | 0.07 | 0.07 | 0.09 | 0.11 |
| $r_{\mathrm{Ti}_{4c}-\mathrm{O}_{2c}^{1\mathrm{st}}}$ [Å] | 1.83 | 1.86 | 1.87 | 1.88 | 1.89 |
| $r_{\mathrm{Ti}_{4c}-\mathrm{O}_{3c}}$ [Å] | 1.91 | 1.93 | 1.95 | 1.95 | 1.96 |
| $r_{\mathrm{Ti}_{5c}-\mathrm{O}_{2c}^{2\mathrm{nd}}}$ [Å] | 1.96 | 1.96 | 1.96 | 1.97 | 1.97 |
| $r_{\mathrm{Ti}_{5c}-\mathrm{O}_{2c}^{3\mathrm{rd}}}$ [Å] | 1.97 | 1.98 | 1.98 | 1.98 | 1.98 |
| $r_{\mathrm{Ti}_{5c}-\mathrm{O}_{3c}}$ [Å] | 2.00 | 1.97 | 1.97 | 1.97 | 1.97 |
| $\measuredangle(\mathrm{Ti}_{4c} - \mathrm{O}_{2c}^{1\mathrm{st}} - \mathrm{Ti}_{4c})$ [°] | 98.75 | 111.09 | 110.91 | 110.11 | 109.44 |
| $\Delta Q_{\mathrm{Ti}_{4c}}$ [$e$] | 0.32 | 0.35 | 0.36 | 0.38 | 0.39 |

Coulomb interaction parameter $U = 0.0$ eV), the $\mathrm{Ti}_{4c}$ gains almost all the excess electrons (ca. 0.32 e) due to $\mathrm{O}_{2c}^{\mathrm{vacancy}}$, leaving little to the other surface atoms, viz., $\mathrm{O}_{2c}^{1\mathrm{st}}$, $\mathrm{O}_{2c}^{2\mathrm{nd}}$, $\mathrm{O}_{2c}^{3\mathrm{rd}}$, $\mathrm{O}_{3c}$, and $\mathrm{Ti}_{5c}$. In the corresponding density of states (DOS) (Fig. 2.6b),the excess electrons localized at the two neighboring $\mathrm{Ti}_{4c}$, and appearing as defect states in the middle of the gap between the VBM and the CBM (cf., Figs. 2.6(a),(b)). Antiferromagnetic coupling between two $\mathrm{Ti}_{4c}$ ions created by spin polarisation of the intermediate $\mathrm{O}_{2c}^{1\mathrm{st}}$ to conform with the Pauli Exclusion Principle. These defect states locate near the $E_{\mathrm{F}}$, just below CBM. This result indicates that with standard Generalized Gradient Approximation (GGA) cannot clearly distinguish the experimentally observed the localized states in the band gap of the O-deficient/reduced anatase $\mathrm{TiO}_2$(001) [41, 42, 58, 59]. In order to accurately consider the position of the defect states in the electronic structure of anatase $\mathrm{TiO}_2$(001), additional calculations were performed with the on-site Coulomb interaction $U$ [60]

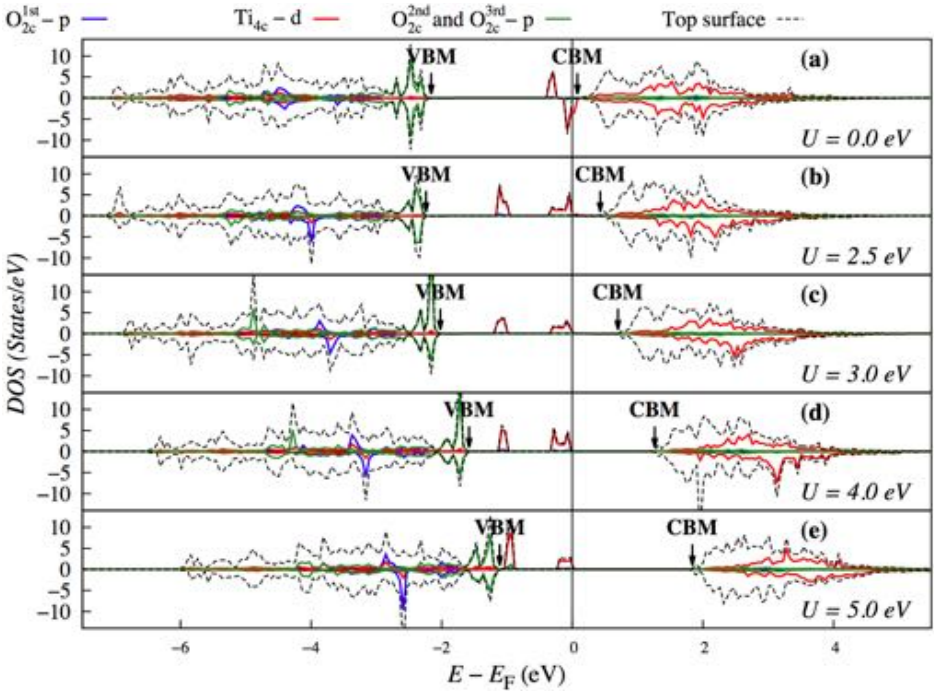


**Figure 2.6:** Calculated LDOS of the O-deficient/reduced $TiO_2(001)$ for several on-site Coulomb interaction values $U$: (a) 0.0 eV, (b) 2.4 eV, (c) 3.0 eV, (d) 4.0 eV, and (e) 5.0 eV. The DOS contribution from $d$-orbitals of the $Ti_{4c}$, $p$-orbitals of the nearest $O_{2c}$ ( i.e., $O_{2c}^{1st}$) and $p$-orbitals of the $2^{nd}$ and $3^{rd}$ nearest $O_{2c}$ ( i.e., $O_{2c}^{2nd}$ and $O_{2c}^{3rd}$) from the $O_{2c}^{vacant}$ site. The arrows indicate the corresponding VBM and CBM. Energies given in [eV] with respect to the Fermi level ($E_F$).

## On-site Coulomb interaction corrections:

As to be expected, the excess electrons change the distribution, which are mostly concentrated around the $d$ states of the $Ti_{4c}$ ions, and a modification of the $Ti_{4c}$–$O_{2c}^{1st}$ interaction. Table 2.2 shows how the corresponding changes of the surface Ti and O atom in the surface layer and the charge transfer from $O_{2c}^{vacant}$ varies with $U$. The $Ti_{5c}$–$O_{2c}^{2nd}$ and $Ti_{5c}$–$O_{2c}^{3rd}$ bonds are only slightly modified. Meanwhile, the optimized O-deficient/reduced anatase $TiO_2(001)$, computed with GGA+$U$ shows an outward displacement of all surface atoms, elongating and releasing the tensile stress of the surface. This displacement results in the enhancement of the repulsion from the surface $O_{2c}$ ions on the O-deficient/reduced anatase $TiO_2(001)$.

Figs. 2.6(c)-(f) show how the corresponding DOS changes with $U$. Firstly, most of the charge transfer still occur near $Ti_{4c}$, in the vicinity of $O_{2c}^{vacant}$. Next, the inclusion of $U$ weakens the exchange interaction and elongates the bond length of of $Ti_{4c}$–$O_{2c}^{1st}$. It changes the magnetic coupling between the two $Ti_{4c}$ atoms, from antiferromagnetic (cf., Fig. 2.6(b)) to ferromagnetic (cf., Fig. 2.6(c)-(f)).

The LDOS of the surface $O_{2c}$, especially the $O_{2c}^{1st}$, become more localized. As

increasing $U$, CB shifts further away from $E_F$, whereas valence band (VB) shifts towards $E_F$. The defect states appearing in the gap between VBM and CBM, near $E_F$, in turn, shifts towards VBM. With $U = 4.0$ eV (Fig. 2.6e), the defect states are located ca. 1.25 eV below CBM. With $U = 5.0$ eV (Fig. 2.6f), the defect states are located ca. 1.84 eV below CBM. Based on previous experimental [46,58,59,61–63] and theoretical [39] studies, $U = 4.0$ eV could well-describe the localized states of the O-deficient/reduced anatase $TiO_2(001)$.

## 2.4 The $O_2$ Adsorption

The stability of the adsorption configuration is evaluated by the corresponding calculated adsorption energy $E_{ads}$, in terms of the difference in the corresponding energies for the surface after adsorbing $O_2$ ($E_{O_2/surf}$) and the isolated surface ($E_{surf}$) and $O_2$ ($E^{gas}_{O_2}$, in the triplet ground state [55,56]), i.e.,

$$E_{ads} = E_{O_2/surf} - [E_{surf} + E^{gas}_{O_2}]. \tag{2.2}$$

### 2.4.1 On the stoichiometric anatase $TiO_2(001)$

The concentration of 0.25 monolayer (0.25 ML) was considered for the $O_2$ adsorption. $O_2$ can be adsorbed on four sites, in five stable adsorption configurations, as shown in Fig. 2.7. Table 2.3 shows the computed adsorption energy ($E_{ads}$,

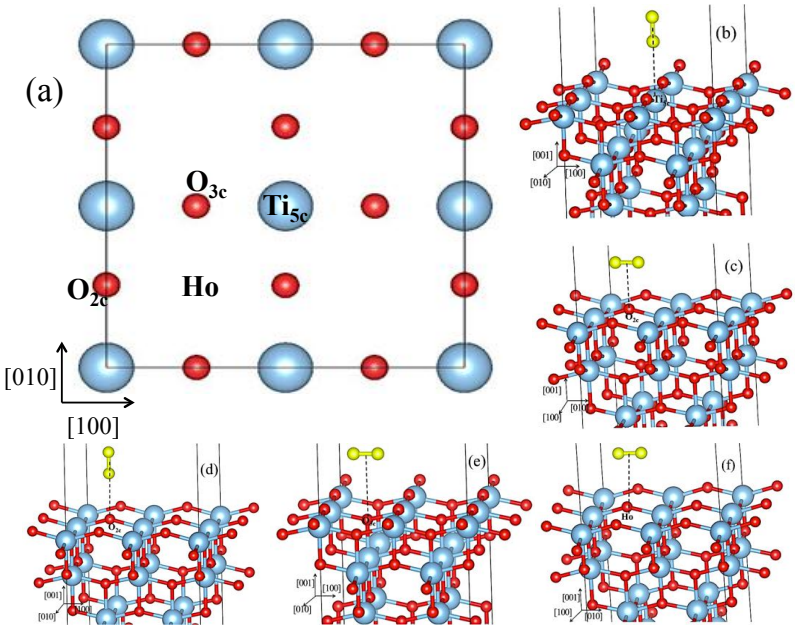


**Figure 2.7:** (a) Top view of a stoichiometric anatase $Ti0_2(001)$, with the corresponding symmetric sites, viz., atop $Ti_{5c}$; $O_{2c}$; $O_{3c}$; and Ho: the hollow site. Also shown are the stable configurations for an incoming $O_2$: (b) atop $Ti_{5c}$, with the O-O bond along [001]; (c) atop $O_{2c}$, with the O-O bond along [010]; (d) atop $O_{2c}$, with the O-O bond along [001]; (e) atop $O_{3c}$, with the O-O bond along [100]; and (f) atop Ho, with the O-O bond along [010].

Eq. 2.2), bond length of adsorbed $O_2$ ($r_{O-O}$), and amount of charge transfer ($\Delta Q$) from anatase $TiO_2$(001) to the adsorbed $O_2$ at each of the five stable adsorption configurations/sites. All five configurations show positive $E_{ads}$, indicating that $O_2$ cannot adsorb on the stoichiometric anatase $TiO_2$(001) surface, for all four sites and five configurations considered. The most stable configuration, with $E_{ads} = 0.37$ eV, corresponds to $O_2$ center-of-mass (CM) located atop $O_{2c}$, with the O-O bond oriented parallel to the surface along [010] (Fig. 2.7c). Adsorption at other sites, e.g., $O_2$ CM atop $Ti_{5c}$ with the O-O bond oriented perpendicular to the surface along [001] (Fig. 2.7b), $O_2$ CM atop $O_{2c}$ with the O-O bond oriented perpendicular to the surface along [001] (Fig. 2.7d), and $O_2$ CM atop $O_{3c}$ with the O-O bond oriented parallel to the surface along [100] (Fig. 2.7e) have quite similar endothermic $E_{ads}$. The most endothermic corresponds to $O_2$ adsorption at the hollow site (Ho), with the O-O bond oriented parallel to the surface along [010] (Fig. 2.7f). At all the four sites, the O-O bond length of the adsorbed $O_2$ is longer than the corresponding gas phase bond length $r^{gas}_{O-O} = 1.21$ Å [64]. Bader charge analysis [65] also shows that the adsorbed $O_2$ does not have charge transfer with the stoichiometric surface. The adsorbed $O_2$ retains a triplet spin state, as $O_2$ does in the gas phase [55, 56].

**Table 2.3:** Computed adsorption energy ($E_{ads}$, Eq. 2.2) of $O_2$ on the stoichiometric $TiO_2$(001), bond length of the adsorbed $O_2$ ($r_{O-O}$), and amount of charge transfer ($\Delta Q$) from anatase $TiO_2$(001) to the $O_2$ adsorbed at each of the five stable adsorption configurations/sites, viz., $Ti_{5c}$, $O_{2c}$[010], $O_{2c}$[001], $O_{3c}$, and Ho (cf., Fig. 2.7.). A positive value of $E_{ads}$ correspond to the endothermic adsorption of $O_2$.

| Site | $Ti_{5c}$ | $O_{2c}$[010] | $O_{2c}$[001] | $O_{3c}$ | Ho |
|---|---|---|---|---|---|
| $E_{ads}$ [eV] | 0.55 | 0.37 | 0.54 | 0.53 | 0.98 |
| $r_{O-O}$ [Å] | 1.23 | 1.24 | 1.23 | 1.23 | 1.23 |
| $\Delta Q$ [e] | 0.02 | 0.04 | 0.01 | 0.01 | 0.01 |

Repulsion of the surface O ions plays a significant role in deciding the structure of anatase surfaces [21]. It also induces the repulsive force with the coming $O_2$ molecule, and becomes the reason why it is difficult for the $O_2$ to adsorb on the stoichiometric surface. It explains the endothermic adsorption on the stoichiometric surface. In order to make adsorption favorable on this surface, it is necessary to decrease the O-O repulsion on the surface, and the easiest way to do that is to reduce the number of surface O atoms, i.e., by forming O-vacancies on the surface.

### 2.4.2 On the O-deficient/Reduced Anatase $TiO_{2-\delta}(001)$

Since the excess electrons are localized at $Ti_{4c}$, the neighboring O-vacancy site, i.e., $O_{2c}^{vacant}$, can be considered as the active site for $O_2$ adsorption. It is confirmed that unconstrained $O_2$ adsorption only occurs at $O_{2c}^{vacant}$, and $O_2$ cannot chemically absorb on the other sites on the O-deficient/reduced anatase $TiO_2(001)$. This agrees with earlier studies [59]. We have also identified two relevant adsorption configurations, viz., $O_2$ located atop the O-vacancy site, with O-O bond oriented parallel to the surface along [010], viz., A1 configuration (cf., Fig. 2.8), and perpendicular to the surface along [001], viz., A2 configuration (cf., Fig. 2.9).

**A1 Configuration: O-O bond along [010] (cf., Fig. 2.8)**

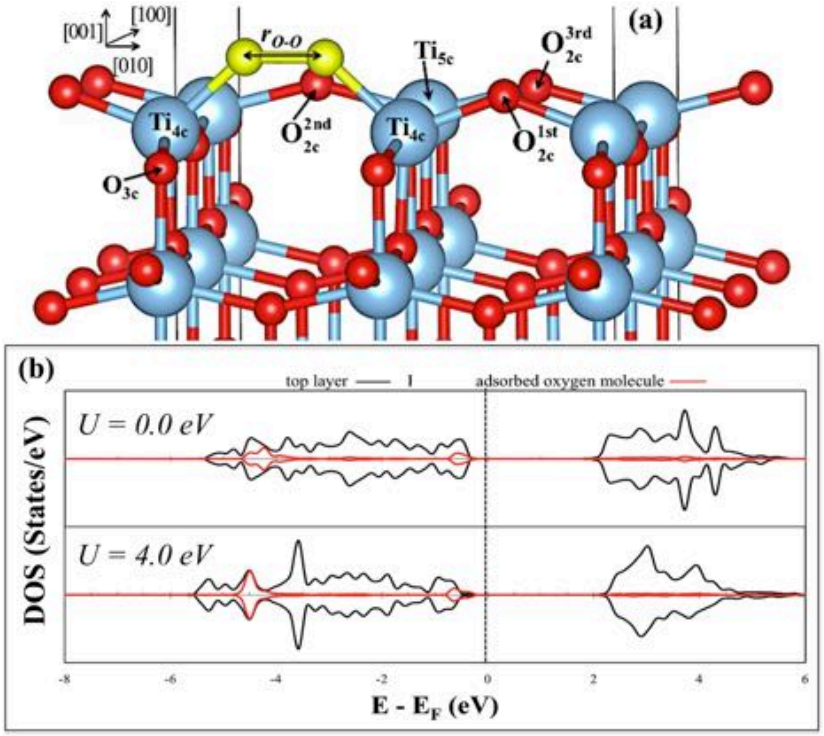


**Figure 2.8:** (a): Optimized structure of the A1 adsorption configuration at the O-vacancy site: $O_2$ adsorbs with the O-O bond parallel to the surface along the [010] direction. (b): Calculated DOS of the top layer of the O-deficient/reduced anatase $TiO_2(001)$ after oxygen adsorption in A1 configuration with standard GGA ($U = 0$ eV) calculations and GGA+$U$ ($U = 4$ eV) calculations. Energies given in [eV] with respect to the Fermi level ($E_F$).

With $O_2$ located atop the O-vacancy site, and the O-O bond oriented parallel to the surface along [010], $E_{ads} = -4.82$ eV. This indicates very stable $O_2$ adsorption in the A1 configuration on the O-deficient/reduced anatase $TiO_2(001)$. The $O_2$ binds with the $Ti_{4c}$, at an O$-Ti_{4c}$ distance of 1.87 Å, and gains $\Delta Q = 1.028$e

from the surface, to form a superoxide anion ($O_2^-$). In this adsorbed $O_2^-$ state, $r_{O-O}(O_2^-)$ = 1.37 Å and the stretching frequency $\nu_{O-O}(O_2^-)$ = 1049.7 cm$^{-1}$. This result can compare this with the $O_2^-$ intermediates observed in ORRs on Pt electrodes by SE-IRAS with attenuated total reflection [66,67], with $r_{O-O}(O_2^-)$ = 1.37 Å and $\nu_{O-O}(O_2^-)$ = 1016 cm$^{-1}$. This suggests that anatase could be a promising alternative catalyst in the ORRs. In comparison, on (101), the adsorbed $O_2$ can be observed in the peroxide state ($O_2^{2-}$) with the same $O_2$ coverage [44–46]. The results are in good agreement with experimental studies of anatase particles using EPR spectroscopy [47, 48]. The dissociation of adsorbed oxygen could not be realized on this surface, even with the presence of O-vacancy, which agrees with the experimental results from STM studies [59]. In the O-deficient/reduced anatase $TiO_2$(001), the defect states disappear upon $O_2$ adsorption, for both GGA and GGA+$U$ results (cf., Figs. 2.8b). The adsorbed $O_2$ locates stable on the surface.

**Table 2.4:** Computed adsorption energy ($E_{ads}$, Eq. 2.2) of $O_2$ on the O-deficient/reduced $TiO_2$(001), bond length of the adsorbed $O_2$ ($r_{O-O}$), the stretching frequency ($\nu_{O-O}$), and charge gain/loss ($\pm\Delta Q$) by the neighboring Ti and O atoms on O-reduced surface due to the adsorption of $O_2$, for various on-site Coulomb parameters $U$ (cf., Fig. 2.8 and Fig. 2.9).

| | A1 configuration | | A2 configuration | |
|---|---|---|---|---|
| $U$[eV] | 0.0 | 4.0 | 0.0 | 4.0 |
| $E_{ads}$ [eV] | −4.82 | −4.08 | −4.00 | −3.36 |
| $r_{O-O}$ [Å] | 1.37 | 1.39 | 1.47 | 1.48 |
| $\nu_{O-O}$ [cm$^{-1}$] | 1049.7 | 1033.1 | 908.0 | 888.5 |
| $\Delta Q_{Ti_{4c}}$ [$e$] | −0.3 | −0.36 | −0.32 | −0.42 |
| $\Delta Q_{O_2^{adsorbed}}$ [$e$] | 1.03 | 1.08 | 1.23 | 1.3 |

The calculations results for $U$ = 0.0 and 4.0 eV differ only in the corresponding $E_{ads}$ (cf., Table 2.4). For both $U$ = 0.0 and 4.0 eV, A1 configuration is observed as the most stable adsorption configuration. As mentioned earlier, there is an enhancement of the repulsion from the surface O ions on the O-deficient/reduced surface, within the GGA+$U$ calculations. It interferes slightly with the creation of bond between the incoming $O_2$ and the $Ti_{4c}$ ions. As a result, a lower $E_{ads}$ is expected from GGA+$U$ calculations for anatase $TiO_2$(001), i.e., $E_{ads}$ = −4.08 eV (cf., Table 2.4). In the A1 configuration, GGA+$U$ calculations indicate that the $O_2$ still has $O_2^-$ character, with $r_{O-O}(O_2^-)$ = 1.39 Å and $\nu_{O-O}(O_2^-)$ = 1033.1 cm$^{-1}$.

**A2 Configuration: O-O bond along [001] (cf., Fig. 2.9)**

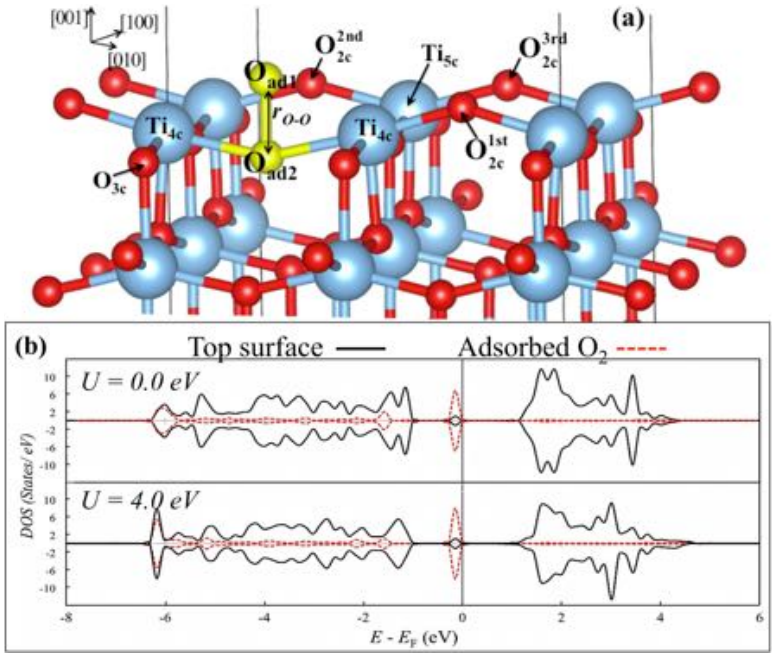


**Figure 2.9:** (a): Optimized structure of the A2 adsorption configurations at the O-vacancy site: $O_2$ adsorbs with the O-O bond perpendicular to the surface along the [001] direction. In the A2 configuration, the bottom O ($O_{ad1}$) of $O_2$ protrudes from the surface, and the top O ($O_{ad2}$) is near the $Ti_{4c}$-plane. (b): Calculated DOS of the top layer of the O-deficient/reduced anatase $TiO_2$(001) after oxygen adsorption in A2 configuration with standard GGA ($U = 0$ eV) calculations and GGA+$U$ ($U = 4$ eV) calculations. Energies given in [eV] with respect to the Fermi level ($E_F$).

With $O_2$ located atop $O^{vacant}_{2c}$, and the O-O bond oriented perpendicular to the surface along [001], $E_{ads} = -4.00$ eV. This also indicates stable $O_2$ adsorption in the A2 configuration on the O-deficient/reduced anatase $TiO_2$(001). In this configuration, $O_2$ tends to come closer to the $Ti_{4c}$-plane, and the lower O atom fills up the O-vacancy site and bonds with two $Ti_{4c}$ ions, at a O$-$$Ti_{4c}$ distance of 2.02 Å, cf., Fig. 2.9. Compared to the A1 configuration, the A2 configuration exhibits a larger charge transfer $\Delta Q = 1.23$e from the two $Ti_{4c}$ ions, as shown in Table 2.4. In both the A1 and A2 configurations, there is negligible (one order of magnitude less) charge transfer between the incoming $O_2$ with the oxygen ions far from the $O^{vacant}_{2c}$, viz., $O_{2c}$ and $O_{3c}$. Most of the charges transfer come from the $Ti_{4c}$ ions to the adsorbed $O_2$. This indicates the critical role of the excess electrons on $Ti_{4c}$, which is due to the O-vacancy at $O_{2c}$, in making $O_2$ adsorption on this surface more favorable.

In this A2 configuration, the adsorbed $O_2$ forms a peroxide state ($O_2^{2-}$), with $r_{O-O}(O_2^{2-}) = 1.47$ Å and $\nu_{O-O}(O_2^{2-}) = 908.0$ cm$^{-1}$. This results again can com-

pare this with the $O_2^{2-}$ observed on Pt(111) [67–70], with $r_{O-O}(O_2^{2-}) = 1.47$ Å and $\nu_{O-O}(O_2^{2-}) = 870$ cm$^{-1}$. The dissociation is also unfavorable on this surface. Within the GGA+$U$ calculations, the A2 configuration also found to be unstable, as compared to A1. In the A2 configuration, a lower $E_{ads}$ is also observed, however, the $O_2^{2-}$ character persists, with $r_{O-O}(O_2^{2-}) = 1.48$ Å and $\nu_{O-O}(O_2^{2-}) = 888.5$ cm$^{-1}$. In the discussion in previous section (Sec. 2.3.3), the GGA+$U$ calculations give a better description of the energetic position of the defect states (in electronic structure) of the O-deficient/reduced anatase $TiO_2$(001). However, there seem to be no significant direct correlation between the location of the defect states with the corresponding $E_{ads}$, $r_{O-O}$, and $\Delta Q$. Furthermore, similar to A1 configuration, the defect states disappear upon $O_2$ adsorption on the O-deficient/reduced anatase $TiO_2$(001), for both GGA and GGA+$U$ results (cf., 2.9b). This attenuation of the defect peak signal after oxygen adsorption has also been observed by resonant photoemission spectroscopy [58].

From Table 2.4, we see that almost all the excess electrons, which $Ti_{4c}$ ions gained from the $O_{2c}^{vacant}$, transfer to incoming the $O_2$, and occupy the $\pi^*$ antibonding states of the adsorbed $O_2$, with corresponding energy levels located just below $E_F$. DOS calculated with GGA+$U$ are more localized than those calculated with GGA. However, both GGA and GGA+$U$ calculations do not show any significant difference in electronic structure of the system after molecular adsorption. The adsorbed $O_2$ shares a strong bond with the nearest Ti ions on the O-deficient/reduced $TiO_2$(001). Due to the missing surface $O_{2c}$, the two neighboring Ti ions gain excess electrons. These excess electrons enable the Ti ions to attract the incoming $O_2$. As the result, $O_2$ can easily adsorb on this surface.

### 2.4.3 Healing/ Migration effect

Although the A2 configuration is not as stable as the A1 configuration, the A2 configuration cannot relax to the A1 configuration. Moreover, in the optimized A2 configuration, $\measuredangle(Ti_{4c} - O_{ad1} - Ti_{4c})$ subtends an angle of 155.5°, and $\measuredangle(Ti_{4c} - O_{2c}^{1st} - Ti_{4c}$ has a subtended angle of 146.8°, which is close to that of a stoichiometric anatase $TiO_2$(001) (i.e., 149.9°). According to our calculations, the stoichiometric anatase $TiO_2$(001), with an O adatom at the $O_{2c}$ site is around 0.5 eV more stable than the O-deficient/reduced anatase $TiO_2$(001) with $O_2$ in A2 configuration. This implies that one O from the incoming $O_2$ can fill the O-vacancy of the O-deficient/reduced anatase $TiO_2$(001), *healing* the O-deficient/reduced surface, while the other O atom may become an O adatom and migrates to other sites, on the *healed* stoichiometric surface. The *healing* effect

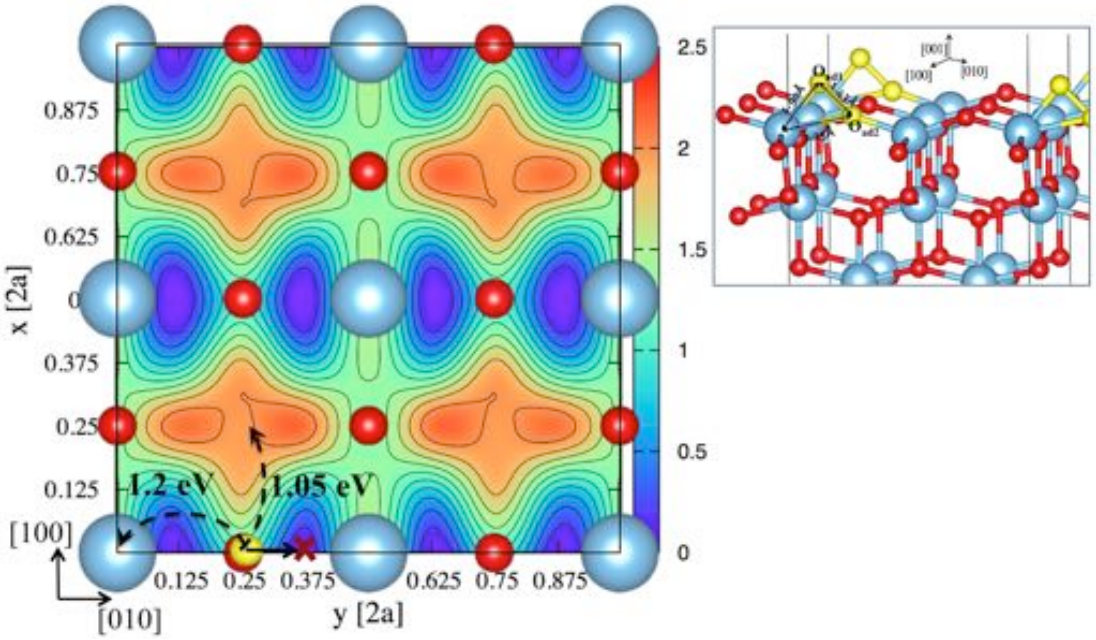


**Figure 2.10:** Potential energy surface for O adatom diffusion on the stoichiometric $TiO_2(001)$. The coordinates $(x, y)$ of the O adatom are given as fractional units of the $(2 \times 2)$ surface. The top-view and the symmetric sites correspond to Figure 2.7. (Inset) The configuration corresponding to the case when the O adatom is at a minima above $(x, y) = (0, 0.125)$. O adatom: smaller/yellow sphere. Contour spacing: 0.15 eV. Surface lattice parameter $a = 3.79(4)$ Å.

of the incoming $O_2$ corresponds to the disappearance of point defects observed in STM studies [59]. This behavior is also observed on rutile $TiO_2(110)$ [7] and anatase $TiO_2(101)$ [71].

Nevertheless, the potential energy surface (PES) for O adatom diffusion on the stoichiometric anatase $TiO_2(001)$ shows that O adatom can move to the position at the middle of the $Ti_{5c}$-$O_{2c}$ bond without any barrier (Fig. 2.10). The configuration corresponding to the case when the O adatom is at a local minima above the middle of the $Ti_{5c}$-$O_{2c}$ bond can also be seen in oxygen evolution reaction (OER) [72]. It takes around 1.2 eV for the O adatom to migrate to the nearest $Ti_{5c}$ site, and around 1.05 eV to migrate to the nearest hollow site (Ho). Healing/migration effect of the O adatom on the stoichiometric anatase $TiO_2(001)$ reduces the efficiency of the surface chemical reactions, and hence, slows down the rate of ORRs. In this situation, the A2 configuration would show a decreased rate in chemical reactions on the anatase $TiO_2((001)$.

## 2.5 Summary

We performed DFT-based calculations to investigate the effect of O-vacancy on the electronic structure and the adsorption of oxygen on anatase $TiO_2(001) - (2 \times 2)$. Our calculation results show that the stoichiometric anatase $TiO_2(001)$ does

not favour $O_2$ adsorption. O-vacancies play an important role in the improvement of $O_2$ adsorption on this surface. The absence of 2-fold coordinated O ($O_{2c}$) ion on the surface leads to excess electrons. These excess electrons redistribute locally around the two neighboring 4-fold coordinated Ti ions ($Ti_{4c}$), and an associated localized defect state appears in the corresponding electronic structure. The localized defect state can be described well with GGA+$U$. However, regardless of the value of $U$ considered, we find no significant qualitative change in the results of the $O_2$ adsorption on this surface. On the O-deficient/reduced anatase $TiO_2(001)$, the O-vacancy sites become active sites, making $O_2$ adsorption favorable and exothermic. Here, we considered two adsorption configurations, viz., $O_2$ adsorbs at the O-vacancy with the O-O bond oriented parallel to the surface along the [010] (A1 configuration), and with the O-O bond oriented perpendicular to the surface along [001] (A2 configuration). In the A1 configuration, the incoming $O_2$ adsorbs with a superoxide state ($O_2^-$). In the A2 configuration, the incoming $O_2$ adsorbs with a peroxide state ($O_2^{2-}$). Both results for the adsorbed states of $O_2$ in the corresponding A1 and A2 configurations agree with previous results observed for oxygen adsorption on Pt surfaces [48, 67, 69]. The $O_2^-$ states of adsorbed $O_2$ are more stable than the $O_2^{2-}$ states of adsorbed $O_2$. With the less stable A2 configuration, *healing* of the O-deficient/reduced anatase $TiO_2(001)$ can take place, where one adsorbed O atom fills the O-vacancy and the other becomes an O adatom on the healed surface. The O adatom can migrate easily to positions in the middle of the Ti−O bond along [010], but it is difficult for the O adatom to migrate to other positions. It could reduce the efficiency of the surface chemical reactions and slow down the reaction rate. However, the healing/migrate effect has less probability to occur than the $O_2$ adsorption in $O_2^-$ states. It indicates that the introduction of O-vacancy significantly improve the $O_2$ adsorption on anatase $TiO_2(001)$, which is considered as an important first step of ORRs.

# Chapter 3

# O-vacancies in Pristine Lanthanum Gallate Based Materials

## 3.1 LG-based materials

Perovskite materials have been used in several green-technology applications because of their interesting physical properties, e.g., ferroelectric, magnetic, optical properties, etc. These materials show drastic changes in their physical properties even with a slight modification of the structure by defect inclusion, chemical substitution, or by an altered external condition, etc. Lanthanum gallate, $LaGaO_3$ (LG), is one such perovskite with a $GdFeO_3$-type structure. These materials represent a family of perovskites [73, 74] that exhibit ionic conductivity and find use in various application, e.g., as electrolytes in solid oxide fuel cells (SOFCs) applications [75–80].

Pristine LG shows the phase transition of LG, i.e., from an orthorhombic ($Pnma$) to rhombohedral ($R\bar{3}c$) structure, observed experimentally at 425K by the powder neutron diffraction [81]. And, it was confirmed in a large number of later reports [82–86]. In the low symmetry orthorhombic phase of LG, the [$GaO_6$] octahedral substructures are tilted from the ideal cubic perovskite structure, with the La atoms occupying the hollow site in between the [$GaO_6$] octahedrons [82]. Judging from the geometric structure, interstitial oxygen cannot be expected in this system, and studies indicate that introduction of interstitial oxygen in perovskite structure would indeed be thermodynamically unfavourable [4]. Instead, O migration through LG-based material would be through O-vacancies. O-vacancies has key role in LG-based materials for the desired O-migration. This study focuses on the role of O-vacancies in the material as related to O migration, which is an important factor for ionic conductivity.

## 3.2 The Pristine/ Stoichiometric LG

### 3.2.1 Geometric Structure

The optimized structure of the pristine/stoichiometric LG is showed in Fig. 3.1 with the preservation of *Pnma* symmetry. The [$GaO_6$] octahedrons are tilted from their ideal cubic perovskite structure, when viewed along the *b*-axis (cf., Fig. 3.1(b)). The calculated lattice parameters: $a = 5.58(3)$ Å, $b = 7.87(4)$ Å, and

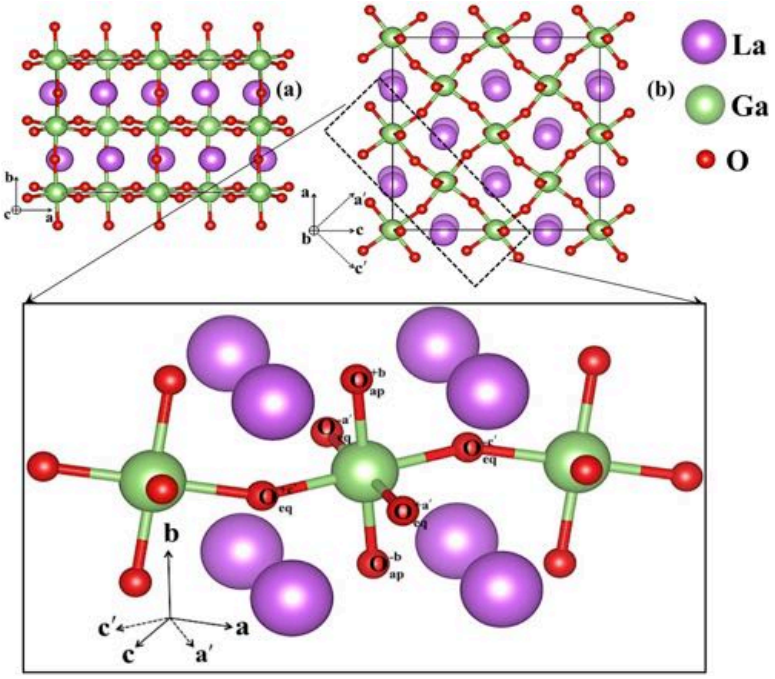


**Figure 3.1:** The optimized structure of the stoichiometric LG as viewed from (a) the *c*-axis and (b) the *b*-axis, and (c) a magnified view of the [$GaO_6$] octahedron of the supercell. The ($2 \times 1 \times 2$) supercell contains 80 atoms: 16 La, 16 Ga, and 48 O. The corresponding coordinate axes ($a, b, c$ and $a', c'$) are also shown.

$c = 5.56(2)$ Å, agree with experimental observations, with errors within 2%. [83–87] LG contains 6-fold O-coordinated Ga ions ($Ga_{6c}$), 8-fold Ga-coordinated O ions ($O_{8c}$) and 12-fold O-coordinated La ions ($La_{12c}$) (cf., Fig. 3.1). The [$GaO_6$] octahedron contains two apical O ions (viz., $O_{ap}^{+b}$ and $O_{ap}^{-b}$, which lie along the [010] direction), and four equatorial O ions (viz., $O_{eq}^{+c'}$, $O_{eq}^{-c'}$ along [101] and $O_{eq}^{+a'}$, $O_{eq}^{-a'}$ along [−100]) (cf., Fig. 3.1(c)).

Bond lengths $r_{Ga-O_{ap}^{\pm b}} = 2.02(1)$ Å, $r_{Ga-O_{eq}^{\pm c'}} = 2.01(1)$ Å, and $r_{Ga-O_{eq}^{\pm a'}} = 2.02(1)$ Å for the two apical O ions and the four equatorial O ions, respectively. Subtended angles $\measuredangle(O_{ap}^{+b} - Ga - O_{eq}^{+a'}) = \measuredangle(O_{ap}^{-b} - Ga - O_{eq}^{-a'}) = 89.87°$ and $\measuredangle(O_{ap}^{+b} - Ga - O_{eq}^{+c'}) = \measuredangle(O_{ap}^{-b} - Ga - O_{eq}^{-c'}) = 88.96°$. The calculated small deviations in $\measuredangle(O_{ap} - Ga - O_{eq})$ from that of the ideal octahedron, i.e., 90°, is

consistent with reported solid-state NMR studies. [88] As mentioned earlier, these deviations indicate that the [$GaO_6$] octahedrons are tilted from their ideal cubic perovskite crystal structure. The tilting of the [$GaO_6$] octahedrons occurs around the *b*- and *c*-axes, in good agreement with previous experimental observations. [81, 85, 88] Similarly, the calculated $\measuredangle(\mathrm{Ga} - \mathrm{O_{eq}} - \mathrm{Ga}) = 155.80°$ and $\measuredangle(\mathrm{Ga} - \mathrm{O_{ap}^{\pm b}} - \mathrm{Ga}) = 154.85°$, are in agreement with the experimental results. [81]

### 3.2.2 Electronic Properties

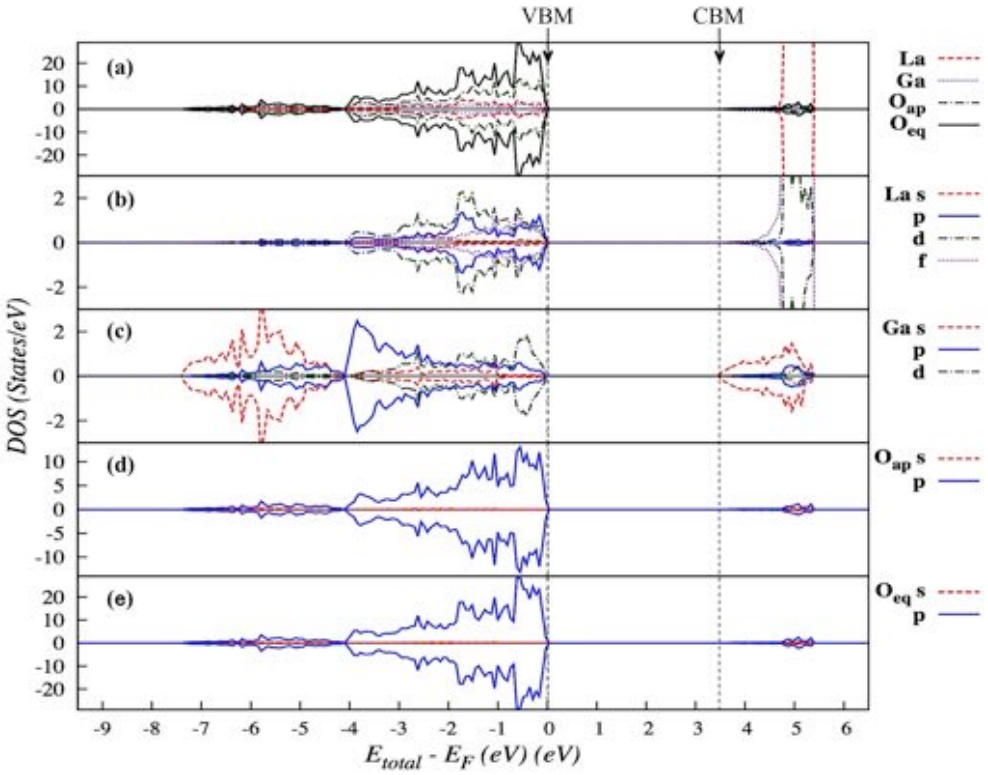


**Figure 3.2:** Calculated LDOS of the stoichiometric $LaGaO_3$ (LG). (a) DOS for whole ($2 \times 1 \times 2$) super-cell with the DOS contributions from lanthanum (La), gallium (Ga), apical oxygen ($O_{ap}$), and equatorial oxygen ($O_{eq}$), respectively. (b)-(e) DOS contributions from the *s*, *p*, *d*, and *f*-orbitals of La, Ga, $O_{ap}$, and $O_{eq}$, respectively. Energies are given in [eV] with respect to the Fermi level ($E_F$). The corresponding VBM and CBM are also indicated.

The corresponding LDOS of the stoichiometric LG (cf., Fig. 3.2) shows that the system is non-magnetic and insulating. The gap between the VBM and the CBM is $\sim 3.31$ eV. The main contribution to the VB comes from the O atoms, viz., $O_{ap}$ and $O_{eq}$ ions. A weak La-O covalent interaction is indicated by the corresponding relatively shallow *d*-*p* and *p*-*p* hybridizations (cf., [$-2$ eV,$-0.5$ eV] and [$-2$ eV, $E_F$], respectively, in Figs. 3.2(b),(d),(e)). Besides, La ions bond more strongly with the $O_{ap}$ ions than with the $O_{eq}$ ions (cf., Figs. 3.2(b),(d),(e)).

The difference of La-O hybridization will become important to decide the stable position of O-vacancy (cf., Sec. 3.3.1). The Ga-O *d*-*p* hybridization is similar to that of La-O, shallow [−2 eV, $E_{\rm F}$]. However, we observe a relatively stronger Ga-O covalent interaction, as indicated by the corresponding relatively deep *s*-*p* and *p*-*p* hybridizations (cf., [−7 eV,−4.2 eV] and [−4.2 eV, −2 eV], respectively, inFig. 3.2(c),(d),(e)).

## 3.3 O-deficient/Reduced $LaGaO_{3-\delta}$ ($LG_{-\delta}$)

### 3.3.1 O-vacancy Formation

To study the role of O-vacancies on the the structural and electronics properties of LG, we considered six possible O-vacancy configurations/locations, viz., the locations of the two apical O ions ($O_{\rm ap}^{\pm b}$) and the four equatorial O ions ($O_{\rm eq}^{\pm a'/c'}$) (cf., Fig. 3.1).

Following Ref. [89], to evaluate the feasibility of realizing such O-vacancies, we calculate the corresponding O-vacancy formation energy ($E_{\rm O}^{vacancy}$) in terms of the difference in the corresponding energies for a stoichiometric LG ($E^{stoichiometric} = E_{\rm LG}$) with that of a reduced (O-deficient) LG ($E^{reduced} = E_{{\rm LG}_{-\delta}}$) and a free O in the gas phase ($\frac{1}{2}E_{\rm O}^{gas}$, cf., Refs. [55, 56]), i.e.,

$$\begin{aligned} E_{\rm O}^{vacancy} &= E^{reduced} - E^{stoichiometric} + \frac{1}{2}E_{\rm O_2}^{gas} \\ &= E_{{\rm LG}_{-\delta}} - (E_{\rm LG} + \frac{1}{2}E_{\rm O_2}^{gas}) \end{aligned} \tag{3.1}$$

Table 3.1 shows the computed $E_{\rm O}^{vacancy}$. As expected (cf., Sec. 3.3.3), it would be harder to remove $O_{\rm ap}$, because of the relatively stronger covalent bonding of the $O_{\rm ap}$ with surrounding cations, as compared to $O_{\rm eq}$. Furthermore, the large values of $E_{\rm O}^{vacancy}$ also confirms that it is difficult to create O-vacancy in the pure LG, in agreement with previous reports. [90]

**Table 3.1:** Calculated O-vacancy formation energy ($E_{\rm O}^{vacancy}$, Eq. 3.1) in $LaGaO_3$ (LG) for the apical $O_{\rm ap}^{\pm b}$ ions along the *b*-axis and the equatorial $O_{eq}^{\pm c'}$ and $O_{eq}^{\pm a'}$ ions along the *c*- and *a*-axes, respectively (cf., Fig. 3.1).

| | apical O ions ($O_{\rm ap}$) | equatorial O ions ($O_{\rm eq}$) | |
|---|---|---|---|
| Vacancy site | $O_{\rm ap}^{\pm b}$ | $O_{\rm eq}^{\pm c'}$ | $O_{\rm eq}^{\pm a'}$ |
| $E_{\rm O}^{vacancy}$ [eV] | 5.70 | 5.65 | 5.66 |

### 3.3.2 Geometric Structure

The introduction of O-vacancy ($O^{vac}$) in LG creates two unsaturated [$GaO_5$] pyramids near the vacancy site with two 5-fold coordinated Ga ions, viz., $Ga_{5c}^{+c'}$ and $Ga_{5c}^{-c'}$ (Fig. 3.3). The calculated $LG_{-\delta}$ lattice parameters: $a = 5.60(2)$ Å, $b = 7.88(2)$ Å, $c = 5.56(1)$ Å, indicate slight expansion (as compared to LG) of the (2×1×2) supercell. This expansion is a result of the elongation of the bonds in the O-deficient/reduced $LG_{-\delta}$, viz., $r_{Ga_{5c}^{+c'}-O_{eq}^{-c'}} = 2.13$ Å and $r_{Ga_{5c}^{-c'}-O_{eq}^{-c'}} = 2.07$ Å.

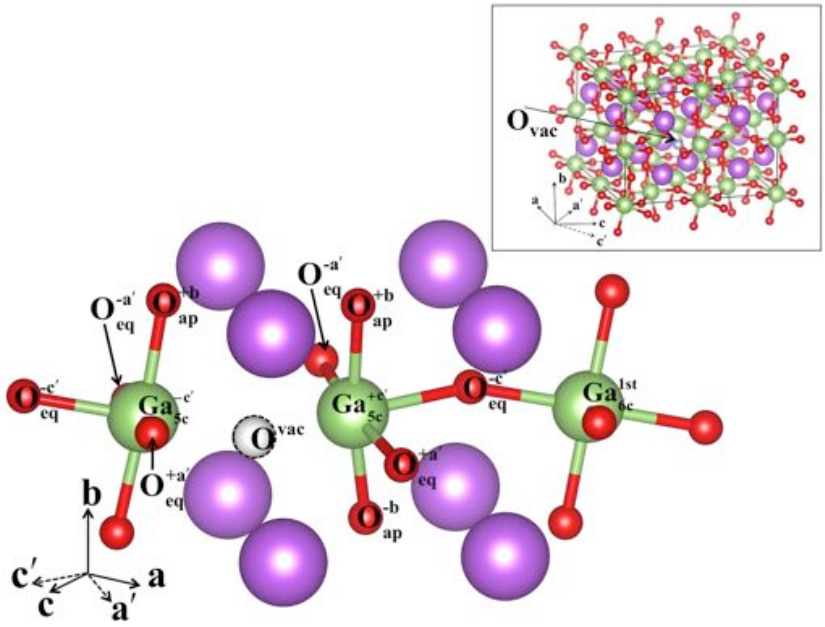


**Figure 3.3:** A magnified view of the most stable pyramidal structure [$GaO_5$] of the reduced $LaGaO_3$ ($LG_{-\delta}$). O vacancy ($O^{vac}$: white, dashed-outlined sphere. (Inset) The most stable position for $O^{vac}$ in the $(2 \times 1 \times 2)$ supercell, containing 79 atoms: 16 La (largest/light purple spheres), 16 Ga ($2^{nd}$ largest/green spheres), 47 O (smallest/red spheres). The corresponding coordinate axes ($a, b, c$ and $a', c'$) are also shown.

Furthermore, we observe that the structural distortion of the unsaturated [$GaO_5$] pyramid is most prominent in the immediate vicinity of $O^{vac}$. The other Ga-O bond lengths remain almost the same as in the stoichiometric LG ($\sim$ 2.02(3) Å). The presence of $O^{vac}$ not only elongates the $Ga_{5c}^{\pm c'}$-$O_{eq}^{-c'}$ bond lengths, but also tilts the [$GaO_5$] pyramids from the [$GaO_6$] octahedrons described above. The subtended angles $\measuredangle(O_{ap}^{-b} - Ga_{5c}^{\pm c'} - O_{ap}^{+b})$ decrease to 171.09° and 176.70°, respectively. Similary, the subtended angles $\measuredangle(O_{eq}^{-a'} - Ga_{5c}^{\pm c'} - O_{eq}^{+a'})$ decrease to 171.67° and 177.31°, respectively. On the other hand, no significant change was observed in the $\measuredangle(O - Ga - O)$ of the other [$GaO_6$] octahedrons. The tilting angle of [$GaO_5$] around $b$-axis does not show any significant change with the presence of $O^{vac}$.

### 3.3.3 Electronic Properties

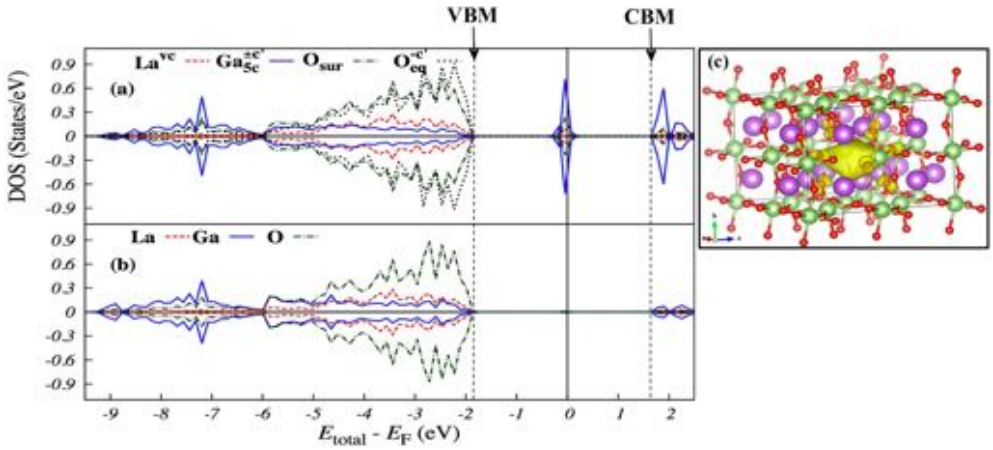


**Figure 3.4:** Calculated density of states (DOS) of O-deficient/reduced $LaGaO_3$ ($LG_{-\delta}$). (a) $[GaO_5]$ pyramids, which consist the surrounding $La^{vc}$ ions (red/dash), the $Ga_{5c}$ ions (blue/solid), the surrounding $O^{vc}$ ions ($O_{sur}$), including $O_{eq}^{\pm a'}$ and $O_{ap}^{\pm b}$, and the $O_{vc}$-opposite O ions ($O_{eq}^{-c'}$) metioned in Fig. 3.3. (b) Other $[GaO_6]$ octahedra, which include La, Ga and O ions. Energies given in [eV] with respect to the Fermi level ($E_F$). Figure 4(c) shows partial charge distribution of the defect state near the Fermi level of $LG_{-\delta}$, where the isosurface value is 0.003 $e/Å^3$. The corresponding VBM and CBM are also indicated.

Upon creation of an $O^{vac}$ to the pure LG, the resulting $LG_{-\delta}$ is still non-magnetic and insulating (cf., Fig. 3.4). The resulting two excess electrons in $LG_{-\delta}$ redistribute locally around the neighboring 5-fold coordinated Ga ions ($Ga_{5c}^{\pm c'}$, cf., Fig. 3.4(c)), and appear as defect states located between VBM and CBM, at or near $E_F$ (cf., Figs. 3.2 and 3.4). The defect states are located ca. 1.80 eV below CBM. The introduction of $O^{vac}$ strengthens the bonds in the $[GaO_6]$ octahedrons of $LG_{-\delta}$ as compared to the $[GaO_5]$ pyramids (cf., $[-9.2$ eV, $-6$ eV] in Fig. 3.4(b)). Again, as mentioned in Sec. 3.3.3, this will become important when we discuss about the O-migration (cf., Sec. 3.4).

## 3.4 Oxygen Migration (O-vacancy migration)

O-migration (or $O^{vac}$ migration in the opposite direction) takes place via occupation of the $O^{vac}$ site by the nearest O ion. In Fig. 3.5(a)) we show the four possible O-migration paths, viz.,

- path I: (shortest path) between two neighboring non-vertex sharing $[GaO_6]$ octahedra;
- path II: from $O_{ap}$ site to $O_{eq}$ sites of vertex-sharing $[GaO_6]$ octahedra; and
- paths III & IV: between the $O_{eq}$ sites of vertex-sharing $[GaO_6]$ octahedra.

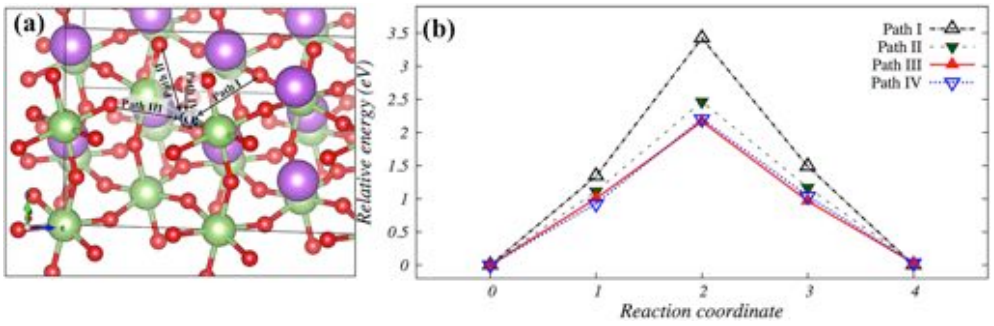


**Figure 3.5:** (a) O-migration paths from the most stable $O^{vac}$ configuration in an O-deficient/reduced $LaGaO_3$ ($LG_{-\delta}$). Path I corresponds to the shortest path between two non-vertex sharing [$GaO_6$] octahedra. Path II corresponds to the path between $O_{eq}$ sites in a a vertex-sharing [$GaO_6$] octahedra. There are two paths between the $O_{eq}$ sites, viz., paths III and IV, as shown. (b) Calculated energies corresponding to certain points along the paths indicated. Energies given in [eV] with respect to the initial position configuration.

As the results showed in Fig. 3.5(b), O-migration between the $O_{eq}$ sites gives the most favorable path (i.e., path III, $\sim$ 2.17 eV). This indicates that O-migration ($O^{vac}$-migration) occurs along vertex-sharing [$GaO_6$] octahedra. This result agrees with earlier experimental studies on, e.g., pure and doped LG. [83]

As shown in Fig. 3.6, O-migration ($O^{vac}$) along path III, between the $O_{eq}$ sites, follows an arc, starting from a $Ga_{6c}(Ga_{5c})$ in one [$GaO_6$] octahedron to the $Ga_{5c}(Ga_{6c})$ in the next neighboring vertex-sharing [$GaO_6$] octahedron. In the process of migration, $Ga_{56}$ ($Ga_{65}$) corresponds to the initially $Ga_{5c}(Ga_{6c})$ that, after O-migration ($O^{vac}$-migration), becomes, $Ga_{6c}(Ga_{5c})$. $Ga^{s}_{5c}$ corresponds to the $Ga_{5c}$ that remained 5-fold coordinated after O-migration ($O^{vac}$-migration). $La^{m}_{1}$ and $La^{m}_{2}$ refer to the neighboring two La ions the mobile O ($O_m$) has to pass during migration. In Table 3.2, there is only a slight change in the charge distributed around $O_m$. The other surrounding La and O ions do not play a significant role (in the charge transfer) during O-migration. In Fig. 3.7, we can see more clearly how the excess charges are redistributed during O($O^{vac}$)- migration.

Upon the introduction an O-vacancy, the excess electrons redistributed around the neighboring Ga, viz., those that would later become $Ga_{65}$ and $Ga_{56}$. Thus, in the initial configuration, as a result of the increased $e$-charge of $Ga_{65}$, the Coulomb repulsion with $O_m$ increases. Subsequently, $O_m$ breaks away from $Ga_{65}$, and bonds more strongly with $Ga^{s}_{5c}$. As the $O_m$ migrates, the bond length $r_{Ga^{s}_{5c}-O_m}$ decreases from 2.04 Å to 1.90 Å. The decrease in bond length in turn results in an increased repulsion between $Ga^{s}_{5c}$ and $O_m$. Subsequently, $Ga^{s}_{5c}$ loses electrons while the $Ga_{56}$ ion gains more electrons. The excess electrons redistribute locally around $Ga_{56}$. This increases the Coulomb repulsion between $O_m$ and $Ga_{56}$ ions and hinders for the $O_m$ from bonding with $Ga_{56}$ ion. At the transition region, during $O^{vac}$

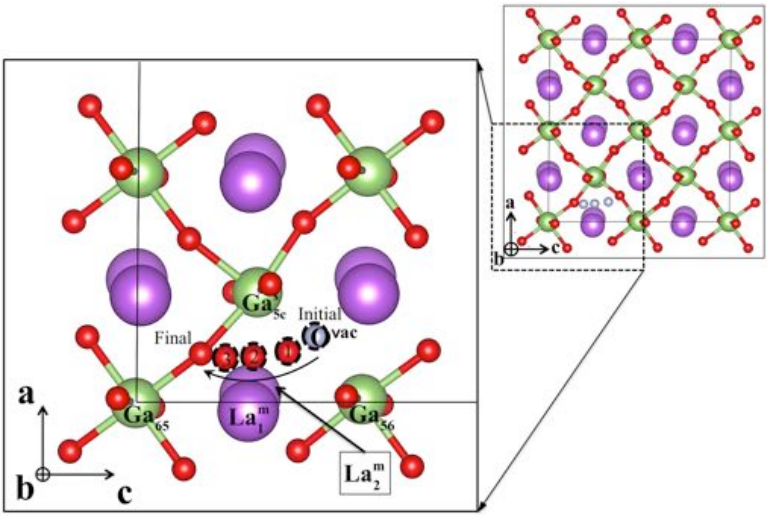


**Figure 3.6:** The most favourable O-vacancy ($O^{vac}$) migration path (path III in Fig. 3.5). The labels "Initial", "1", "2", "3", "Final" indicate the initial, location, intermediate locations, and final locations of ($O^{vac}$). $O_m$ traces the same path in the opposite direction.

**Table 3.2:** Bader charge analysis for each images along the O-migration path. Positions of $Ga_{5c}$, $Ga_{56}$, $Ga_{65}$, $La_1^m$ and $La_2^m$ were shown in Fig. 3.6. $O_m$ represents for the mobile O ions, which is in the inverse direction with the $O^{vac}$. $O_{sur}$ ions are the other O ions surrounding the shared [$GaO_5$] pyramid. Positive (negative) values refers to electron loss (gain) through bonding with other ions.

| | Bader charge | | | | |
|---|---|---|---|---|---|
| Atomic position | Initial state | Image 1 | Image 2 | Image 3 | Final state |
| $Ga_{5c}$ | 11.77 | 11.33 | 11.26 | 11.31 | 11.65 |
| $Ga_{56}$ | 11.61 | 12.00 | 11.56 | 11.19 | 11.15 |
| $Ga_{65}$ | 11.15 | 11.21 | 11.61 | 12.04 | 11.73 |
| $O_m$ | 7.31 | 7.29 | 7.28 | 7.31 | 7.31 |
| $La_1^m$ | 8.97 | 8.94 | 8.94 | 8.96 | 8.98 |
| $La_2^m$ | 8.99 | 8.97 | 8.93 | 8.92 | 8.92 |
| $O_{sur}$ | 7.31 | 7.31 | 7.31 | 7.32 | 7.31 |
| | Effective charge | | | | |
| Atomic position | Initial state | Image 1 | Image 2 | Image 3 | Final state |
| $Ga_{5c}$ | 1.23 | 1.67 | 1.74 | 1.69 | 1.35 |
| $Ga_{56}$ | 1.39 | 1.00 | 1.44 | 1.81 | 1.85 |
| $Ga_{65}$ | 1.85 | 1.79 | 1.39 | 0.96 | 1.27 |
| $O_m$ | −1.31 | −1.29 | −1.28 | −1.31 | −1.31 |
| $La_1^m$ | 2.03 | 2.06 | 2.06 | 2.04 | 2.02 |
| $La_2^m$ | 2.01 | 2.03 | 2.07 | 2.08 | 2.08 |
| $O_{sur}$ | −1.31 | −1.31 | −1.31 | −1.32 | −1.31 |

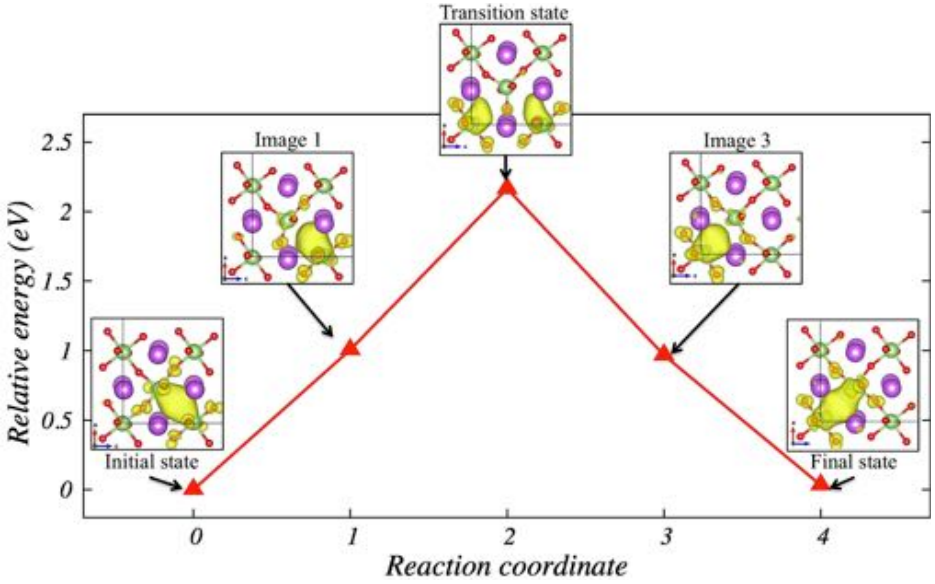


**Figure 3.7:** Calculated energies and partial charge distributions of the defect states correspond to each states along the O-vacancy ($O^{vac}$) migration path (path III in Fig. 3.5 and also cf., Fig. 3.6). Isosurfaces are given in intervals of 0.003 $e/\text{Å}^3$.

migration, $O_m$ has to pass through a triangular region/opening created by $Ga^s_{5c}$ ion and two La ions (i.e., $Ga^s_{5c}$-$La^m_1$-$La^m_2$). Following the movement of $O_m$, $Ga^s_{5c}$, $La^m_1$, and $La^m_2$ lose a few electrons and become more positive (in terms of effective charge). The shorter the bond lengths between $O_m$ ion with $Ga^s_{5c}$, $La^m_1$ and $La^m_2$ ions are, the stronger the Coulomb attraction between these ions become. From the initial to the transition state, $r_{O_m-La^m_1}$ decreases from 2.44 Å to 2.32 Å; and $r_{O_m-La^m_2}$ decreases from 2.81 Å to 2.34 Å. At the transition state, $Ga_{56}$ loses electrons and $Ga_{65}$ gains electrons. However, most of the excess electrons are located on the $Ga_{56}$ and $Ga_{65}$ as seen in Fig. 3.7. This maintains the Coulomb repulsion between $O_m$ and $Ga_{56}$. The attractive nature of the interaction between $O_m$-$Ga^s_{5c}$, $O_m$-$La^m_1$, and $O_m$-$La^m_2$, and the repulsive interaction between $O_m$-$Ga_{56}$ seem to indicate the reason for the difficulty of $O_m$ migration in LG and require a large activation energy (energy barrier for migration). The redistribution of excess electrons on $Ga_{65}$ promotes $O_m$ migration through the transition state.

After passing through the $Ga^s_{5c}$-$La^m_1$-$La^m_2$ triangular region, $O_m$ gradually bonds with $Ga_{56}$, resulting in a charge reduction of $Ga_{56}$. Subsequently, $Ga^s_{5c}$, $La^m_1$ and $La^m_2$ regain the excess electrons. $Ga_{65}$ gains the most excess electrons, and the most increased Coulomb repulsion with the $O_m$. At the final state, the roles of $Ga_{56}$ and $Ga_{65}$ are reversed. The distribution of excess electrons show again the accumulation of charge in the $Ga^s_{5c}$-$O^{vac}$-$Ga_{65}$ bonding orbital.

The other migration paths along the equatorial edge of the [$GaO_6$] octahedron (path IV) and the migration path between the apical O site and the equatorial O site (path II) share the same mechanism. From these results, we see that Coulomb interaction plays an important role in O-migration in pure LG.

## 3.5 Summary

As ionic conductors, O-vacancies are necessary in the LG-based materials. The study of the pristine/stoichiometric LG-based materials forms a basics for understanding the role of O-vacancy in the O-defect/reduced $LG_{-\delta}$. We can see that it is difficult to form O-vacancy in LG, as indicated by the calculated large O-vacancy formation energy. We also found that the equatorial O-positions of [$GaO_6$] octahedron are more favorable than the apical O-positions for introducing O-vacancy. This preference is due to the difference in the nature of the bonds with the surrounding cations, especially the weak covalent bonding with La. The effect of O-vacancy on the structural characteristics is primarily observed around the vicinity of the vacancy site. The introduction of O-vacancy leads to excess electrons in the O-deficient/reduced LG ($LG_{-\delta}$). This induces the accumulation of charge in the $Ga_{5c}$-$O^{vac}$-$Ga_{5c}$ bonding, and an associated localized defect state appears in the corresponding electronic structure. The appearance of O-vacancy allows the O ion to migrate in $LG_{-\delta}$ through O hopping to the O-vacancy site. Calculated potential curves for O-migration shows that the preferable migration paths are along the equatorial edges of the [$GaO_6$] octahedron. Coulomb interaction between the mobile O with other ions play an important role in the O migration mechanism and is the main reason for the presence of high activation energy hindering O-migration. In order to apply this material in a variety of applications, e.g., in solid-oxide fuel cells, we need to reduce not only the O-vacancy formation energy, but also the Coulomb interaction of the mobile O with the surrounding ions.

# Chapter 4

# O-vacancies in Doped $LaGaO_3$ Based Materials

## 4.1 Doped $LaGaO_3$-Based Materials

The previous chapter clarified that excess electrons from the creation of O-vacancy increased the Coulomb interaction between mobile O ions and surrounding cation ions and hindered the O-vacancy migration in pristine/stoichiometric LG. The concentration of O-vacancies is also low in pure LG due to the high O-vacancy formation energy, which was confirmed by both calculation and experimental studies [89, 90]. This raises a question: how do we avoid the excess electrons in LG materials. Doping on a cation site could be one solution to reduce the O-vacancy formation energy and the occurrence of excess electrons.

Following the initial discovery by Ishihara et al. [91, 92], numerous experimental studies have been carried out on the $LaGaO_3$-based materials, which include reports covering oxygen ion conductivity [76, 87, 93–95], structural properties [96–99], electrolyte performance within SOFCs [97, 100, 101] and the effect of transition-metal doping [102, 103]. Among the possible dopants, the incorporation of cation dopants such as Sr and Mg at La and Ga sites, respectively, to form $(La_{1-x}Sr_x)Ga_{1-y}Mg_yO_{3-\delta}$ (i.e., LSGM), gives rise to the highly mobile oxygen vacancies that are responsible for the observed ionic conductivity [76, 91, 100]. It is revealed that $Sr^{2+}$, which has ionic size almost similar to $La^{3+}$, shows a strong effect on LG in term of increasing O-vacancy concentration and ionic conductivity. However, the stability of Sr into La sites is not good. The secondary phases, $SrGaO_3$ and $La_4SrO_7$, created when the amount of Sr becomes higher than 10 mol%. The investigation of dopant at Ga sites has also been carried out. It is found that doping $Mg^{2+}$ into $Ga^{3+}$ sites is also effective at increasing the O-vacancy concentration [104]. Since it was found that doping with the Sr and Mg dopants have the most influence on LG-based materials [92] , we focused on gaining a deeper understanding of the effect of these dopant to the

O-deficient/reduced LG.

## 4.2 Sr- and Mg-Doped $LaGaO_3$: (LSGM)

### 4.2.1 Geometric Structure

In Fig. 4.1, we show the optimized structure of the doped LSGM. The calculated lattice parameters: $a = 5.60(3)$ Å, $b = 7.87(4)$ Å, and $c = 5.58(2)$ Å, agree with experimental observations, with errors within 2%. [91]. This expansion in volume of the unit cell is expected because of the difference in ionic radius between the hosts (La, Ga) and the dopants (Sr, Mg). We see that the orthorhombic structure with *Pnma* symmetry persists. Two dopants are found to be stable at position far from each other (cf., Fig. 4.1a). The Sr and Mg dopants only affect the O ions and [$GaO_6$] octahedra nearest to the dopants. Other [$GaO_6$] octahedra are similar to LG-based materials with $r_{\mathrm{Ga-O}} \sim$ 2.01 Å, and $r_{\mathrm{La-O_{ap}/O_{eq}}} = 2.41/2.45$ *Å* for the apical O ($O_{ap}$) and equatorial O ($O_{eq}$) ions, respectively.

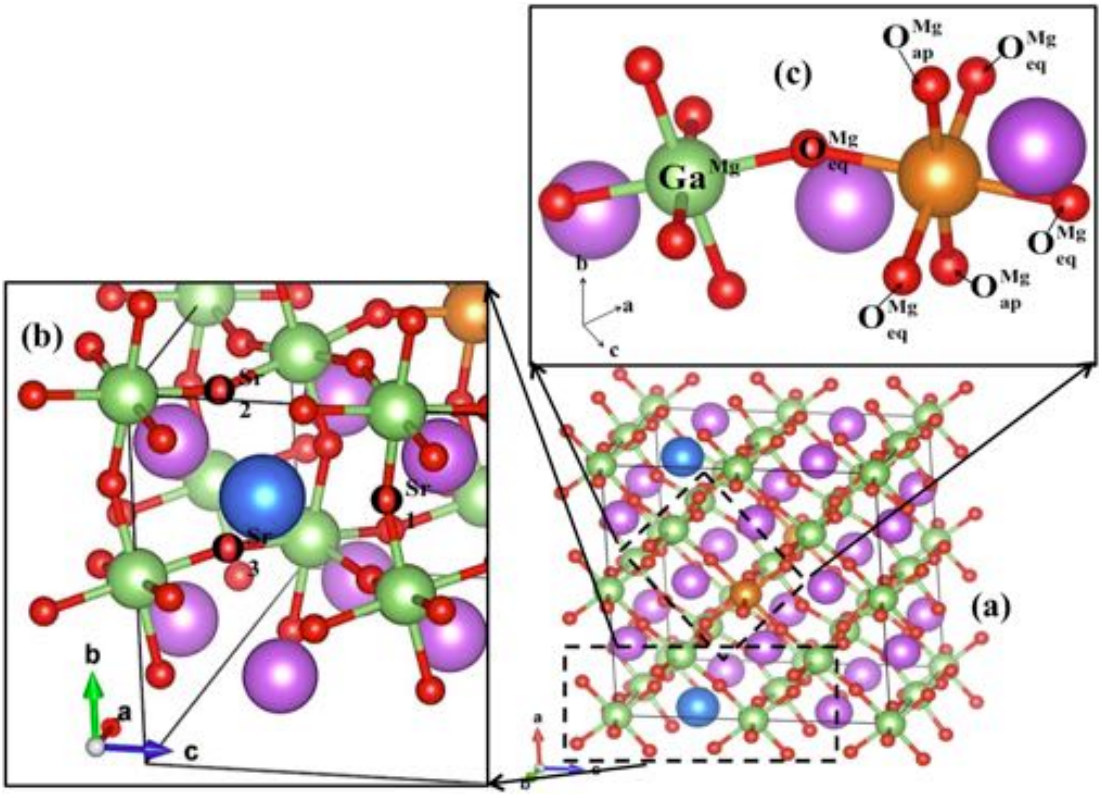


**Figure 4.1:** The optimized structure of the non-defect LSGM. (a) In the ($2 \times 1 \times 2$) supercell, a Sr ion and a Mg ion were substituted for the La ion and Ga ion, respectively. The supercell contains 80 atoms: 15 La (light purple spheres), 1 Sr (blue spheres), 15 Ga (green spheres), 1 Mg (orange spheres), 48 O (red spheres). (b) A magnified view of the vicinity of Sr ion with the three nearest O ions (viz. $O_1^{Sr}$, $O_2^{Sr}$ and $O_3^{Sr}$). (c) A magnified view of the vicinity of Mg ion. $O^{Mg}$ and $Ga^{Mg}$ refer to the O ion of [$MgO_6$] octahedron and the first nearest Ga ions.

The distortion of the structure only appears in the vicinity of the dopants. The Mg dopant affects most the bond length of the nearest O ions, i.e., $O^{Mg}$, with the nearest Ga ions, i.e., $Ga^{Mg}$ The $[MgO_6]$ octahedron maintains the tilting of the original $[GaO_6]$ octahedra with the longer bond lengths $r_{Mg-O^{Mg}} = 2.08(1)$ Å. These shorten the bond lengths of $O^{Mg}$ and $Ga^{Mg}$: $r_{Ga^{Mg}-O^{Mg}} \sim 1.97(1)$ Å. In the $[GaO_6]$ octahedra nearest to the Mg dopant, bond lengths $r_{Ga^{Mg}-O} \sim 2.03$ Å, same as the other $[GaO_6]$ octahedra.

Meanwhile, Sr dopant affects mostly on the subtended angles $\measuredangle(Ga-O-Ga)$ in the vicinity of Sr ion, i.e., three closest O ions ($O^{Sr}$, viz. $O_1^{Sr}$, $O_2^{Sr}$, $O_3^{Sr}$). The subtended angles between these O ions and two bonding Ga ions open: $\measuredangle(Ga-O_1^{Sr}-Ga) = 158.72°$, and $\measuredangle(Ga-O_2^{Sr}-Ga) = \measuredangle(Ga-O_3^{Sr}-Ga) = 159.90°$, which are 154.85° and 155.80°, respectively, in pristine LG based materials. Bond lengths $r_{Ga-O_1^{Sr}/O_2^{Sr}/O_3^{Sr}}$ slightly change to $\sim 2.00$ Å. Besides, bond lengths $r_{Sr-O_1^{Sr}} = 2.49$ Å and $r_{Sr-O_2^{Sr}} = r_{Sr-O_2^{Sr}} = 2.52$ Å, for the apical $O_1^{Sr}$ and the equatorial $O_2^{Sr}$, $O_3^{Sr}$, respectively.

### 4.2.2 Electronic Properties

Upon substituting divalent Sr and Mg ions to trivalent La and Ga sites, the LSGM become metallic (cf., Fig. 4.2a-b). This is not good for an ionic conducting material, which is required to exhibit low electronic conductivity. The introduction of dopants makes electrons less localised in LSGM. The corresponding calculated local density of states (LDOS) shows the broadening of electronic bands of LSGM (refer to pristine LG based materials).

The introduction of dopants reduces slightly the covalent bond of La-O/Ga-O, seen as reducing the magnitude of the hybridizations between O ions and the La/Ga cation ions (Fig. 4.2a). Sr and $O^{Sr}$ ions share weak covalent bonds seen as the small hybridizations of Sr-$O^{Sr}$ (cf. [−2 eV, VBM] in Fig. 4.2b). This causes the enhancement of the distribution of $O^{Sr}$ ions near Fermi level (cf., [−2 eV, 0.2 eV] in Fig. 4.2b). The corresponding LDOS of Mg only shows small and narrow hybridization with the O ions belong the $[MgO_6]$ octahedron (cf., [−4 eV,−3.7 eV], Fig. 4.2c).

Sr and Mg are reducing agents, so it is easy for these atoms to lose two outermost electrons, and become cation ions. In co-dopes LSGM, Sr and Mg ions also present as reducing agents when losing most of two outermost electrons(cf. Table 4.1). It makes the bonds of Sr-O and Mg-O more ionic than the bonds of La-O and Ga-O. Bader charge analysis shows that La and Ga ions remain the same charges as in LG-based material (cf. Table 3.2). After the charge transfer, Sr

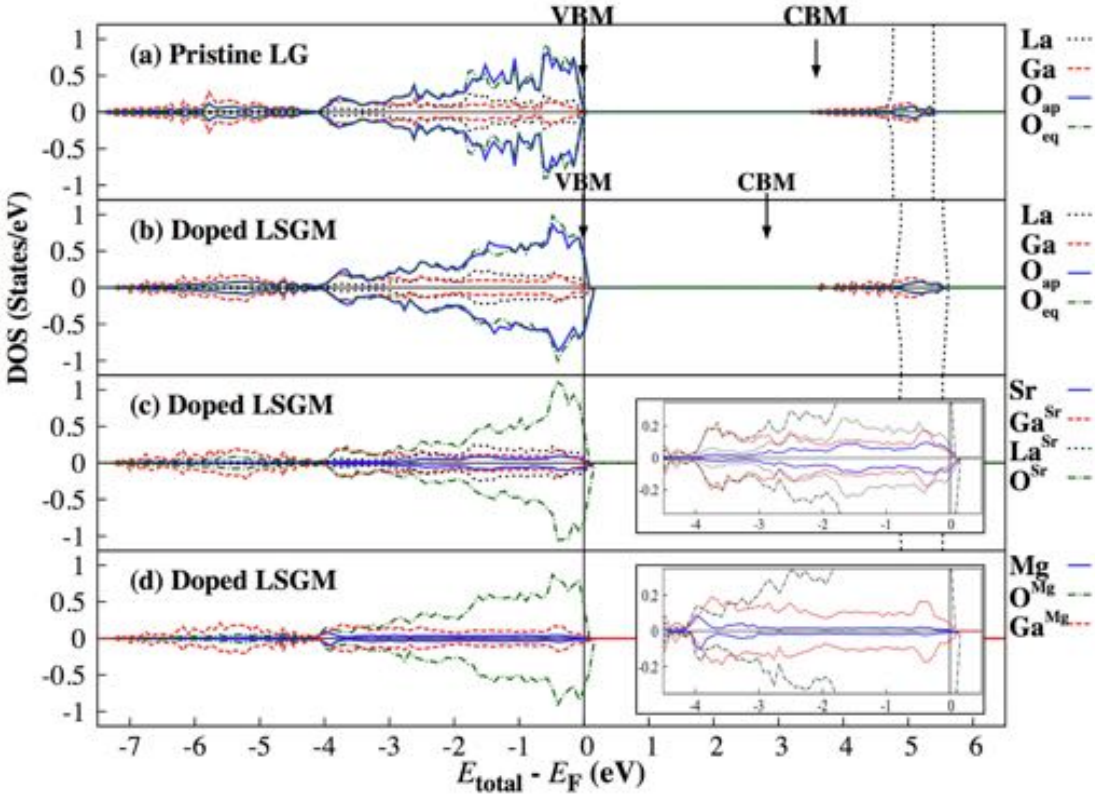


**Figure 4.2:** Calculated local density of states (LDOS) of the doped LSGM. (a) DOS for whole ($2\times1\times2$) super-cell with DOS contributions from lanthanum (La), gallium (Ga), apical oxygen ($O_{ap}$), and equatorial oxygen ($O_{eq}$), respectively. (b) LDOS for the vicinity of Sr ion, which consist the surrounding $La^{Mg}$ ions, Sr ion and the $O^{Sr}$ ions (i.e. $O_1^{Sr}$, $O_2^{Sr}$ and $O_3^{Sr}$). (Inset: The magnified view of LDOS in the energy range [-4.5 eV, 0.5 eV].) (c) DOS for the vicinity of Mg ion, which consist Mg ion, the O ions of [$MgO_6$] ($O^{Mg}$) and the nearest Ga ions ($Ga^{Mg}$). (cf., Fig. 4.1) (Inset: The magnified view of LDOS in the energy range [-4.5 eV, 0.5 eV].) Energies are given in [eV] with respect to the Fermi level ($E_F$). The corresponding valence band maximum (VBM) and conduction band maximum (CBM) are also indicated.

**Table 4.1:** Bader charge analysis of the non-defected LSGM. Effective charge of each atoms is the deduction of the corresponding Bader charge from the original valence electrons of the atoms (10 for La, 13 for Ga, 10 for Sr, 8 for Mg and 6 for O). Positive/negative values refers to loss/gain electrons. $O^{Sr}$ and $O^{Mg}$ refers for O ions in the vicinity of the Sr and Mg, respectively. "Other O" refers to the other O ions outside of the vicinity of Sr and Mg ions. (cf., Fig. 4.1)

| Cation site | La | Sr | Ga | Mg | $O^{Sr}$ | $O^{Mg}$ | other O |
|---|---|---|---|---|---|---|---|
| Bader charge (e) | 8.91 | 8.41 | 11.13 | 6.25 | 7.30 | 7.35 | 7.30 |
| Effective charge (e) | 2.09 | 1.59 | 1.87 | 1.75 | -1.30 | -1.35 | -1.30 |

ion has the ionic bonds with the nearest O ions, i.e., $O^{Sr}$. However, the difference in effective charge with the surrounding O ion suggests that the ionic bonds of Sr-O seem to be weak as compare to the other ionic interactions between O ions and cation ions such as La, Ga and Mg. In contrary, Mg losses more electrons for the surrounding O (O ions belong the [$MgO_6$] octahedron, i.e., $O^{Mg}$) than Sr (cf. Table 4.1); and the resulting charge of $O^{Mg}$ ions increase. This results make the bonds of Mg-O more ionic. The ionic bond of Sr-$O^{Sr}$ and Mg-$O^{Mg}$ becomes important for the discussion of the O-vacancy formation (cf., Sec. 4.3).

## 4.3 O-deficient/reduced (LaSr)(GaMg)$O_{3-\delta}$

An O-vacancy was introduced into the $t5(2 \times 1 \times 2)$ supercell of LSGM , resulting in the O-deficient/reduced $(La_{1-x}Sr_x)(Ga_{1-y}Mg_y)O_{3-\delta}$ ($x = y = 0.0625$; $\delta = 0.0625$) ($LSGM_{-\delta}$). All possible positions in supercell for O-vacancy are considered. Following Eq.3.1, to evaluate the feasibility of realizing such O-vacancies, we calculate the corresponding O-vacancy formation energy ($E_O^{vacancy}$) in terms of the difference in the corresponding energies for a non-deficient LSGM ($E^{stoichiometric} = E_{LSGM}$) with that of a reduced (O-deficient) LG ($E^{reduced} = E_{LSGM_{-\delta}}$) and a free O in the gas phase ($\frac{1}{2}E_O^{gas}$, cf., Refs. [55, 56]), i.e.,

$$\begin{aligned} E_O^{vacancy} &= E^{reduced} - E^{stoichiometric} + \frac{1}{2}E_{O_2}^{gas} \\ &= E_{LSGM_{-\delta}} - E_{LSGM} + \frac{1}{2}E_{O_2}^{gas} \end{aligned} \tag{4.1}$$

**Table 4.2:** Calculated O-vacancy formation energy ($E_O^{vacancy}$, Eq. 4.1) in LSGM for the corresponding $1^{st}$, $2^{nd}$ and $3^{rd}$ nearest to the Mg and Sr dopants (cf., Fig. 4.1).

| Vacancy site | refer to Mg ions | | | refer of Sr ion | | |
|---|---|---|---|---|---|---|
| | $1^{st}$ nearest | $2^{nd}$ nearest | $3^{rd}$ nearest | $O_1^{Sr}$ | $O_2^{Sr}$ | $O_3^{Sr}$ |
| $E_O^{vacancy}$ [eV] | 0.47 | 0.48 | 0.51 | 0.18 | 0.22 | 0.25 |

In Table 4.2, we show the computed $E_O^{vacancy}$ for the O position $1^{st}$, $2^{nd}$ and $3^{rd}$ nearest to the dopants of Mg and Sr (cf., Fig. 4.1). The introduction of Sr and Mg considerably reduces the O-vacancy formation energy, which has the value of 5.65 eV in LG-based materials [89]. The most stable O-vacancy position is found to be at the nearest O ions from the Sr ion (viz., $E_O^{vacancy} = 0.18$ eV). The highest O-vacancy formation energy is found at the O ions nearest Mg ion (viz., $E_O^{vacancy} = 0.51$ eV). It means that O-vacancy was created easier near Sr ion than

Mg ion. It can be expected from the nature of the bonds between the dopants, i.e, Sr and Mg, and the corresponding O nearest to each dopant, i.e., $O^{Sr}$ and $O^{Mg}$, respectively. This result is in good agreement with the observation from experiments, which reported that the concentration of O-vacancies increases with the amount of Sr [76].

### 4.3.1 Geometric Structure

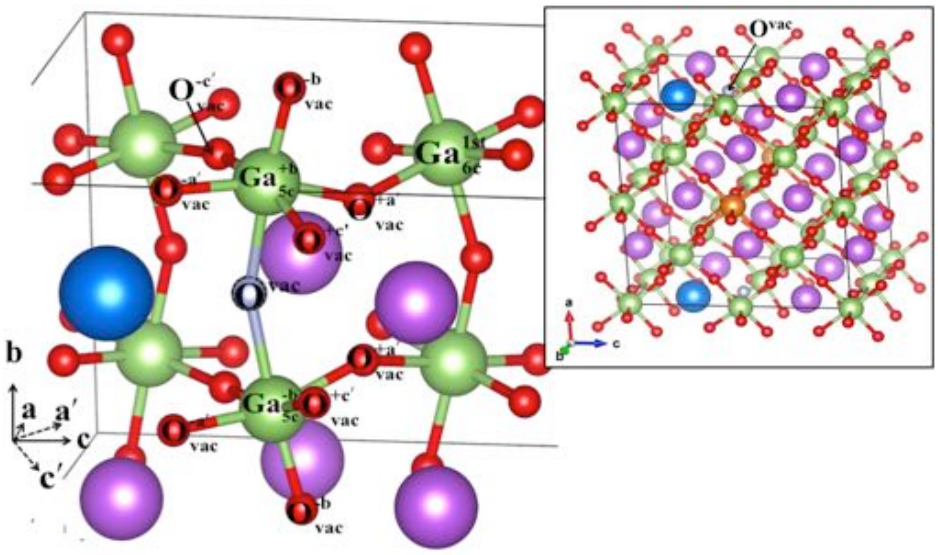


**Figure 4.3:** A magnified view of the most stable pyramidal structure [$GaO_5$] of the O-deficient/reduced LSGM$_{-\delta}$. One of the O ions along $b$-axis is replaced by an O vacancy ($O^{vac}$, white, dashed-outlined sphere), resulting in two 5-fold coordinated Ga ions ($Ga_{5c}$, viz., $Ga_{5c}^{\pm b}$). The $(2 \times 1 \times 2)$ supercell contains 79 atoms: 15 La ($2^{nd}$ largest/light purple spheres), 1 Sr (largest/blue sphere), 15 Ga ($4^{th}$ largest/green spheres), 1 Mg ($3^{rd}$ largest/orange sphere), 47 O (smallest/red spheres). (Inset) The most stable position for $O^{vac}$ in the $(2 \times 1 \times 2)$ supercell. The corresponding coordinate axes ($a, b, c$ and $a', c'$) are also shown.

The introduction of O-vacancy ($O^{vac}$) in LSGM creates two unsaturated [$GaO_5$] pyramids near the vacancy site with two 5-fold coordinated Ga ions, viz., $Ga_{5c}^{\pm b}$ (Fig. 4.3). The calculated LSGM$_{-\delta}$ lattice parameters: $a = 5.60(2)$ Å, $b = 7.88(2)$ Å, $c = 5.56(1)$ Å, does not indicate the expansion (as compared to LSGM) of the $(2 \times 1 \times 2)$ supercell. In contrast to the expansion of the pristine/stoichiometric LG, the introduction of $O^{vac}$ does not shows the considerable change of lattice parameters, even show the slight compression in $c$-axis, which is a result of reducing the bonds in [$GaO_5$] pyramid, viz., $r_{Ga_{5c}^{+b}-O_{vac}^{+b}}$ and $r_{Ga_{5c}^{-b}-O_{vac}^{-b}}$ decrease $\sim 7\%$ while $r_{Ga_{5c}^{+b}-O_{vac}^{\pm a'}}$ and $r_{Ga_{5c}^{+b}-O_{vac}^{\pm c'}}$ decrease $2 \sim 3\%$. The effect of $O^{vac}$ on bending [$GaO_5$] pyramids in LSGM$_{\delta}$ is similar to the effect in the O-deficient/reduced LG$_{\delta}$. The subtended angles $\measuredangle(O_{vac}^{-a'} - Ga_{5c}^{\pm b} - O_{vac}^{+a'})$

decrease to 164.24° and 164.29°, respectively. Similarly, the subtended angles $\measuredangle(\mathrm{O}_{\mathrm{vac}}^{-c'} - \mathrm{Ga}_{5c}^{\pm b} - \mathrm{O}_{\mathrm{vac}}^{+c'})$ decrease to 163.83° and 164.13°, respectively. The structural distortion can observed mostly in the immediate vicinity of $\mathrm{O}^{\mathrm{vac}}$. The distance between $\mathrm{Ga}_{5c}^{\pm b}$ and the first $\mathrm{Ga}_{6c}$ ($\mathrm{Ga}_{6c}^{1st}$) just change in order of 1% from the corresponding lengths in LSGM. It makes the elongation of the bond of the $\mathrm{O}_{\mathrm{vac}}^{\pm a'/c'}$ ions of [$\mathrm{GaO}_5$] pyramids and the nearest $\mathrm{Ga}_{6c}$, i.e., $\mathrm{Ga}_{6c}^{1st}$ ions ($\sim 5\%$).

### 4.3.2 Electronic Properties

**Table 4.3:** Bader charge analysis of the the O-deficient/reduced LSGM$_{-\delta}$. Effective charge of each atoms is the deduction of the corresponding Bader charge from the original valence electrons of the atoms (10 for La, 13 for Ga, 10 for Sr, 8 for Mg and 6 for O). Positive/negative values refers to loss/gain electrons. $\mathrm{Ga}_{5c}^{\pm b}$ was showed in Fig. 4.3. $\mathrm{Ga}_{6c}$ and $\mathrm{O}_{\mathrm{vac}}^{\mathrm{sur}}$ refer to the 6-fold coordinated Ga ions in supercell and the surrounding O ion of [$\mathrm{GaO}_5$] pyramid (incl. $\mathrm{O}_{\mathrm{vac}}^{\pm a'/c'}$, respectively.

| Cation site | $\mathrm{Ga}_{5c}^{\pm b}$ | $\mathrm{Ga}_{6c}$ | $\mathrm{O}_{\mathrm{vac}}^{\mathrm{sur}}$ | Mg | $\mathrm{O}^{\mathrm{Sr}}$ | $\mathrm{O}^{\mathrm{Mg}}$ | other O |
|---|---|---|---|---|---|---|---|
| Bader charge (e) | 11.25 | 11.15 | 7.32 | 6.25 | 7.33 | 7.37 | 7.31 |
| Effective charge (e) | 1.75 | 1.85 | -1.32 | 1.75 | -1.33 | -1.37 | -1.31 |

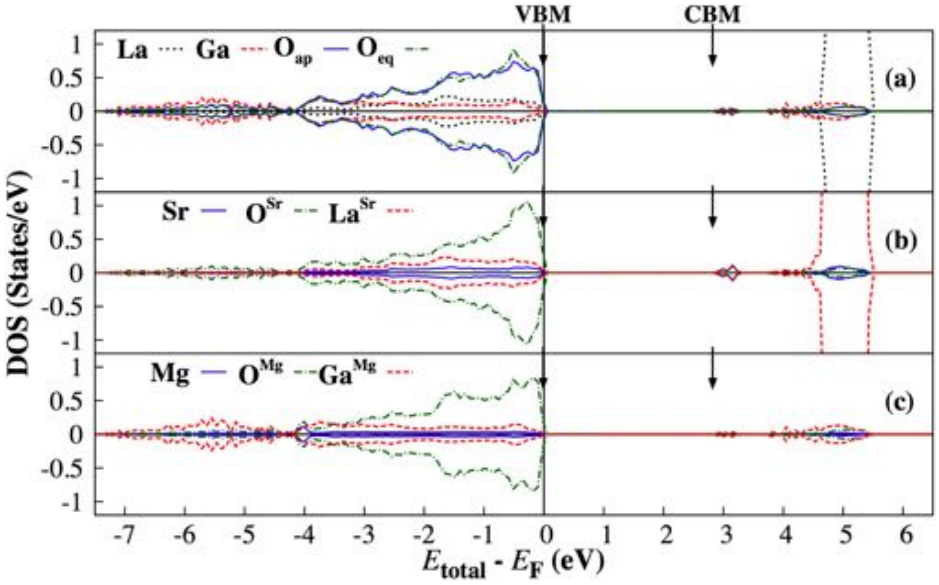


**Figure 4.4:** Calculated LDOS of LSGM and O-deficient/reduced LSGM$_{-\delta}$. (a) DOS for whole ($2 \times 1 \times 2$) super-cell: (b) LDOS for the vicinity of Sr ion, which consist the surrounding $\mathrm{La}^{\mathrm{Mg}}$ ions, Sr ion and the $\mathrm{O}^{\mathrm{Sr}}$ ions (incl. $\mathrm{O}_1^{\mathrm{Sr}}$, $\mathrm{O}_2^{\mathrm{Sr}}$ and $\mathrm{O}_3^{\mathrm{Sr}}$). (c) LDOS for the vicinity of Mg ion, which consist the O ions of [$\mathrm{MgO}_6$] ($\mathrm{O}^{\mathrm{Mg}}$), the nearest Ga ions ($\mathrm{Ga}^{\mathrm{Mg}}$) and Mg ions. Energies are given in [eV] with respect to the Fermi level ($E_{\mathrm{F}}$). The corresponding VBM and CBM are also indicated.

Table 4.3 shows that the $Ga_{5c}^{\pm b}$ ions gain most of electrons from the formation of $O^{vac}$. Beside, most of ions of $LSGM_{-\delta}$ also gain electrons with the creation of $O^{vac}$. It is the results of the presence of dopants, which make electrons less localised in co-doped LSGM.

Upon the presence of the dopants, the excess electrons, which were seen in LG-based materials, were suppressed in the O-deficient/reduced $LSGM_{-\delta}$; and, it leads the unoccupied defect states (ca. 3 eV in Fig. 4.4). The introduction of O-vacancy induced the insulating properties in $LSGM_{-\delta}$ materials, which is required for an ionic conductor. The gap between the valence band (VB) maximum (VBM) and the conduction band (CB) minimum (CBM) is 2.96 eV (cf., Fig. 4.4). No significant change is observed in the corresponding calculated LDOS for the vicinity of dopants. (cf., Fig. 4.4b-c)

### 4.3.3 Oxygen Migration (O-vacancy Migration)

Both of dopants are stable far away from each other, and the structure distortion of $[GaO_6]$ octahedra is observed only in the vicinity of the dopants. It is possible to consider individually the effect of each dopants on the O-migration.

#### 4.3.3.1 Effect of Sr Ions

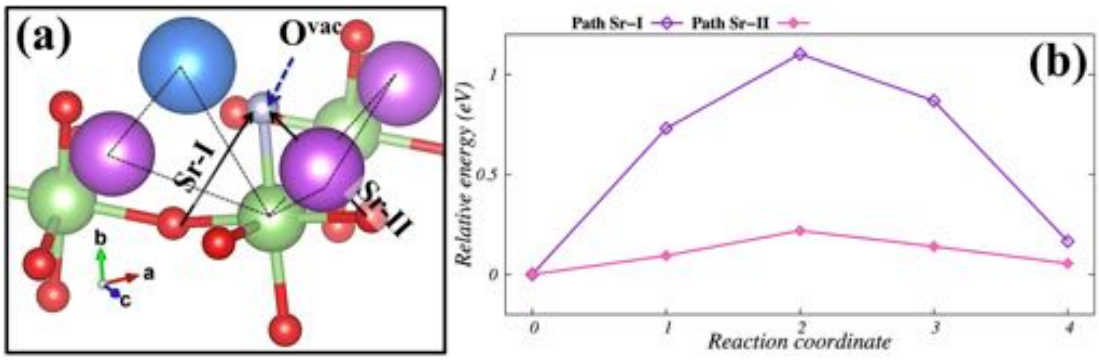


**Figure 4.5: (a)** O-migration paths from the most stable $O^{vac}$ configuration near Sr ion (i.e., $O_{1^{st}}^{Sr}$) in the O-deficient/reduced $LSGM_{-\delta}$. path Sr-I corresponds to the path near Sr ion, which has the transition state of mobile O passing through the triangle △Sr-Ga-La. path Sr-II corresponds to the path from the outside O site to the site nearest Sr ion (Mobile O passes the triangle △La-Ga-La in the transition state). **(b)** Calculated energies corresponding to certain points along the paths indicated in Fig. (a). The migration activation energy ($E_a$) corresponds to the energy of the transition state. Energies were given in [eV] with respect to the initial position configuration.

O-migration (or $O^{vac}$ migration in the opposite direction) takes place via occupation of the $O^{vac}$ site by the nearest O ion. In Fig. 4.5(a), we show the two

representative O-migration paths from the most stable configuration of $O^{vac}$ , viz.,

- path Sr-I: (near Sr ion, between two nearby O ions) Mobile O has to pass through the triangle △La-$Ga^{s}_{5c}$-Sr in the transition state. ($Ga^{s}_{5c}$ refers to the $Ga_{5c}$ that remained 5-fold coordinated after O-migration ($O^{vac}$-migration))

- path Sr-II: (far Sr ion, between the "outside" O ion to the O ion nearest to the Sr dopant) Mobile O has to pass through the triangle △La-$Ga^{s}_{5c}$-La in the transition state.

We can see in Fig. 4.5b: the path Sr-II (from outside O site to the nearest O site) give the more favourable path (i.e., $\sim 0.22eV$). This indicates that Sr ion does not support for the nearby O($O^{vac}$)-migration.

**Table 4.4:** Bond lengths of between mobile O and the surrounding atoms: the shared 5-fold coordinated Ga (i.e., $Ga^{s}_{5c}$), O ion of [$GaO_5$] pyramid nearest to mobile O, Sr/$La^{m}_{1}$ for the corresponding path *Sr-I*/*Sr-II*, respectively, and $La^{m}_{2}$ (cf., Fig. 4.5a).

| | | $r_{Ga^{s}_{5c}-O_m}$ [Å] | $r_{O_m-O_{1st}}$ [Å] | $r_{Sr/La^{m}_{1}-O_m}$ [Å] | $r_{La^{m}_{2}-O_m}$ [Å] |
|---|---|---|---|---|---|
| Path *Sr-I* | Initial | 2.04 | 2.73 | 2.80 | 3.38 |
| | TS | 1.81 | 2.59 | 2.33 | 2.45 |
| Path *Sr-II* | Initial | 1.97 | 2.75 | 2.42 | 2.61 |
| | TS | 1.83 | 2.68 | 2.31 | 2.38 |

The closer view of the transition states in the O($O^{vac}$)-migration process can give an explanation for this results. The transition state of path *Sr-I* shows the unstable configuration, as compare to the transition state of path *Sr-II*. Mobile O ($O_m$) in the transition state moves closer to Sr ion. The larger ionic radius of Sr elongates the bonds of $O_m$ with Sr-$O_m$ and $La^{m}_{2}$-$O_m$, and decreases the bond lengths of $O_m$ with $Ga^{s}_{5c}$, esp., with the nearest O of same [$GaO_5$] pyramid, i.e., $O^{1st}$ (cf., Table 4.4). This results in the stronger bond of $Ga^{s}_{5c}$-$O_m$ and the Coulomb repulsion between $O_m$ and the nearest O ion. It makes the transition state configuration of path *Sr-I* more unstable than the transition state configuration of path *Sr-II* , resulting higher activation energy.

#### 4.3.3.2 Effect of Mg Ions

In Fig. 4.6(a) we show the four possible O-migration paths (shortest path), viz.,

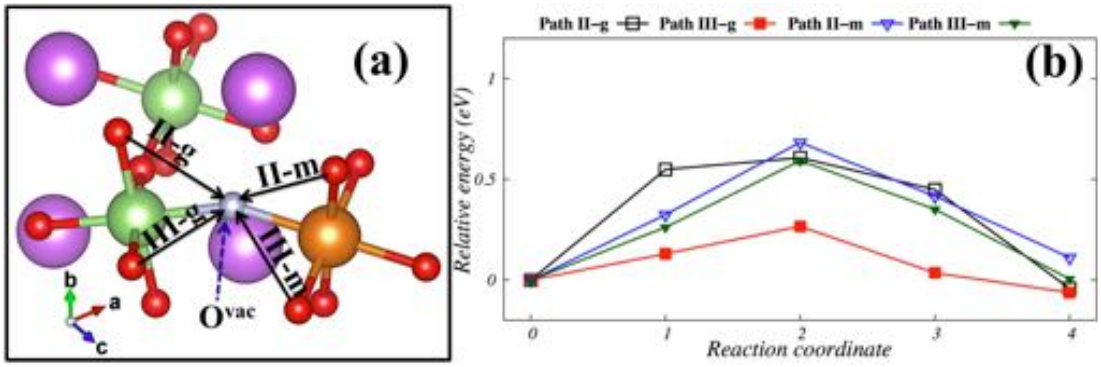


**Figure 4.6:** (a): O-migration paths from the most stable $O^{vac}$ configuration near Mg ion in the O-deficient/reduced $LSGM_{-\delta}$. path II-g and path II-m correspond to the path between the apical O site and equatorial O sites within the nearest $[GaO_6]$ and $[MgO_6]$ octahedra, respectively. path III-g and III-m correspond to the path between two equatorial O sites within the nearest $[GaO_6]$ and $[MgO_6]$ octahedra, respectively. (b): Calculated energies corresponding to certain points along the paths indicated in Fig.(a). The migration activation energy ($E_a$) corresponds to the energy of the transition state. Energies were given in [eV] with respect to the initial position configuration.

- path II-g: from $O_{ap}$ site to $O_{eq}$ sites within the $[GaO_6]$ octahedra nearest to Mg ions
- path III-g: between the $O_{eq}$ sites pf the $[GaO_6]$ octahedra nearest to Mg ions
- path II-m: from $O_{ap}$ site to $O_{eq}$ sites within the $[MgO_6]$ octahedra
- path III-m: between the $O_{eq}$ sites along the equatorial edge of the $[MgO_6]$ octahedra

We can see in Fig. 4.6b: for both of $[MgO_6]$ and the nearest $[GaO_6]$ octahedra, O-migration between the $O_{eq}$ sites gives the most favourable path (i.e., path III-g, $\sim$ 0.27 eV, and path III-m, $\sim$ 0.59 eV, for the nearest $[GaO_6]$ and $[MgO_6]$, respectively). The trending of $O(O^{vac})$-migration near the Mg dopant in the O-deficient/reduced $LSGM_{-\delta}$ is similar to the $O(O^{vac})$-migration in the O-deficient/reduced $LG_{-\delta}$. It is in agreement with the study by molecular dynamics [83,105]. It is notable that $O(O^{vac})$-migration between two equatorial sites within the nearest $[GaO_6]$ octahedron have a lowest activation energy among the paths near Mg ion. It results from the structural distortion of the nearest $[GaO_6]$ octahedron. This octahedron is under the effects of Mg dopant, which affects the bond length of Ga-O, and the effect of O-vacancy, which affects the tilting of $[GaO_5]$ pyramid. It elongates strongly the bonds between the equatorial O ion, which near the $O^{vac}$, and La ions (2.53 [Å] and 2.64 [Å]). This expansion weakens the bonds between the equatorial O ion and the surrounding La ion, and

produces the lower activation energy. In Fig. 4.6, the O($O^{vac}$)-migration seem to become less favourable within the [$MgO_6$] octahedron, for both of the paths from $O_{ap}$ site to $O_{eq}$ sites and the path between the $O_{eq}$ sites.

#### 4.3.3.3 Outside the Vicinity of Dopants

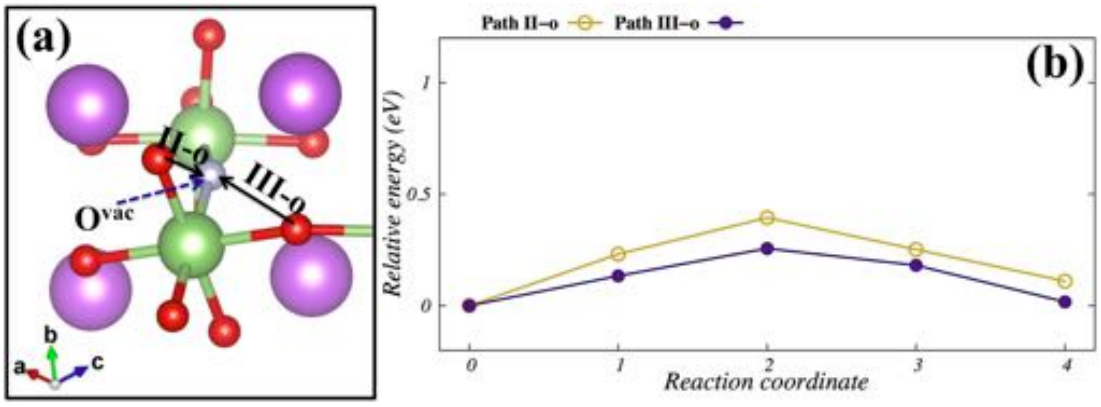


**Figure 4.7:** (a): O-migration paths from the most stable $O^{vac}$ configuration outside the vicinity of dopants in the O-deficient/reduced $LSGM_{-\delta}$. Path II-o corresponds to the path between the apical O site and equatorial O sites, and path III-o correspond to the path between two equatorial O sites within a [$GaO_6$] octahedron. (b): Calculated energies corresponding to certain points along the paths indicated in Fig.(a). The migration activation energy ($E_a$) corresponds to the energy of the transition state. Energies were given in [eV] with respect to the initial position configuration.

Outside the vicinity of Sr and Mg dopants, [$GaO_6$] octahedra are not under the effect of dopant, and maintain the geometric and electronics properties of the O-deficient/reduced $LG_{\delta}$. In Fig. 4.7(a) we show the two representative O-migration paths, viz.,

- path II-o: from $O_{ap}$ site to $O_{eq}$ sites within the [$GaO_6$] octahedron outside the vicinity of dopants.
- path III-o: between two $O_{eq}$ sites of the [$GaO_6$] octahedra outside the vicinity of dopants.

Outside the vicinity of the dopants, the tendency of the O-migration is as same as the tendency of the O-deficient/reduced $LG_{-\delta}$: path III-o between two equatorial sites is more preferable than path II-o from apical site to equatorial site. Path III-o exhibits the low activation energy, i.e., $E_a \sim 0.27$ eV. The presence of the co-dopants, i.e., Sr and Mg, and $O^{vac}$ decreases greatly the migration activation energy in the O-deficient/reduced $LSGM_{-\delta}$. The values of activation energies got from the investigated paths show a good agreement with experimental [87, 106], which observed the activation energy $E_a = 0.78$ eV.

## 4.4 Summary

We performed DFT calculations to investigate the role of O-vacancy and dopants, i.e., Sr and Mg, in the co-doped (LaSr)(GaMg)$O_3$ (LSGM). The introduction of Mg and Sr dopant considerably decreases the O-vacancy formation energy, and thereby increase the concentration of O-vacancy in LSGM based materials. We also found that O vacancy formation energy is lowest at positions nearest the Sr ions and highest at O positions at the [MgO6] octahedron. This preference is due to the difference in the nature of the dopants in LSGM based materials. It indicates that O-vacancy is preferable on the position nearest to Sr dopant. The effect on the structural characteristics and electronic structures is primarily observed around the vicinity of the dopants and O-vacancy sites. With the suppression of excess electrons from the creation of O-vacancy, which was determined as the main reason of high activation energy in pristine LG-based materials (cf., chapter 3), the O-deficient/reduced co-doped $LSGM_{-\delta}$ shows the great decrease in activation energies in all considered O (O-vacancy)-migration paths. These results indicate the co-doped LSGM-based materials as good ionic conductors. The detail investigation of different O (O-vacancy)-migration paths shows that the small change of the bonds between O ions and cation ions, i.e., La, Sr, Ga, and Mg, can cause the drastic difference in term of activation energy. O (O-vacancy)-migration in the O-deficient/ reduced (LaSr)(GaMg)$O_{3-\delta}$ ($LSGM_{-\delta}$) has the similar tendency as pristine $LaGaO_3$-based materials: paths between two equatorial O sites are more favourable than path between apical site and equatorial site. The presence of Sr introduces an addition O-migration path with the low activation energy, i.e., O migration towards the vicinity of the Sr dopants from either the apical edge or the equatorial edge of the [$GaO_6$] octahedron.

# Chapter 5

# Summary, Conclusion and Outlook

In this dissertation, the improvement of metal oxides' reactivity through O-vacancy is presented. It starts from an understanding of how metal oxides function for realizing the desired reactivity related to green technology applications, which can be carried out within the framework of the density functional theory (DFT)-based investigation. Consequently, O-vacancy is introduced as one simple but effective way to modify metal oxides in order to improve the corresponding reactivity. Despite the advantages of the presence of O-vacancies, there are still some undesired effect of O-vacancies, which still needs to be considered. A detailed understanding of how O-vacancy affects metal oxides and their reactivity would enable us to avoid undesired effects of O-vacancies in order to improve more the efficiency of the desired reactivity; and, perhaps, even allow us to design oxide materials exhibiting specific, targeted functions. Two well-known case studies of metal oxides are provided: anatase $TiO_2(001)$ and lanthanum gallate ($LaGaO_3$) based materials.

Results showed a strong repulsion of the surface O atoms on the stoichiometric anatase $TiO_2(001)$. This is the assumed reason why it is difficult for $O_2$ molecule to adsorb on the stoichiometric surface. It is in agreement with experimental observations of anatase $TiO_2(001)$. An O-vacancy can be created at the 2-fold coordinated O ion on the surface, resulting in excess electrons. These excess electrons redistribute locally around the two neighboring 4-fold coordinated Ti ions, and an associated localized defect state appears in the corresponding electronic structure. The localized defect state can be described well with GGA+$U$. However, regardless of the value of $U$ considered, we find no significant qualitative change in the results of the $O_2$ adsorption on this surface, in terms of stable adsorption configuration and the states of adsorbed $O_2$. The presence of O-vacancy promotes $O_2$ adsorption on an initially inert stoichiometric $TiO_2(001)$. The O-vacancy sites became active sites, making $O_2$ adsorption favorable and exothermic. The adsorbed $O_2$ can be found either in superoxide state ($O_2^-$) and peroxide state ($O_2^{2-}$). The $O_2^-$ anion was formed when the O-O bond is oriented

parallel to the surface, along [010]. And the $O_2^{2-}$ anion was formed when the O-O bond is oriented perpendicular to the surface, along [001]. The superoxide anion becomes more stable than peroxide anion. Healing/migration of the surface occurs when one of the O atoms of the perpendicularly adsorbed $O_2$ fills the vacant site and the other atom diffuses, recovering the stoichiometric surface. The O-adatom can move easily to positions in the middle of the Ti−O bond along [010], but difficult for the O-adatom to diffuse to other positions. It could reduce the efficiency of the surface chemical reactions and slow down the catalytic reaction rate. However, the healing/migration effect occurs only on the less stable adsorption configurations. In essence, the introduction of O-vacancy can promote $O_2$ adsorption on anatase $TiO_2$(001).

The geometric and electronic structures of pristine/stoichiometric LG are based on the tilting of the [$GaO_6$] octahedrons from the ideal cubic perovskite structure. It is difficult to form O-vacancy in LG, as indicated by the calculated large O-vacancy formation energy. The equatorial O-positions of [$GaO_6$] octahedron are found to be more favorable than the apical O-positions for introducing O-vacancy. This preference is due to the difference in the nature of the bonds with the surrounding cation ions, especially the weak covalent bonding with La. The effect of O-vacancy on the structural characteristics is primarily observed around the vicinity of the vacancy site. The introduction of O-vacancy leads to excess electrons in the O-deficient LG ($LG_{-\delta}$). This induces the accumulation of charge between two 5-fold coordinated Ga ions, and an associated localized defect state appears in the corresponding electronic structure. The appearance of O-vacancy allows the O ion to migrate in $LG_{-\delta}$ through O hopping to the O-vacancy site. Calculated potential curves for O-migration show that the preferable migration paths are along the equatorial edges of the [$GaO_6$] octahedron with the high activation energy. The mechanism of O-migration reveals that excess electrons enhance not only the repulsive Coulomb interaction between the mobile O and the surrounding Ga ions, but also the attractive Coulomb interaction between the mobile O and the surrounding La ions. It is the reason for the high migration energy in pristine LG based materials.

From an understanding of the positive and negative effects of introducing O-vacancy in LG-based materials, doping at cation sites is proposed as one way to decrease O-vacancy formation energy and enhance the desired O-migration. Sr and Mg dopants at the La and Ga sites, respectively, were investigated with the dopant concentration $(La_{1-x}Sr_x)(Ga_{1-x}Mg_x)O_3$ (x=0.0625), i.e., LSGM. The effect of the dopants on the structural characteristics is primarily observed around

the vicinity of each of the dopant sites, same as the effect of O-vacancy. The presence of co-dopants at cations site suppresses the excess electrons resulting from the creation/presence of O-vacancy. This results in a significant decrease in O-vacancy formation energy, and therefore increases the concentration of O-vacancies. The O-vacancy formation energy shows the lowest value in the vicinity of the Sr ion and the highest value in the vicinity of Mg ion. It explains the experimental observation of the significant role of Sr in increasing O-vacancy concentration. With the suppression of excess electrons, which was determined as the main reason of high activation energy in pristine LG-based materials, a significant decrease in the activation energy for O (O-vacancies)-migration was observed. Apart from the preferable being between two equatorial O sites , i.e., same in LG-based materials, the introduction of dopants, especially Sr dopant at La sites, provides one more preferable migration path: migration paths towards the Sr dopants, either originating from the apical or equatorial edges of [$GaO_6$] octahedra. The dopants in this case play an important role of promoting the effect of O-vacancies through the enhancement of O (O-vacancy)-migration. Presence of both O-vacancies and dopants makes co-doped LSGM-based materials good ionic conductors for electrolyte of SOFC applications.

These studies show that understanding the effect of O-vacancy on various metal oxides, i.e., surface and periodic system, plays a key factor in the improvement of their reactivity for specific purposes, e.g., electrocatalytic reactions, ionic conductivity. The presence of excess electrons through the introduction of O-vacancies plays a major role in the improvement of metal oxides' reactivity. In some cases, O-vacancies can significantly improve metal oxides' reactivity by the introduction of excess electrons on the materials, e.g., enhancement the adsorption on the surface. In some cases, they can act as an obstacle for the desired reactivity, e.g., reason for high activation energy for O-migration in pristine LG-based materials. From this view-point, it is necessary to avoid the occurrence of excess electrons. The introduction of dopants at cation sites is clarified as an effective solution to solve this problem.

Taking advantage of this understanding in further research in order to improve various types of metal oxides for desired reactivity is one important tool we could employ. The improvement of metal oxides' reactivity through "defect engineering", i.e., O-vacancy, is proven to be a good approach, which we can apply for the further research of metal oxides and, also, for other material families.

# Appendix A

# Density Functional Theory Formalism

The basic idea of the DFT is that: the many-body problem of interacting electrons is mapped to a problem of one-particle reference system with the same density as the real system. This is performed by replacing the Schrödinger equation with the Kohn-Sham equation. This procedure is briefly introduced in the following.

## A.1 The Schrödinger Equation

Any electronic properties of matters are described by the Schrödinger equation. In this review, we consider time-independent Schrödinger equations, which are used in most cases. Within the Born-Oppenheimer non-relativistic approximation, this equation is given by:

$$\hat{H}\Psi(\mathbf{r}_1, \mathbf{r}_2, ..., \mathbf{r}_N) = E\Psi(\mathbf{r}_1, \mathbf{r}_2, ..., \mathbf{r}_N) \tag{A.1}$$

$$\hat{H} = \hat{T} + \hat{V}_{\text{nuc}-\text{ele}} + \hat{U} \tag{A.2}$$

where $E$ is the electronic energy, $\Psi(\mathbf{r}_1, \mathbf{r}_2, ..., \mathbf{r}_N)$ is the wave function, and $\hat{H}$ is the Hamiltonian operator including the kinetic energy operator $\hat{T}$ , the nuclei-electron interaction operator $\hat{V}_{\text{nuc}-\text{ele}}$, and the Coulomb interaction between electrons $\hat{U}$. The interaction of electrons with nuclei can be considered as a simple "external" potential $\hat{V}_{ext}$. For an $N$-electron system, the external potential $\hat{V}_{ext}$ completely determines the Hamiltonian (A.1). N and $\hat{V}_{ext}$ determine all properties of the non-degenerate ground state.

The probability density of finding an electron with any particular set of coordinates $\{\mathbf{r}_1, \mathbf{r}_2, ..., \mathbf{r}_N\}$ is $|\Psi(\mathbf{r}_1, \mathbf{r}_2, ..., \mathbf{r}_N|^2$. The electron density has a close relationship with this expression and is written as

$$\rho(\mathbf{r}) = N \int |\Psi(\mathbf{r}_1, \mathbf{r}_2, \mathbf{r}_3..., \mathbf{r}_n)|^2 d\mathbf{r}_1, d\mathbf{r}_2, d\mathbf{r}_3, ..., d\mathbf{r}_n \tag{A.3}$$

The lowest energy eigenvalue, $E_0$, is the ground state energy corresponding to the

ground state wave function $\Psi_0$. The ground state of the Schr$\acute{}$odinger equation is found by minimising the expectation value of the energy according to the *variational principle*

$$\delta[\langle\Psi|\hat{H}|\Psi\rangle - E\langle\Psi|\Psi\rangle] = 0 \tag{A.4}$$

Even with the variational principles, solving the Schrödinger equation by a direct minimisation of $N$-electron systems is still far from practical because the wave function has $3N$ degrees of freedom. One of the best methods to avoid this difficulty is to use the electron density, by which the ground state energy is determined, instead of the wave function itself.

## A.2 Hohenberg-Kohn Theorems

The Hohenberg-Kohn theorems enable us to solve the Schrödinger equation by using the electron density $\rho(\mathbf{r})$ as a basic variable [107].

There are composed of two theorems: the first theorem is stated as *"The external potential $\nu_{ext}(\mathbf{r})$ is, except for a constant, uniquely determined by the electron density $\rho(\mathbf{r})$"*. Since $\rho(\mathbf{r})$ determines the number of electrons as $N = \int \rho_t(\mathbf{r})d\mathbf{r}$, $\rho(\mathbf{r})$ also determines the ground state wave function and all other electronic properties of the system. In principle, given the ground state electron density, the Hamiltonian operator is uniquely determined.

The second theorem establishes a variational principle: *"For any positive definite trial density $\rho_t(\mathbf{r})$ such that $\int \rho_t(\mathbf{r})d\mathbf{r} = N$, then $E[\rho_t] \geq E_0$"*, where $E_0$ is the true ground state energy, and $E[\rho_t]$ is defined as the sum of the kinetic interaction, electron-electron interaction and external potential functionals, $E[\rho_t] = T[\rho_t] + U[\rho_t] + \int \rho_t(\mathbf{r})\nu_{ext}d\mathbf{r}$.

The Hohenberg-Kohn theorems established the one-to-one correspondence between ground state $\rho(\mathbf{r})$ and the external potential $\nu_{ext}(\mathbf{r})$. 3-dimensional electron density functions now become a basic variable. The ground state and ground state energy can be obtained by minimizing the energy functional with respect to the electron density. It makes a great simplification of solving many-body problems.

## A.3 Kohn-Sham Equation

Kohn and Sham pointed out an exact way to consider the electronic structures of condensed matters [108]. As is mentioned above, the ground state total energy of the system for a given external potential $\nu_{ext}(\mathbf{r})$ is:

$$E[\rho_t] = T[\rho] + U[\rho] + \int \rho(\mathbf{r})\nu_{ext}d\mathbf{r} \tag{A.5}$$

Since $\nu_{ext}$ appears only in $\int \rho(\mathbf{r})\nu_{ext}d\mathbf{r}$, the functionals $T[\rho]$ and $U[\rho]$ are the universal functionals of the density, independent of $\nu_{ext}$. Here, they introduced a fictitious system of $N$ non-interacting electrons that are described by single electron wave functions with $N$ "orbitals" $\psi$. In this system, the ground state density is expressed as:

$$\rho = \sum_{i}^{N} |\psi_i|^2 \tag{A.6}$$

The kinetic energy of the non-interacting system of electron is write on:

$$T_{\mathrm{S}}[\rho] = -\frac{1}{2}\sum_{i}^{N}\langle\psi_i|\nabla|^2\psi_i\rangle \tag{A.7}$$

The important point is that a significant part of the electron-electron interaction $U[\rho]$ is the classical Coulomb interaction or Hartree energy $V_{\mathrm{H}}$. This we can write in terms of electron density as:

$$V_{\mathrm{H}} = \frac{1}{2}\int\int \frac{\rho(\mathbf{r})\rho(\mathbf{r}')}{|\mathbf{r}-\mathbf{r}'|}d\mathbf{r}d\mathbf{r}' \tag{A.8}$$

Thus the energy functional can be rearranged as:

$$E[\rho] = T_{\mathrm{S}}[\rho] + V_{ext}[\rho] + V_{\mathrm{H}}[\rho] + E_{xc}[\rho] \tag{A.9}$$

Where, the *exchange-correlation functional* $E_{xc}[\rho]$ is introduced. All the many-body effects are counted in $E_{xc}[\rho]$.

$$E_{xc} = (T - T_{\mathrm{S}}) + (U - V_{\mathrm{H}}) \tag{A.10}$$

The variational equation given by Hohenberg and Kohn, $\dfrac{\delta E}{\delta\rho}$, becomes

$$\frac{\delta T_0}{\delta\rho} + \nu_{ext} + \int \frac{\rho(\mathbf{r}')}{|\mathbf{r}-\mathbf{r}'|}d\mathbf{r}' + \nu_{xc} = 0 \tag{A.11}$$

where

$$\nu_{xc} = \frac{\delta E_{xc}}{\delta\rho} \tag{A.12}$$

Then, the so-called Kohn-Sham equations are obtained:

$$\left[-\frac{1}{2}\nabla^2 + \nu_{eff}(\mathbf{r})\right]\psi_i(\mathbf{r}) = \varepsilon_i\psi_i(\mathbf{r}) \tag{A.13}$$

$$\nu_{eff}(\mathbf{r}) = \nu_{ext} + \int \frac{\rho(\mathbf{r}')}{|\rho\mathbf{r} - \mathbf{r}'|}d\mathbf{r}' + \nu_{xc} \tag{A.14}$$

This set of non-linear equation (the Kohn-Sham equations) describes the behaviours of non-interacting "electrons" in an effective local potential. For the exact functional, and thus exact local potential, the "orbitals" yields the exact ground state density via Eq. A.6 and exact ground state energy via Eq. A.9.

It is notable that there is no approximation used until this point. In the Kohn-Sham equation, the exchange-correlation energy seems to be much smaller than kinetic energy and Hartree energy, and all of difficulties are included in this part. The exchange-correlation potential in Eq. A.14 is the universal functional of the electron density, which is same for any systems from molecules to bulk systems. The exact form of this potential is unknown. However several approximations have been proposed for exchange-correlation potential. Among them, two of the most useful approximations are the local density approximation (LDA), which was proposed in 1960s [107,108], and generalized gradient approximation (GGA), which was reported later by Perdew et al. [109–111].

## A.4 Approximations for Exchange-Correlation Functional

The major problem of the DFT is that the exact functional of exchange-correlation energy is not known. Using approximations for the exchange-correlation energy allows us to solve the Kohn-Sham equations for solids. LDA and GGA are the most well-known approximations.

In the LDA, the representation for $E_{xc}[\rho]$ is given by a simple function of the local charge density $\varepsilon_{xc}[\rho]$. Here, $\varepsilon_{xc}[\rho]$ is the exchange correlation energy per electron of a homogeneous electron gas of density $\rho$. The as approximate expression for the exchange-correlation energy is given by:

$$E_{xc}[\rho] = \int \rho(\mathbf{r})\varepsilon_{xc}(\rho)d\mathbf{r} \tag{A.15}$$

Since $\varepsilon_{xc}(\rho)$ is a function of only the local value of the density, the functional $E_{xc}(\rho)$ is constructed as a sum of the local exchange-correlation energies. The remarkable performance of the LDA is its reasonable description of the spherically

averaged exchange correlation hole.

A natural progression beyond the LDA is obviously taking gradients of the charge density at a local point. In the GGA, the exchange-correlation energy depends on both the density and its gradients, but the analytic properties of LDA remains. The typical form of the GGA is:

$$E_{xc}[\rho] = \int \rho(\mathbf{r})\varepsilon_{xc}(\rho, \nabla\rho)d\mathbf{r} \tag{A.16}$$

In some cases the GGA significantly improves the LDA ' s description of the binding energy.

## A.5 Implementation of DFT

In the calculations presented in this dissertation, spin-polarized density functional theory calculation were implemented via the Vienna ab-initio simulation pakage (VASP) [112, 113].

For the investigation on the metal oxides' surface, i.e., anatase $TiO_2(001)$, the supercell approach is used. The surface was modelled using infinitely repeating periodic slabs of atoms separated by vacuum layers. The slab should be thick enough to accurately simulate the surface of material. With the introduction of adsorption in the calculations, the asymmetry of the slab model containing the adsorbate create a net dipole moment in the direction of the surface, and slow down the energy convergence in the respect with the supercell size. In order to reduce this effect, electric dipole correction layer in the vacuum area was used to cute the dipole interactions between the repeated image layer systems [114, 115].

Within the Bloch's theorem, for an electron in a periodic potential, the electronic wave function at each $\mathbf{k}$ point can be expanded in terms of a discrete plane-wave basis set:

$$\psi_{j,\mathbf{k}}(\mathbf{r}) = \sum_{\mathbf{G}} C_{\mathbf{k}+\mathbf{G}} e^{i(\mathbf{k}+\mathbf{G}).\mathbf{r}} \tag{A.17}$$

where, $\mathbf{G}$ is the reciproval lattice vector and $\mathbf{k}$ is set to lie within the first Brillouin zone. Substituting Eq. A.17 to Eq. A.13 and taking the inner product, the Kohn-Sham equations in the plane-wave representation can be written as:

$$\sum_{\mathbf{G}} \left[ -\frac{1}{2}|\mathbf{k}+\mathbf{G}|^2 \delta_{\mathbf{G}\mathbf{G}'} + \nu_{eff}(\mathbf{G}-\mathbf{G}') \right] = \varepsilon_j C_{j,\mathbf{k}+\mathbf{G}'} \tag{A.18}$$

In principle, an inifinite plane-wave basis set is required in expanding the electronic wave funxtions, However, the coefficients $C_{j,\mathbf{k}+\mathbf{G}'}$ for the plane waves with small kinetic energy $-\frac{1}{2}|\mathbf{k}+\mathbf{G}|^2$ are more important than those with large kinetic energy. Hence, a certain *kinetic energy cutoff* (i.e., $E_{\text{cutoff}}$) for plane-waves which defines the size of the matrix to be setup for diagonalization. Numerical convergence for the $E_{\text{cutoff}}$ is performed as a standard first step in plane-waves calculations. It was chosen $E_{\text{cutoff}}$=540 eV for anatase $TiO_2$(001) and $E_{\text{cutoff}}$=600 eV for the pristine and doped $LaGaO_3$-based materials.

In the infinite periodic system, the total energy calculations of the crystal requires an infinite number of **k** points. However, since electronics wave functions at **k** points are almost identical for the points close together. It leads that only finite number of "special" **k** point may be necessary. The first Brillouin zone integrations were carried out by Monkhorst-Pack scheme [116] for generating sets of **k** points with Methfessel-Paxtion smearing [117] of $\sigma = 0.1$ eV. While Monkhorst-Pack **k** points of $5 \times 5 \times 1$ was used for anatase $TiO_2$(001), the **k** points are chosen $3 \times 3 \times 3$ for the pristine and doped LG-based materials.

Other conditions was used, e.g. conjugate-gradient algorithm for the relaxation into the ground state, harmonic vibrational frequencies using finite difference method with step size of 0.02 Å. The electron-ion interactions were described by the projector-augmented wave (PAW) potentials. [118]. Calculations of O-migration and the corresponding activation migration energy were implemented using climbing image nudged elastic band (CI-NEB) [119].

# Bibliography


[1] S.-W. Cheong. "Transition metal oxides: The exciting world of orbitals." *Nature Materials* **6**(12), 927–928 (2007).

[2] M. Ho, P. Khiew, D. Isa, T. Tan, W. Chiu, and C. Chia. "A review of metal oxide composite electrode materials for electrochemical capacitors." *Nano* **9**(06), 1430002 (2014).

[3] U. Diebold, N. Ruzycki, G. S. Herman, and A. Selloni. "One step towards bridging the materials gap: surface studies of $TiO_2$ anatase." *Catalysis Today* **85**(2), 93–100 (2003).

[4] M. Pena and J. Fierro. "Chemical structures and performance of perovskite oxides." *Chemical Reviews* **101**(7), 1981–2018 (2001).

[5] G. Pacchioni. "Oxygen vacancy: the invisible agent on oxide surfaces." *ChemPhysChem* **4**(10), 1041–1047 (2003).

[6] D. Matsunaka, H. Kasai, H. Nakanishi, and A. Okiji. "Effects of oxygen vacancies on the electronic states in copper oxides." *Journal of the Physical Society of Japan* **71**(9), 2247–2252 (2002).

[7] R. Schaub, E. Wahlström, A. Rønnau, E. Lægsgaard, I. Stensgaard, and F. Besenbacher. "Oxygen-mediated diffusion of oxygen vacancies on the $TiO_2$ (110) surface." *Science* **299**(5605), 377–379 (2003).

[8] K. Rajeshwar. "Hydrogen generation at irradiated oxide semiconductor–solution interfaces." *Journal of Applied Electrochemistry* **37**(7), 765–787 (2007).

[9] M. G. Walter, E. L. Warren, J. R. McKone, S. W. Boettcher, Q. Mi, E. A. Santori, and N. S. Lewis. "Solar water splitting cells." *Chemical Reviews* **110**(11), 6446–6473 (2010).

[10] B. O'regan and M. Grätzel. "A low-cost, high-efficiency solar cell based on dye-sensitized colloidal $TiO_2$ films." *Nature* **353**(6346), 737–740 (1991).

[11] P. V. Kamat. "Photochemistry on nonreactive and reactive (semiconductor) surfaces." *Chemical Reviews* **93**(1), 267–300 (1993).

[12] M. A. Henderson. "A surface science perspective on photocatalysis." *Surface Science Reports* **66**(6), 185–297 (2011).

[13] M. Batzill, E. H. Morales, and U. Diebold. "Influence of nitrogen doping on the defect formation and surface properties of $TiO_2$ rutile and anatase." *Physical Review Letters* **96**(2), 026103 (2006).

[14] J.-H. Kim, A. Ishihara, S. Mitsushima, N. Kamiya, and K.-I. Ota. "Catalytic activity of titanium oxide for oxygen reduction reaction as a non-platinum catalyst for PEFC." *Electrochimica Acta* **52**(7), 2492–2497 (2007).

[15] M. Chisaka, A. Ishihara, K. Suito, K.-i. Ota, and H. Muramoto. "Oxygen reduction reaction activity of nitrogen-doped titanium oxide in acid media." *Electrochimica Acta* **88**, 697–707 (2013).

[16] K.-i. Ota, Y. Ohgi, K.-D. Nam, K. Matsuzawa, S. Mitsushima, and A. Ishihara. "Development of group 4 and 5 metal oxide-based cathodes for polymer electrolyte fuel cell." *Journal of Power Sources* **196**(12), 5256–5263 (2011).

[17] A. Fujishima. "Electrochemical photolysis of water at a semiconductor electrode." *Nature* **238**, 37–38 (1972).

[18] A. Fujishima, X. Zhang, and D. A. Tryk. "$TiO_2$ photocatalysis and related surface phenomena." *Surface Science Reports* **63**(12), 515–582 (2008).

[19] L. Kavan, M. Grätzel, S. Gilbert, C. Klemenz, and H. Scheel. "Electrochemical and photoelectrochemical investigation of single-crystal anatase." *Journal of the American Chemical Society* **118**(28), 6716–6723 (1996).

[20] K. I. Hadjiivanov and D. G. Klissurski. "Surface chemistry of titania (anatase) and titania-supported catalysts." *Chemical Society Reviews* **25**(1), 61–69 (1996).

[21] M. Lazzeri, A. Vittadini, and A. Selloni. "Structure and energetics of stoichiometric $TiO_2$ anatase surfaces." *Physical Review B* **63**(15), 155409 (2001).

[22] Z. Zhao, Z. Li, and Z. Zou. "Surface properties and electronic structure of low-index stoichiometric anatase $TiO_2$ surfaces." *Journal of Physics: Condensed Matter* **22**(17), 175008 (2010).

[23] A. Vittadini, A. Selloni, F. Rotzinger, and M. Grätzel. "Structure and energetics of water adsorbed at $TiO_2$ anatase\(101\) and\(001\) surfaces." *Physical Review Letters* **81**(14), 2954 (1998).

[24] H. Ariga, T. Taniike, H. Morikawa, M. Tada, B. K. Min, K. Watanabe, Y. Matsumoto, S. Ikeda, K. Saiki, and Y. Iwasawa. "Surface-mediated visible-light photo-oxidation on pure $TiO_2$ (001)." *Journal of the American Chemical Society* **131**(41), 14670–14672 (2009).

[25] W. Zeng, T. Liu, Z. Wang, S. Tsukimoto, M. Saito, and Y. Ikuhara. "Oxygen Adsorption on Anatase $TiO_2$ (101) and (001) surfaces from first principles." *Materials Transactions* **51**(1), 171–175 (2010).

[26] R. Hengerer, B. Bolliger, M. Erbudak, and M. Grätzel. "Structure and stability of the anatase $TiO_2$ (101) and (001) surfaces." *Surface Science* **460**(1), 162–169 (2000).

[27] G. S. Herman, M. R. Sievers, and Y. Gao. "Structure determination of the two-domain (1× 4) anatase $TiO_2$ (001) surface." *Physical Review Letters* **84**(15), 3354 (2000).

[28] G. Herman, Y. Gao, T. Tran, and J. Osterwalder. "X-ray photoelectron diffraction study of an anatase thin film: $TiO_2$(001)." *Surface Science* **447**(1â"3), 201 – 211 (2000).

[29] M. Calatayud and C. Minot. "Effect of relaxation on structure and reactivity of anatase (100) and (001) surfaces." *Surface Science* **552**(1), 169–179 (2004).

[30] R. Hengerer, L. Kavan, P. Krtil, and M. Grätzel. "Orientation Dependence of Charge-Transfer Processes on $TiO_2$ (Anatase) Single Crystals." *Journal of the Electrochemical Society* **147**(4), 1467–1472 (2000).

[31] G. Shukri and H. Kasai. "Density functional theory study of ethylene adsorption on clean anatase $TiO_2$ (001) surface." *Surface Science* **619**, 59–66 (2014).

[32] Y. Liang, S. Gan, S. A. Chambers, and E. I. Altman. "Surface structure of anatase $TiO_2$ (001): reconstruction, atomic steps, and domains." *Physical Review B* **63**(23), 235402 (2001).

[33] A. Thomas, W. Flavell, A. Mallick, A. Kumarasinghe, D. Tsoutsou, N. Khan, C. Chatwin, S. Rayner, G. Smith, R. Stockbauer *et al.* "Comparison of the electronic structure of anatase and rutile $TiO_2$ single-crystal surfaces using resonant photoemission and X-ray absorption spectroscopy." *Physical Review B* **75**(3), 035105 (2007).

[34] G. Liu, H. G. Yang, X. Wang, L. Cheng, H. Lu, L. Wang, G. Q. Lu, and H.-M. Cheng. "Enhanced photoactivity of oxygen-deficient anatase $TiO_2$ sheets with dominant {001} facets." *The Journal of Physical Chemistry C* **113**(52), 21784–21788 (2009).

[35] M. Lazzeri and A. Selloni. "Stress-Driven Reconstruction of an Oxide Surface: The Anatase $TiO_2$ (001)-(1× 4) Surface." *Physical Review Letters* **87**(26), 266105 (2001).

[36] F. De Angelis, C. Di Valentin, S. Fantacci, A. Vittadini, and A. Selloni. "Theoretical Studies on Anatase and Less Common $TiO_2$ Phases: Bulk, Surfaces, and Nanomaterials." *Chemical Reviews* **114**(19), 9708–9753 (2014).

[37] V. E. Henrich, G. Dresselhaus, and H. Zeiger. "Observation of Two-Dimensional Phases Associated with Defect States on the Surface of $TiO_2$." *Physical Review Letters* **36**(22), 1335 (1976).

[38] G. Lu, A. Linsebigler, and J. T. Yates Jr. "$Ti^{3+}$ defect sites on $TiO_2$ (110): production and chemical detection of active sites." *The Journal of Physical Chemistry* **98**(45), 11733–11738 (1994).

[39] C. Di Valentin, G. Pacchioni, and A. Selloni. "Reduced and n-type doped $TiO_2$: nature of $Ti^{3+}$ species." *The Journal of Physical Chemistry C* **113**(48), 20543–20552 (2009).

[40] R. L. Kurtz, R. Stock-Bauer, T. E. Msdey, E. Román, and J. De Segovia. "Synchrotron radiation studies of $H_2O$ adsorption on $TiO_2$ (110)." *Surface Science* **218**(1), 178–200 (1989).

[41] M. A. Henderson, W. S. Epling, C. H. Peden, and C. L. Perkins. "Insights into photoexcited electron scavenging processes on $TiO_2$ obtained from studies of the reaction of $O_2$ with OH groups adsorbed at electronic defects on $TiO_2$ (110)." *The Journal of Physical Chemistry B* **107**(2), 534–545 (2003).

[42] K. Komaguchi, H. Nakano, A. Araki, and Y. Harima. "Photoinduced electron transfer from anatase to rutile in partially reduced $TiO_2$ (P-25) nanoparticles: an ESR study." *Chemical Physics Letters* **428**(4), 338–342 (2006).

[43] S. Wendt, P. T. Sprunger, E. Lira, G. K. Madsen, Z. Li, J. Ø. Hansen, J. Matthiesen, A. Blekinge-Rasmussen, E. Lægsgaard, B. Hammer *et al.* "The role of interstitial sites in the Ti3d defect state in the band gap of titania." *Science* **320**(5884), 1755–1759 (2008).

[44] G. Mattioli, F. Filippone, and A. Amore Bonapasta. "Reaction intermediates in the photoreduction of oxygen molecules at the (101) $TiO_2$ (anatase) surface." *Journal of the American Chemical Society* **128**(42), 13772–13780 (2006).

[45] F. Filippone, G. Mattioli, and A. A. Bonapasta. "Reaction intermediates and pathways in the photoreduction of oxygen molecules at the (101) TiO 2 (anatase) surface." *Catalysis Today* **129**(1), 169–176 (2007).

[46] U. Aschauer, J. Chen, and A. Selloni. "Peroxide and superoxide states of adsorbed $O_2$ on anatase $TiO_2$ (101) with subsurface defects." *Physical Chemistry Chemical Physics* **12**(40), 12956–12960 (2010).

[47] T. Berger, M. Sterrer, O. Diwald, E. Knözinger, D. Panayotov, T. L. Thompson, and J. T. Yates. "Light-induced charge separation in anatase $TiO_2$ particles." *The Journal of Physical Chemistry B* **109**(13), 6061–6068 (2005).

[48] E. Carter, A. F. Carley, and D. M. Murphy. "Evidence for $O_2$-radical stabilization at surface oxygen vacancies on polycrystalline $TiO_2$." *The Journal of Physical Chemistry C* **111**(28), 10630–10638 (2007).

[49] A. Fahmi, C. Minot, B. Silvi, and M. Causa. "Theoretical analysis of the structures of titanium dioxide crystals." *Physical Review B* **47**(18), 11717 (1993).

[50] Y. Gai, J. Li, S.-S. Li, J.-B. Xia, and S.-H. Wei. "Design of narrow-gap $TiO_2$: a passivated codoping approach for enhanced photoelectrochemical activity." *Physical Review Letters* **102**(3), 036402 (2009).

[51] E. Finazzi, C. Di Valentin, G. Pacchioni, and A. Selloni. "Excess electron states in reduced bulk anatase $TiO_2$: comparison of standard GGA,

GGA+ U, and hybrid DFT calculations." *The Journal of Chemical Physics* **129**(15), 154113–154113 (2008).

[52] M. Landmann, E. Rauls, and W. Schmidt. "The electronic structure and optical response of rutile, anatase and brookite $TiO_2$." *Journal of Physics: Condensed Matter* **24**(19), 195503 (2012).

[53] J. P. Perdew and M. Levy. "Physical content of the exact Kohn-Sham orbital energies: band gaps and derivative discontinuities." *Physical Review Letters* **51**(20), 1884 (1983).

[54] A. Zunger, J. Perdew, and G. Oliver. "A self-interaction corrected approach to many-electron systems: Beyond the local spin density approximation." *Solid State Communications* **34**(12), 933–936 (1980).

[55] S. Yotsuhashi, Y. Yamada, W. A. Diño, H. Nakanishi, and H. Kasai. "Dependence of oxygen dissociative adsorption on platinum surface structures." *Physical Review B* **72**(3), 033415 (2005).

[56] S. Yotsuhashi, Y. Yamada, T. Kishi, W. A. Diño, H. Nakanishi, and H. Kasai. "Dissociative adsorption of $O_2$ on Pt and Au surfaces: Potential-energy surfaces and electronic states." *Physical Review B* **77**(11), 115413 (2008).

[57] A. Roldán, M. Boronat, A. Corma, and F. Illas. "Theoretical confirmation of the enhanced facility to increase oxygen vacancy concentration in $TiO_2$ by iron doping." *The Journal of Physical Chemistry C* **114**(14), 6511–6517 (2010).

[58] A. Thomas, W. Flavell, A. Kumarasinghe, A. Mallick, D. Tsoutsou, G. Smith, R. Stockbauer, S. Patel, M. Grätzel, and R. Hengerer. "Resonant photoemission of anatase $TiO_2$ (101) and (001) single crystals." *Physical Review B* **67**(3), 035110 (2003).

[59] Y. Wang, H. Sun, S. Tan, H. Feng, Z. Cheng, J. Zhao, A. Zhao, B. Wang, Y. Luo, J. Yang *et al.* "Role of point defects on the reactivity of reconstructed anatase titanium dioxide (001) surface." *Nature Communications* **4** (2013).

[60] S. Dudarev, G. Botton, S. Savrasov, C. Humphreys, and A. Sutton. "Electron-energy-loss spectra and the structural stability of nickel oxide: An LSDA+ U study." *Physical Review B* **57**(3), 1505 (1998).

[61] V. E. Henrich and R. L. Kurtz. "Surface electronic structure of $TiO_2$: Atomic geometry, ligand coordination, and the effect of adsorbed hydrogen." *Physical Review B* **23**(12), 6280 (1981).

[62] Z. Zhang, S.-P. Jeng, and V. E. Henrich. "Cation-ligand hybridization for stoichiometric and reduced $TiO_2$ (110) surfaces determined by resonant photoemission." *Physical Review B* **43**(14), 12004 (1991).

[63] R. Heise, R. Courths, and S. Witzel. "Valence band densities-of-states of $TiO_2$ (110) from resonant photoemission and photoelectron diffraction." *Solid State Communications* **84**(6), 599–602 (1992).

[64] R. C. Weast, M. Astle, and W. Beyer. *1985: CRC handbook of chemistry and physics*. CRC Press, Inc., Boca Raton, FL (1985).

[65] W. Tang, E. Sanville, and G. Henkelman. "A grid-based Bader analysis algorithm without lattice bias." *Journal of Physics: Condensed Matter* **21**(8), 084204 (2009).

[66] M.-h. Shao, P. Liu, and R. R. Adzic. "Superoxide anion is the intermediate in the oxygen reduction reaction on platinum electrodes." *Journal of the American Chemical Society* **128**(23), 7408–7409 (2006).

[67] T. Q. Nguyen, M. C. S. Escaño, H. Nakanishi, H. Kasai, H. Maekawa, K. Osumi, and K. Sato. "DFT+U study on the oxygen adsorption and dissociation on $CeO_2$-supported platinum cluster." *Applied Surface Science* **288**, 244–250 (2014).

[68] J. L. Gland, B. A. Sexton, and G. B. Fisher. "Oxygen interactions with the Pt (111) surface." *Surface Science* **95**(2), 587–602 (1980).

[69] H. Steininger, S. Lehwald, and H. Ibach. "Adsorption of oxygen on Pt (111)." *Surface Science* **123**(1), 1–17 (1982).

[70] D. Outka, J. Stöhr, W. Jark, P. Stevens, J. Solomon, and R. Madix. "Orientation and bond length of molecular oxygen on Ag (110) and Pt (111): A near-edge x-ray-absorption fine-structure study." *Physical Review B* **35**(8), 4119 (1987).

[71] Y. Lei, F. Niu, H. Mei, Q. Liu, C. Pan, and W. Xiao. "Adsorption and diffusion studies of an O adatom on $TiO_2$ anatase surfaces with first principles calculations." *Computational Materials Science* **63**, 58–65 (2012).

[72] Y.-F. Li, Z.-P. Liu, L. Liu, and W. Gao. "Mechanism and activity of photocatalytic oxygen evolution on titania anatase in aqueous surroundings." *Journal of the American Chemical Society* **132**(37), 13008–13015 (2010).

[73] A. Chroneos, R. Vovk, I. Goulatis, and L. Goulatis. "Oxygen transport in perovskite and related oxides: A brief review." *Journal of Alloys and Compounds* **494**(1–2), 190 – 195 (2010).

[74] J. Zhu, H. Li, L. Zhong, P. Xiao, X. Xu, X. Yang, Z. Zhao, and J. Li. "Perovskite Oxides: Preparation, Characterizations, and Applications in Heterogeneous Catalysis." *ACS Catalysis* **4**(9), 2917–2940 (2014).

[75] A. B. Stambouli and E. Traversa. "Solid oxide fuel cells (SOFCs): a review of an environmentally clean and efficient source of energy." *Renewable and Sustainable Energy Reviews* **6**(5), 433–455 (2002).

[76] P. Huang and A. Petric. "Superior oxygen ion conductivity of lanthanum gallate doped with strontium and magnesium." *Journal of the Electrochemical Society* **143**(5), 1644–1648 (1996).

[77] J. Stevenson, T. Armstrong, D. McCready, L. Pederson, and W. Weber. "Processing and Electrical Properties of Alkaline Earth-Doped Lanthanum Gallate." *Journal of the Electrochemical Society* **144**(10), 3613–3620 (1997).

[78] M. S. Islam. "Computer modelling of defects and transport in perovskite oxides." *Solid State Ionics* **154**, 75–85 (2002).

[79] T. Phan Thuy Linh, M. Sakaue, M. Alaydrus, T. Dewi Kencana Wungu, S. Meñez Aspera, H. Kasai, T. Mohri, and T. Ishihara. "Electronic and Oxygen Migration Properties of Monoclinic $La_2GeO_{5-\delta}$." *Journal of the Physical Society of Japan* **82**(8), 084702 (2013).

[80] T. P. T. Linh, M. Sakaue, S. M. Aspera, M. Alaydrus, T. D. K. Wungu, N. H. Linh, H. Kasai, T. Mohri, and T. Ishihara. "First-principles calculation on oxygen ion migration in alkaline-earth doped La 2 GeO 5." *Journal of Physics: Condensed Matter* **26**(25), 255503 (2014).

[81] W. Marti, P. Fischer, F. Altorfer, H. Scheel, and M. Tadin. "Crystal structures and phase transitions of orthorhombic and rhombohedral $RGaO_3$ (R= La, Pr, Nd) investigated by neutron powder diffraction." *Journal of Physics: Condensed Matter* **6**(1), 127 (1994).

[82] L. Vasylechko, A. Matkovski, A. Suchocki, D. Savytskii, and I. Syvorotka. "Crystal structure of $LaGaO_3$ and (La, Gd)$GaO_3$ solid solutions." *Journal of Alloys and Compounds* **286**(1), 213–218 (1999).

[83] M. Lerch, H. Boysen, and T. Hansen. "High-temperature neutron scattering investigation of pure and doped lanthanum gallate." *Journal of Physics and Chemistry of solids* **62**(3), 445–455 (2001).

[84] C. J. Howard and B. J. Kennedy. "The orthorhombic and rhombohedral phases of-a neutron powder diffraction study." *Journal of Physics: Condensed Matter* **11**(16), 3229 (1999).

[85] P. Dhak, P. Pramanik, S. Bhattacharya, A. Roy, S. N. Achary, and A. K. Tyagi. "Structural phase transition in lanthanum gallate as studied by Raman and X-ray diffraction measurements." *Physica Status Solidi (b)* **248**(8), 1884–1893 (2011).

[86] B. J. Kennedy, T. Vogt, C. D. Martin, J. B. Parise, and J. A. Hriljac. "Pressure-induced orthorhombic to rhombohedral phase transition in $LaGaO_3$." *Journal of Physics: Condensed Matter* **13**(48), L925–L930 (2001).

[87] J. Drennan, V. Zelizko, D. Hay, F. T. Ciacchi, S. Rajendran, and S. P. Badwal. "Characterisation, conductivity and mechanical properties of the oxygen-ion conductor $La_{0.9}Sr_{0.1}Ga_{0.8}Mg_{0.2}O_{3-x}$." *Journal of Materials Chemistry* **7**(1), 79–83 (1997).

[88] F. Blanc, D. S. Middlemiss, L. Buannic, J. L. Palumbo, I. Farnan, and C. P. Grey. "Thermal phase transformations in $LaGaO_3$ and $LaAlO_3$ perovskites: An experimental and computational solid-state NMR study." *Solid State Nuclear Magnetic Resonance* **42**, 87 – 97 (2012).

[89] N. H. Linh, T. Q. Nguyen, W. A. Diño, and H. Kasai. "Effect of oxygen vacancy on the adsorption of $O_2$ on anatase $TiO_2$ (001): A DFT-based study." *Surface Science* **633**, 38–45 (2015).

[90] E. Djurado and M. Labeau. "Second phases in doped lanthanum gallate perovskites." *Journal of the European Ceramic Society* **18**(10), 1397 – 1404 (1998).

[91] T. Ishihara, H. Matsuda, and Y. Takita. "Doped $LaGaO_3$ Perovskite Type Oxide as a New Oxide Ionic Conductor." *Journal of the American Chemical Society* **116**(9), 3801–3803 (1994).

[92] T. Ishihara, H. Matsuda, and Y. Takita. "Effects of rare earth cations doped for La site on the oxide ionic conductivity of $LaGaO_3$-based perovskite type oxide." *Solid State Ionics* **79**, 147 – 151 (1995).

[93] M. Feng, J. B. Goodenough, K. Huang, and C. Milliken. "Fuel cells with doped lanthanum gallate electrolyte." *Journal of Power Sources* **63**(1), 47–51 (1996).

[94] D. Lybye, F. W. Poulsen, and M. Mogensen. "Conductivity of A-and B-site doped $LaAlO_3$, $LaGaO_3$, $LaScO_3$ and $LaInO_3$ perovskites." *Solid State Ionics* **128**(1), 91–103 (2000).

[95] V. Thangadurai, A. Shukla, and J. Gopalakrishnan. "$La_{0.9}Sr_{0.1}Ga_{0.8}Mn_{0.2}O_{2.85}$: a new oxide ion conductor." *Chemical Communications* (23), 2647–2648 (1998).

[96] P. Slater, J. Irvine, T. Ishihara, and Y. Takita. "The structure of the oxide ion conductor $La_{0.9}Sr_{0.1}Ga_{0.8}Mg_{0.2}O_{2.85}$ by powder neutron diffraction." *Solid State Ionics* **107**(3), 319–323 (1998).

[97] K. Huang, R. S. Tichy, and J. B. Goodenough. "Superior Perovskite Oxide-Ion Conductor; Strontium-and Magnesium-Doped $LaGaO_3$: I, Phase Relationships and Electrical Properties." *Journal of the American ceramic society* **81**(10), 2565–2575 (1998).

[98] L. Vasylechko, V. Vashook, D. Savytskii, A. Senyshyn, R. Niewa, M. Knapp, H. Ullmann, M. Berkowski, A. Matkovskii, and U. Bismayer. "Crystal structure, thermal expansion and conductivity of anisotropic $La_{1-x}Sr_xGa_{1-2x}Mg_{2x}O_{3-y}$ (x= 0.05, 0.1) single crystals." *Journal of Solid State Chemistry* **172**(2), 396–411 (2003).

[99] J. Cheng and A. Navrotsky. "Energetics of magnesium, strontium, and barium doped lanthanum gallate perovskites." *Journal of Solid State Chemistry* **177**(1), 126 – 133 (2004).

[100] K. Huang and J. B. Goodenough. "A solid oxide fuel cell based on Sr- and Mg-doped $LaGaO_3$ electrolyte: the role of a rare-earth oxide buffer." *Journal of Alloys and Compounds* **303–304**, 454–464 (2000).

[101] T. Ishihara, M. Honda, T. Shibayama, H. Furutani, and Y. Takita. "An intermediate temperature solid oxide fuel cell utilizing superior oxide ion conducting electrolyte, doubly doped $LaGaO_3$ perovskite." *Ionics* **4**(5-6), 395–402 (1998).

[102] T. Ishihara, T. Akbay, H. Furutani, and Y. Takita. "Improved oxide ion conductivity of Co doped $La_{0.8}Sr_{0.2}Ga_{0.8}Mg_{0.2}O_3$ perovskite type oxide." *Solid State Ionics* **113**, 585–591 (1998).

[103] T. Ishihara, T. Shibayama, H. Nishiguchi, and Y. Takita. "Oxide ion conductivity in $La_{0.8}Sr_{0.2}Ga_{0.8}Mg_{0.2\ X}Ni_XO3$ perovskite oxide and application for the electrolyte of solid oxide fuel cells." *Journal of Materials Science* **36**(5), 1125–1131 (2001).

[104] P. Majewski, M. Rozumek, and F. Aldinger. "Phase diagram studies in the systems $La_2O_3$–SrO–MgO–$Ga_2O_3$ at 1350–1400 ° C in air with emphasis on Sr and Mg substituted $LaGaO_3$." *Journal of Alloys and Compounds* **329**(1), 253–258 (2001).

[105] M. S. Islam. "Ionic transport in $ABO_3$ perovskite oxides: a computer modelling tour." *Journal of Materials Chemistry* **10**(4), 1027–1038 (2000).

[106] T. Ishihara, J. A. Kilner, M. Honda, and Y. Takita. "Oxygen surface exchange and diffusion in the new perovskite oxide ion conductor $LaGaO_3$." *Journal of the American Chemical Society* **119**(11), 2747–2748 (1997).

[107] P. Hohenberg and W. Kohn. "Inhomogeneous electron gas." *Physical Review* **136**(3B), B864 (1964).

[108] W. Kohn and L. J. Sham. "Self-consistent equations including exchange and correlation effects." *Physical Review* **140**(4A), A1133 (1965).

[109] J. P. Perdew. "Density-functional approximation for the correlation energy of the inhomogeneous electron gas." *Physical Review B* **33**(12), 8822 (1986).

[110] J. P. Perdew, K. Burke, and M. Ernzerhof. "Generalized gradient approximation made simple." *Physical Review Letters* **77**(18), 3865 (1996).

[111] J. P. Perdew, K. Burke, and Y. Wang. "Generalized gradient approximation for the exchange-correlation hole of a many-electron system." *Physical Review B* **54**(23), 16533 (1996).

[112] G. Kresse and J. Furthmüller. "Efficient iterative schemes for ab initio total-energy calculations using a plane-wave basis set." *Physical Review B* **54**(16), 11169 (1996).

[113] G. Kresse and D. Joubert. "From ultrasoft pseudopotentials to the projector augmented-wave method." *Physical Review B* **59**(3), 1758 (1999).

[114] G. Makov and M. Payne. "Periodic boundary conditions in ab initio calculations." *Physical Review B* **51**(7), 4014 (1995).

[115] J. Neugebauer and M. Scheffler. "Adsorbate-substrate and adsorbate-adsorbate interactions of Na and K adlayers on Al(111)." *Physical Review B* **46**(24), 16067 (1992).

[116] H. J. Monkhorst and J. D. Pack. "Special points for Brillouin-zone integrations." *Physical Review B* **13**(12), 5188 (1976).

[117] M. Methfessel and A. Paxton. "High-precision sampling for Brillouin-zone integration in metals." *Physical Review B* **40**(6), 3616 (1989).

[118] P. E. Blöchl. "Projector augmented-wave method." *Physical Review B* **50**(24), 17953 (1994).

[119] G. Henkelman, B. P. Uberuaga, and H. Jónsson. "A climbing image nudged elastic band method for finding saddle points and minimum energy paths." *The Journal of Chemical Physics* **113**(22), 9901–9904 (2000).

# Acknowledgement

I acknowledge Ministry of Education, Culture, Sports, Science, and Technology (MEXT) for 5-year scholarship.

I would like to express my sincere gratitude to Prof. H. Kasai for all of guidance, assistance and advises throughout my stay in Japan. I would like to give my thanks to Prof. W. A. Diño and Prof. M. Sakaue for all of the discussions, constructive comments and suggestions, not only for my current research but also for my future works. To Prof. H. Akai and Prof. M. Ogura for the warm support and guidance from the first day I came to Japan. To the vice-examiners of my graduation, Prof. Y. Morikawa and Prof. K. Yamauchi for your valuation time and suggestions towards to the improvements of this dissertatation. I thank sincerely Prof. Nakanishi and the staff of Kasai Laboratory for all their assistance and support, especially in my daily life. To all students in Kasai Laboratory, especially M. Alaydrus, S. M. Aspera, K. Shimizy and former members, T. P. T. Linh and K, Oka, for all your patient discussion, helpful suggestions and patient support in my works and daily life.

I am so much grateful to all my Vietnamese seniors and friends for their academic discussions and mental support throughout my 5 years in Japan. Lastly, I would like to dedicated this work to my family, who are always by my side. I could not be here and finished my work without their encouragement.

This work is my most sincere gratefulness to all the help and support that I receive up to now.

# List of Publications

1. Tran Phan Thuy Linh, Mamoru Sakaue, Susan Meñez Aspera, Musa Alaydrus, Triati Dewi Kencana Wungu, Nguyen Hoang Linh, Hideaki Kasai, Takahiro Mohri, Tatsumi Ishihara. "First-principles calculation on oxygen ion migration in alkaline-earth doped $La_2GeO_5$", *Journal of Physics: Condensed Matter* **26** (2014), 255503.

2. Musa Alaydrus, Mamoru Sakaue, Susan Meñez Aspera, Triati Dewi Kencana Wungu, Nguyen Hoang Linh, Tran Linh PhanThuy, Hideaki Kasai, Tatsumi Ishihara, and Takahiro Mohri . "A DFT+U Study of Strain-Dependent Ionic Migration in Sm-Doped Ceria ", *Journal of the Physical Society of Japan* **83** (2014), 094707.

3. Tran Phan Thuy Linh, Mamoru Sakaue, Susan Meñez Aspera, Musa Alaydrus, Triati Dewi Kencana Wungu, Nguyen Hoang Linh, Hideaki Kasai, Takahiro Mohri, Tatsumi Ishihara. "First-principles calculation on oxygen ion migration in alkaline-earth doped $La_2GeO_5$", *Journal of Physics: Condensed Matter* **26** (2014), 255503

4. Nguyen Hoang Linh, Tien Quang Nguyen, Wilson Agerico Diño, Hideaki Kasai."Effect of Oxygen Vacancy on the Adsorption of $O_2$ on Anatase $TiO_2$(001): A DFT-Based Study" *Surface Science* **633** (2015), 38.

5. Nguyen Hoang Linh, Hideaki Kasai. "Effect of Oxygen Vacancy on the Structure and Electronic Properties of $LaGaO_3$: A DFT-Based Study", submitted to *Journal of Physics: Condensed Matter* (2015).

6. Nguyen Hoang Linh, Hideaki Kasai. "Role of O-vacancy on the geometric and electronic structure of $LaGaO_3$-based materials: Sr- and Mg- doped", submitted to *Journal of Applied Physics* (2015).

**Proceedings:**

Musa Alaydrus, Mamoru Sakaue, Nguyen Hoang Linh, Susan Meñez Aspera, Hideaki Kasai, "Praseodymium doped ceria: The role of 4f-electrons of Pr dopant in doped ceria, ECS Transactions" (accepted, to be published on July 26, 2015)

# List of Scientific Meeting

1. "Electronic Structure and Magnetic Properties of Iron-Pnictide", Nguyen Hoang Linh, Masako Ogura, Hisazumi Akai, *The Physical Society of Japan - Fall meeting 2012*, Yokohama National University, Yokohama, Japan.

2. "Effect of Vacancy on $O_2$ adsorption on $TiO_2$ anatase (001) surfaces". Nguyen Hoang Linh, Ganes Shukri, Hideaki Kasai, *The 60th Japan Society of Applied Physics-Spring Meeting*, March 27-30, 2013, Kanagawa Institute of Technology, Atsugi, Japan.

3. "First-principles study of the oxygen molecular adsorption on $TiO_2$ anatase (001) surfaces". Nguyen Hoang Linh, Mamoru Sakaue, Hideaki Kasai, *International Symposium on Frontiers in Materials Science*, November 17-19, 2013, Hanoi University of Science, Hanoi, Vietnam.

4. "Effect of Oxygen Vacancy on Oxygen Molecular Adsorption on Anatase $TiO_2$(001) Surface: A DFT study". Nguyen Hoang Linh, Wilson Agerico Diño, Hideaki Kasai, *HeKKSaGOn Summer School 2014*, September 1-10, 2014, Karlsruhe Institute of Technology, Karlsruhe,Germany.

5. "DFT study of $LaGaO_3$-based materials for oxygen migration". Nguyen Hoang Linh, Mamoru Sakaue, Hideaki Kasai, *The 55th Annual Syposium of the Vacuum Society of Japan*, November 18-20, 2014, Osaka Prefecture University I-site Namba, Osaka, Japan.

6. "DFT study of $LaGaO_3$-based materials for oxygen migration". Susan Meñez Aspera, Mamoru Sakaue, Musa Alaydrus, Tran Linh Phan Thuy, Nguyen Hoang Linh, Hideaki Kasai, *The 55th Annual Syposium of the Vacuum Society of Japan*, November 18-20, 2014, Osaka Prefecture University I-site Namba, Osaka, Japan.

7. "Praseodymium Doped Ceria: The Role of 4f-Electrons of Pr Dopant in Doped Ceria".Musa Alaydrus, Mamoru Sakaue, Nguyen Hoang Linh, Susan Meñez Aspera, Triati K D Wungu, Hideaki Kasai, *ECS Conference on Electrochemical Energy Conversion & Storage with SOFC-XIV*, July 26-31, 2015, Glasgow, Scotland.